BJR

Contrast-enhanced MRI

Research papers from *BJR*

Guerbet

Contents

BJR

BJR is the international research journal of the British Institute of Radiology and is the oldest scientific journal in the field of radiology and related sciences.

An international, multi-disciplinary journal, *BJR* covers the clinical and technical aspects of medical imaging, radiotherapy, oncology, medical physics, radiobiology and the underpinning sciences. *BJR* is essential reading for radiologists, medical physicists, radiation oncologists, radiotherapists, radiographers and radiobiologists.

REVIEW ARTICLE

Brain metastases: the role of clinical imaging

[1,2,3]SOPHIE H. A. E. DERKS, MD, [2,3]ASTRID A. M. VAN DER VELDT, MD, PhD and [2]MARION SMITS, MD, PhD

[1]Department of Neuro-Oncology, Erasmus MC Cancer Institute, Rotterdam, The Netherlands
[2]Department of Radiology & Nuclear Medicine, Erasmus Medical Center, Rotterdam, The Netherlands
[3]Department of Medical Oncology, Erasmus MC Cancer Institute, Rotterdam, The Netherlands

Address correspondence to: Professor Marion Smits
E-mail: marion.smits@erasmusmc.nl

ABSTRACT

Imaging of brain metastases (BMs) has advanced greatly over the past decade. In this review, we discuss the main challenges that BMs pose in clinical practice and describe the role of imaging.

Firstly, we describe the increased incidence of BMs of different primary tumours and the rationale for screening. A challenge lies in selecting the right patients for screening: not all cancer patients develop BMs in their disease course. Secondly, we discuss the imaging techniques to detect BMs. A three-dimensional (3D) T1W MRI sequence is the golden standard for BM detection, but additional anatomical (susceptibility weighted imaging, diffusion weighted imaging), functional (perfusion MRI) and metabolic (MR spectroscopy, positron emission tomography) information can help to differentiate BMs from other intracranial aetiologies.

Thirdly, we describe the role of imaging before, during and after treatment of BMs. For surgical resection, imaging is used to select surgical patients, but also to assist intraoperatively (neuronavigation, fluorescence-guided surgery, ultrasound). For treatment planning of stereotactic radiosurgery, MRI is combined with CT. For surveillance after both local and systemic therapies, conventional MRI is used. However, advanced imaging is increasingly performed to distinguish true tumour progression from pseudoprogression.

FInally, future perspectives are discussed, including radiomics, new biomarkers, new endogenous contrast agents and theranostics.

INTRODUCTION

The field of clinical oncology is rapidly changing. With improving treatments, advanced cancer is better controlled, leading to improved overall survival (OS) and even curation.[1] However, brain metastases (BMs) now more often emerge in cancer patients, and they seem to behave differently from extracranial disease. Brain metastases are still associated with poor OS, with an estimated OS rate for all tumour types of 8.1% at 2 and 2.5% at 5 years after diagnosis.[2]

In BMs, the efficacy of most systemic anticancer therapies is reduced, at least in part due to features of the blood-brain barrier and the unique brain microenvironment.[3] Fortunately, targeted therapies (TTs) and immune checkpoint inhibitors (ICIs) have shown a beneficial effect on intracranial disease response and survival in patients with BMs of certain cancer types, for example in subgroups of melanoma and non-small cell lung cancer.[4,5] Local therapies, such as surgical resection and stereotactic radiosurgery (SRS), have also improved over the past years and are now increasingly applied. Currently, SRS is even found effective in patients with over 10 brain lesions.[6,7]

The increased use of these systemic and local treatments results in an increased incidence of treatment-related effects. Pseudoprogression (PsPD) is a commonly used term to describe such effects, but its definition is highly variable in the literature.[8] In general, PsPD is defined as an increase of radiological abnormalities, months after therapy, which is not actual tumour progression.[8] Pseudoprogression can be found after treatment with SRS or systemic treatment such as ICIs.[9] Radiation necrosis (RN), which can appear as pseudoprogression on imaging, is a treatment-related effect confirmed by histopathology, found months to years after treatment with SRS. It can lead to invalidating neurological symptoms or even death.[8,10]

As a result of these new developments, these days, treating physicians face a number of questions. With the rising incidence of BMs, what is the right time to screen for BMs in patients with cancer and is screening even effective (Figure 1a)? When BMs have emerged, how extensive are they, and how can BMs be differentiated from other intracranial lesions (Figure 1b)? Finally, how can treatment best be planned (Figure 1c) and monitored (Figure 1d)?

Figure 1. The role of clinical imaging in brain metastasis management. A, B, C and D represent separate sections in this review.
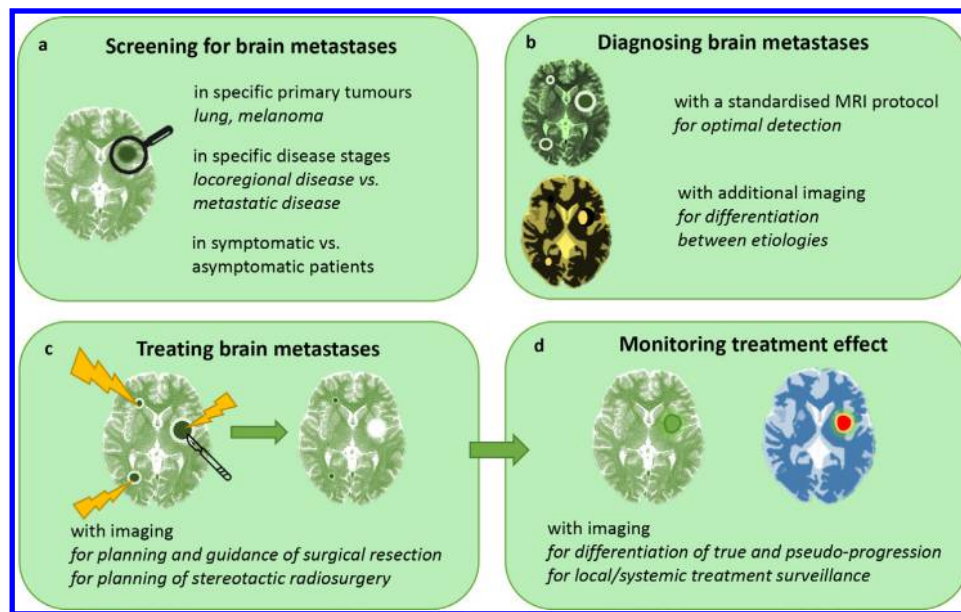
In answering these questions, imaging plays an increasingly important role; in fact, it already is the cornerstone in clinical decision making for oncology today. In this review, we describe the application of several imaging techniques in the clinical practice of BM management, and the promising new developments that lie ahead.

SCREENING FOR BRAIN METASTASES
Incidence and timing
The incidence of BMs has increased over the past decade. The aging population leads to a yearly increase in cancer diagnoses, which in turn increases the probability of BMs.[11,12] Further adding to that probability are the improved systemic disease control that modern treatments provide, along with more frequent use of sensitive imaging techniques.[3,13] The lifetime incidence to develop BMs for a patient with cancer lies approximately between 10 and 30%, but might be even higher due to selection bias in reported studies.[3,13,14]

Not only the incidence of BMs has increased over time but also the interval between primary tumour diagnosis and BM development.[12] This shift in disease course might be another result of improved systemic treatments.

Substantial geographical variations in the application of diagnostics, access to health care and health care/economic policies make it difficult to know the exact incidence of BMs. Asymptomatic BMs are only detected by screening or by autopsy after death. The presence of extracranial metastatic disease, especially metastases in liver and lungs, increases the likelihood of BMs in patients with any cancer type.[3] Furthermore, certain primary tumours and molecular characteristics are associated with a higher risk of BMs.[3] Lung cancer, breast cancer and melanoma are most often associated with BMs, but gastro-intestinal cancer, renal cell cancer and gynaecologic cancers are also increasingly

found to metastasise to the brain.[3,13,15] Table 1 provides more in-depth information on BMs per tumour type.

To screen or not to screen
Imaging of the brain in oncological patients with neurological deficits or symptoms of increased intracranial pressure (*e.g.,* headache, vomiting) is routinely performed to assess the presence of BMs. However, there is no consensus on screening for asymptomatic BMs, not even for cancer types with high risk of BMs. For example, the European Society for Medical Oncology (ESMO) recommends screening for BMs in all patients with NSCLC, whereas the National Comprehensive Cancer Network (NCCN) does not recommend screening in stage I NSCLC patients without symptoms suggestive of BMs.[20] A survey among treating physicians across the world showed that 85% of the respondents performed screening of BMs at primary presentation of advanced lung cancer in patients without symptoms.[34] In SCLC, screening for BMs is always recommended at primary diagnosis.[35] For patients with melanoma, the NCCN recommends screening in patients with stage IIIC to IV, whereas in breast cancer, screening is only recommended for symptomatic patients.[36]

Arguments against screening are that BMs can develop much later in the disease course and could therefore be missed by screening "too early". In addition, it is not known how fast asymptomatic BMs become symptomatic, which could be within a short time interval; in that case, symptomatology would soon have been followed by imaging anyway. Moreover, it is not yet known whether early detection of asymptomatic BMs truly impacts treatment decisions and improves survival.[28,37]

Arguments in favour of screening are that, with knowledge of asymptomatic BMs, treating physicians can make better informed decisions about systemic treatments. Potentially,

Table 1. Primary tumours associated with brain metastases (BMs)

Lung cancer
• Second highest incidence in the general population[15]
• Two-thirds of patients with BMs as a first diagnosis have lung cancer.[15–17]
• Non-small cell lung cancer (NSCLC) constitutes 85% of all lung cancer types; small cell lung cancer (SCLC) has the highest risk of BMs[15]
• Reported lifetime risk of BM development[16]:
• 19.9% in all disease stages
• 9.2% in local disease
• 14.6% in regional disease
• 29.9% in metastatic disease
• Risk factors for BMs: younger age, female gender, adenocarcinoma subtype, and more advanced disease (both locoregional and metastatic).[17–19]
• Driver mutations for targeted therapy: endothelial growth factor receptor (EGFR) mutations in 30–70% and anaplastic lymphoma kinase (ALK) mutations in 60–90% of BMs from NSCLC[3,20,21]

Breast cancer
• Highest incidence in the general population[22]
• BMs can develop late in the disease course[23]
• Reported lifetime risk of BMs[16]:
• 5.1% in all disease stages
• 2.5% in local disease
• 6.8% in regional disease
• 14.2% in metastatic disease
• Risk factors for BMs: age above 41 years, triple-negative and human epidermal growth factor receptor 2 (HER2)-positive subtypes, and metastatic disease in 2–3 extracranial sites[3,23]
• Driver mutations for targeted therapy: HER2-positive BMs[24]

Melanoma
• Highest risk to metastasise to the brain of all solid tumours[15]
• Approximately half of melanoma patients have BMs in their disease course[15]
• BMs can occur very late in the disease course, even more than 10 years after initial diagnosis[8,25]
• Reported lifetime risk of BMs:[16]
• 6.9% in all disease stages
• 4.1% in local disease
• 18.5% in regional disease
• 36.8% in metastatic disease
• Risk factors for BMs: older age (peak incidence between 50–59 years), male gender, specific characteristics of the primary melanoma (higher T-stage, location at head/neck or trunk, presence of ulceration, nodular subtype, desmoplastic or spindle cell melanoma, increasing depth of invasion)[3,26,27]
• Driver mutations for targeted therapy: V-raf murine sarcoma viral oncogene homolog B1 (BRAF) mutations are found in approximately half of melanoma patients with BMs (not specifically associated with a higher risk for BMs)[26–28]

Renal cell cancer (RCC)
• Low incidence in the general population, metastasises to the brain relatively often[29]
• Reported lifetime risk of BMs[6,16]:
• 6.5% in all disease stages
• 2.5% in local disease
• 7.6% in regional disease
• 13.4% in metastatic disease
• Clear cell RCC most common subtype associated with BMs[3,29]
• Driver mutations for targeted therapy: vascular endothelial growth factor receptor (VEGFR)[29]

(Continued)

Table 1. (Continued)

Colorectal cancer (CRC)
• Most frequent type of gastro-intestinal cancer; in the top 5 of general population cancer incidence[6,22,30]
• Reported lifetime risk of BMs[16,24]:
• 1.8% in all disease stages
• 0.8% in local disease
• 2.0% in regional disease
• 2.9% in metastatic disease
• CRC rarely metastasises to the brain, usually late in the disease course[30]
• Driver mutations for targeted therapy: RAS mutations[31]

Gynaecological cancers
• Incidence of BMs is low (<1%)[32]
• Most common types associated with BMs are ovarian, endometrial and cervical cancer[32]
• Data on BMs of gynaecologic cancers is limited[33]

there are also more local treatment options: asymptomatic BMs tend to be smaller and therefore better to treat by surgery or radiation. In general, screening for BMs is considered in more advanced disease stages. In case of extracranial metastatic disease, screening for BMs should be considered if BMs would change the treatment plan. In cancers that rarely metastasise to the brain, such as renal cell, colorectal and gynaecologic cancers, screening is generally only performed in patients with symptoms and/or neurologic deficits.

DIAGNOSING BRAIN METASTASES

Since screening for BMs is not standard of care, most patients with BMs will present with symptoms such as headache, nausea or vomiting, epilepsy or neurologic deficits. In the acute setting, computed tomography (CT) is usually performed for rapid intracerebral evaluation and detection of potential neurosurgical emergencies.[38] CT is also a useful tool to detect haemorrhage, calcification, and evaluate osseous structures.[39] The golden standard for detecting BMs, however, is magnetic resonance imaging (MRI).[3,14] This imaging technique has excellent soft-tissue contrast with high-resolution depiction of tissue anatomy.[40]

Conventional MRI

In order to achieve a more reliable inter-image, and inter-centre, assessment of BMs at diagnosis and in treatment evaluation, Kaufmann et al have proposed a standardised MRI protocol.[14] Their recommendation is based on that of the working group of Response Assessment in Neuro-Oncology-Brain Metastases (RANO-BM) and the Brain Tumour Imaging Protocol for glioma research (BTIP).[14] According to this standard protocol, a pre- and post-contrast 3D T1W sequence is always required.[14] Furthermore, high-resolution T2W imaging should be performed, optionally with fluid attenuation inversion recovery (FLAIR) to optimally detect vasogenic oedema.[14]

In order to detect all BMs, in particular small lesions (<5 mm), MRI needs to be highly sensitive. Higher field strength increases this sensitivity; scanning at 3 Tesla (T) is much more sensitive than scanning at 1.5T.[41] The optimal choice of post-contrast T1W pulse sequence is still under debate. A magnetisation prepared

Figure 2. Axial, three-dimensional (3D) contrast-enhanced T1W image (ce-T1W) on the left, with the corresponding 3D contrast-enhanced T2W Fluid Attenuated Inversion Recovery image (ce-T2W FLAIR) on the right, from a patient with leptomeningeal disease (LMD, arrow). The ce-T2W FLAIR image shows the region of LMD much clearer than the ce-T1W image
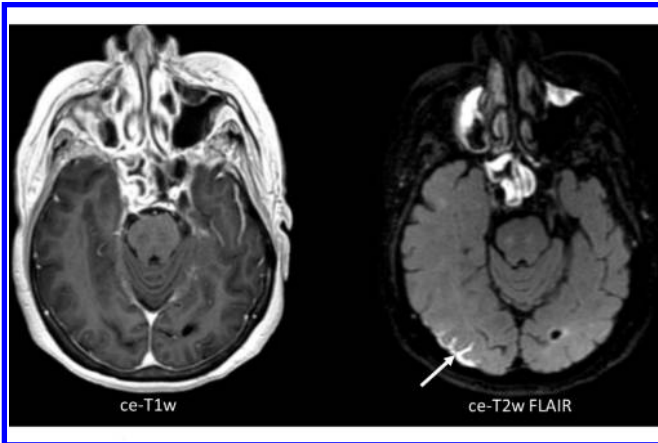
("IR-prepped") gradient recalled echo (GRE) pulse sequence is robust, has high signal-to-noise, and is widely available.[14] Kaufmann et al recommend this sequence to be in the minimal standardised MRI protocol for BMs.[14] However, IR-GRE sequences have slightly less conspicuous contrast enhancement than spin echo (SE) or turbo SE (TSE)-based pulse sequences, in particular at lower field strengths (<3T).[14] 3D (T)SE sequences are however less widely available and have only been sufficiently evaluated at 3T, while 2D sequences render the technique less sensitive to small lesions due to lower through-plane resolution. While the "ideal" protocol thus replaces IR-GRE with 3D TSE T1W imaging pre- and post-contrast administration, and is best performed at 3T, this is not universally attainable. Some sites therefore add a (T)SE sequence to the protocol, but this clearly comes at the cost of additional scanning time.[14] Double or triple doses of a gadolinium-based contrast agent (GBCA) are superior to a single dose, but can lead to an increased number of false-positive findings.[3,38] For the detection of dural or leptomeningeal disease, contrast-enhanced 3D MRI is the most sensitive technique, especially combined with FLAIR (Figure 2).[38] Time-delayed imaging, for example, waiting 15 to 20 min before scanning post-contrast, may further increase sensitivity, especially in the posterior circulation.[38] However, this is time-consuming and therefore not always possible in clinical practice.[38]

Brain metastases are usually iso- to hypointense to grey matter on T1W images, and are of variable intensity on T2W images.[38] Vasogenic oedema typically involves the white matter, creating a "finger-shaped" lineage below the cortex.[38] This oedema can be strikingly disproportionate to the size of the BM, but it can also be completely absent.[3] Other common features of BMs are a spherical, delineated shape and ring enhancement of larger BMs after contrast administration, due to central necrosis.[38,42] Calcification in BMs can be of high intensity on T1W and low on T2W imaging, but varies with its composition.[38] Haemorrhage in BMs can show varying signal intensities on T1W and T2W imaging, depending on different stages over time.[38] Because BMs spread

haematogenically, they usually occur on the grey-white matter junction or watershed zones, where the luminal diameters of arterioles decrease.[3,14] Most BMs are found supratentorially (80%), but BMs can also emerge below the tentorium.[14] More features per primary tumour type are displayed in Table 2; however, none of these features are completely specific for BMs or for BMs of different primaries. The differential diagnosis includes infection (abscess in particular), inflammation, auto-immune disease and primary brain tumour.[3]

Additional imaging

In addition to the standard MRI protocol, advanced MRI sequences and other imaging techniques may provide information on specific lesion characteristics. Although they are promising for clinical imaging, most of these techniques are still evaluated in experimental settings and lack standardisation across centres.
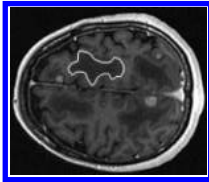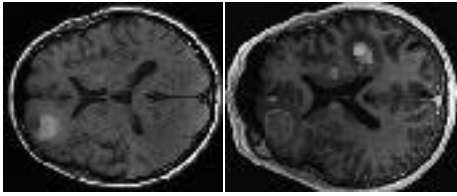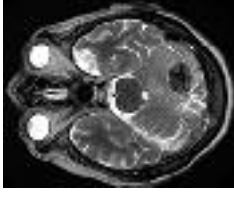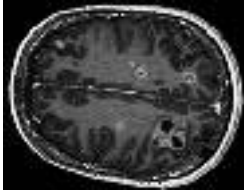
Susceptibility weighted imaging (SWI) might be of added value in confirming the diagnosis of melanoma BMs.[45] Melanin and blood products can be found in these lesions and are paramagnetic, showing susceptibility artefacts on SWI.[45] Since approximately 66% of melanoma BMs have such susceptibility-related signal loss, SWI might be used to differentiate BMs of melanoma from other cancer types.[45] In general, however, SWI is not sufficiently sensitive for detecting BMs.[38] A small study investigated the use of quantitative susceptibility mapping (QSM) to detect melanin content in melanoma BMs, but could not demonstrate an isolated signal for melanin.[47]

DWI can show signal decreases (restriction) in BMs due to increased cellularity.[38] This sequence is most commonly used to differentiate BMs from other intracranial lesions as abscess. Both BMs and abscesses can present as a ring-enhancing lesion on post-contrast T1W imaging.[3,40] In abscesses, diffusion is usually far more restricted than in BMs, particularly in the central non-enhancing portion. However, brain abscesses can rarely (4%) also present without diffusion restriction.[3,38]

Since increased tissue perfusion is a hallmark of cancer, perfusion MRI can be used to discriminate BMs from normal brain tissue. Dynamic susceptibility contrast (DSC) perfusion MRI is most commonly used and measures relative cerebral blood volume (rCBV). Arterial spin labelling (ASL), measuring cerebral blood flow (CBF), is less commonly used. It has a relatively lower signal-to-noise ratio and spatial resolution, but also has advantages over DSC: there is no need for exogenous contrast administration, it is not sensitive to susceptibility artefacts or signal drop (with an SE read-out) and it does suffer from leakage effects.[48] Perfusion MRI could help to distinguish BMs from primary brain tumours: the peritumoural region of glioblastoma is mostly associated with higher rCBV values than that of BMs.[49] Unfortunately, however, lack of standardisation within and between centres still results in undefined cut-off points for rCBV and CBF for diagnosing different aetiologies.[38]

Metabolic information can be obtained with magnetic resonance spectroscopy (MRS). Using the standardised (Cho)/Creatine

Table 2. Imaging features of BMs, characteristic (but not specific) for different primary tumours

Primary tumour type	Lung cancer	Breast cancer	Melanoma	Renal cell cancer	Colorectal cancer	Gynaecological cancers
Common imaging features	• Common presentation with multiple BMs[15,38] • Associated with leptomeningeal disease, especially in adenocarcinoma[3,43]	• A single or multiple BMs[38] • Associated with leptomeningeal disease[3] • Triple negative breast cancer can show substantially more necrotic and cystic BMs, with very bright T2W signal and low T1W signal centrally.[3,38]	• Common presentation with multiple BMs[15,27,38,44] • Associated with leptomeningeal disease[3] • Haemorrhagic lesions are common[45] • Commonly hyperintense on native T1W imaging due to haemorrhage and/or melanin[3,45]	• A single BM is diagnosed in > 50% of cases[29,38] • Associated with spontaneous haemorrhage[29]	• A single or multiple BMs[38] • Can present as mucinous or protein-rich lesions, with low T2W signal intensity[38]	• A single or multiple BMs[46]
MRI example	 Axial contrast-enhanced T1W: multiple BMs and vasogenic oedema (one zone is highlighted by the white delineation).	 Top: axial contrast-enhanced T1W. Bottom: axial T2W, at approx. the same slice position: BM with cystic components, with centrally low T1W and high T2w signal intensities and rim enhancement.	 Top: axial pre-contrast T1W: revealing BMs through increased signal intensity (melanin). Bottom: axial contrast-enhanced T1W: revealing even more contrast-enhancing BMs in the same patient.	 Axial pre-contrast T1W: a single BM with signal hyperintensity, suggestive of blood products.	 Axial pre-contrast T2W: BM in the left cerebellar hemisphere with low (central) signal intensity.[38]	 Axial contrast-enhanced T1W: multiple BMs from ovarian carcinoma.

(Cr)-ratio, MRS might help to distinguish non-small cell lung cancer (NSCLC) from melanoma and breast cancer BMs.[50] In a study by Huang et al, a ratio < 2.0 was never found in melanoma BMs, in 38% of patients with lung cancer BMs and in 24% of patients with breast cancer BMs.[50] A high lipid content measured with MRS is associated with BMs from colorectal cancer.[38] In clinical practice, MRS is not widely used due to challenges in acquisition, time constraints and limited availability of analysis tools on commercial MR scanners.[51]

Combining positron emission tomography (PET) with CT or MRI combines metabolic with anatomic information. Numerous tracers have been tested in small, selected patient groups. [^{18}F]–2-fluoro-2-deoxy-D-glucose (^{18}F-FDG) is most widely used in general oncological practice and has high uptake in tumour cells, but the diagnostic accuracy for detecting BMs is limited since the brain itself also has high uptake of ^{18}F-FDG.[9] [^{52}Ga]Ga-dodecane tetra-acetic acid-fibroblast activation protein inhibitor (DOTA-FAPI)–04 is a relatively new tracer, which was found to have a higher efficacy than ^{18}F-FDG in PET/CT imaging in detecting brain tumours.[53] Radiolabelled amino acids are also more suitable for imaging pathology in the brain than ^{18}F-FDG, since these tracers have low uptake in normal brain tissue.[9] [^{11}C]-methyl-L-methionine (MET), 3,4-dihydroxy-6-[^{18}F]-fluoro-L-phenylalanine (^{18}F-FDOPA) and O-(2-[^{18}F]-fluoroethyl)-L-tyrosine (^{18}F-FET) are recommended for detecting BMs, with high uptake values indicating overexpression of L-type amino acid transporter (LAT), a feature of BMs.[9]

The specific combination of PET with MRI is being implemented in clinical use but still has some relevant technical challenges to overcome. The synergy of combined MRI and PET could help to improve the diagnostic value of both modalities.[54]

TREATING BRAIN METASTASES
Local therapies
Surgical resection is usually performed in patients with relatively good performance status, stable or absent systemic disease, and one of two intracranial scenarios: either up to three BMs, or a single BM amongst several smaller, presumably asymptomatic lesions.[55,56] Resected BMs are usually symptomatic or expected to become symptomatic soon. In rare cases, the brain is the only site of metastatic disease, in which case resection could even have curative intention. Surgical resection is sometimes primarily performed for diagnosis rather than treatment; for example, when the primary tumour is unknown or when there is a differential diagnosis (such as glioma or abscess).

The goal of resection is always to remove a BM in its entirety. To achieve complete resection, intraoperative imaging and surgical techniques are constantly being improved, requiring accurate cross-sectional imaging for neuronavigation.[55] Fluorescence-guided surgery with 5-aminolevulinic acid (5-ALA), best known for glioma resection, is less frequently used in BM resections, mostly in non-academic centers.[57] Intraoperative ultrasound (US) is frequently used in surgery, providing a real-time and inexpensive method that distinguishes the dense tissue of BMs from normal brain tissue.[55,57] The use of intra-operative MRI

systems is still limited due to lacking cost-effectiveness; CT is not useful due to shortcomings in depicting soft tissue contrast.[55,57]

Laser interstitial thermal therapy (LITT) uses laser ablation and is increasingly explored for local BM treatment.[58] This technique uses pre- and intra-treatment MRI guidance to plan the laser probe tract and to adjust treatment during the procedure.[58] During ablation, changes in MRI signal, in particular T1W hyperintensity, provide information on the laser-induced tissue damage.[58]

Early postoperative imaging, preferably with MRI, to determine the completeness of surgical resection, should be performed within 48 up to 72 h after surgery to avoid surgery-related enhancement.[57] In case of residual tumour in the resection cavity, adjuvant SRS is increasingly routinely performed.[56,59]

Whole brain radiotherapy (WBRT) was historically the treatment of choice for patients with multiple BMs.[7] Stereotactic radiosurgery (SRS) is gradually taking over this position, with recent advances that have increased effectivity and reduced toxicity, even in patients with multiple BMs.[7] For planning of SRS, MRI including at least a post-contrast 3D T1W sequence is required to accurately visualise the BMs. This scan must be obtained preferably within one and ultimately within 2 weeks before the start of SRS.[7,60] In addition, a CT scan, preferably post-contrast and with 1-mm slice thickness, is fused with the MR images.[7] This CT scan is required for positioning and to correct for geographic distortions in the MR image.[7] Repeated MRI scans during more prolonged fractionated SRS schemes should be considered, as target volume can change during the course of therapy.[60]

Over half of patients treated with SRS develop BMs at other brain sites during follow-up. For this reason, regular MRI follow-up is recommended in patients who have remaining treatment options.[7] Follow-up MRI should be planned at intervals of 2 to 3 months; more frequent scanning does not affect clinical outcomes in the absence of neurological symptoms.[7,61]

Systemic therapies
Systemic therapy is considered in all patients with metastatic disease. Systemic therapy is used in patients with asymptomatic BMs or BMs controlled by local treatment to treat active extracranial disease. However, systemic therapy can also be used to treat patients with rapid progression of BMs, when a fast response from systemic therapy can be expected. An example of the latter is the use of BRAF/MEK inhibition in melanoma patients with BMs.[62]

Intracranial response evaluation is required after initiation of systemic therapy. For example, in NSCLC, response evaluation of anti-PD-1 therapy is recommended after 2 to 3 months of therapy.[43] For sequential response evaluation, the MRI protocol should include the same sequences and sequence settings as at baseline and is preferably performed on the same scanner. For BMs, the RANO group has proposed recommendations for evaluation (RANO-BM criteria) and follow-up after ICI treatment (iRANO criteria).[63,64] According to the RANO-BM criteria,

diameters of up to 5 BMs are unidimensionally measured and summed. Progression is defined as this sum exceeding 20% increase compared to that on baseline MRI or the MRI showing the best response. Response to treatment is defined as a reduction of the sum by more than 30% compared with baseline.[64] For immunotherapy, in case of significant clinical deterioration (not caused by comorbidity/medication toxicity) within 6 months of the last treatment, a repeated MRI of the brain must be obtained 3 months following the initial MRI suspect for progression, to determine true progression.[63] If clinical deterioration occurs more than 6 months after the last immunotherapy treatment, the standard RANO-BM criteria apply.[64]

Treatment-related effects

During follow-up, the increase of radiologic abnormalities or enhancement in the tumour region can represent BM progression or PsPD.[9,40] However, conventional MRI is not capable of distinguishing PsPD from true progression.[8] In addition, an increase in lesion volume may consist of a mixture of tumour progression and RN, making the interpretation of imaging findings even more complex.[65] Initial increase of imaging abnormalities such as enhancement, followed by a decrease on follow-up imaging over a clinically relevant period of time (*e.g.,* 3–6 months), should be regarded as PsPD, whereas further increase indicates true progression.[8,66]

Both TTs and especially ICIs are associated with PsPD, alone or in combination with SRS.[9] In the first weeks, up to 6 months following treatment, an inflammatory reaction can appear on MRI as an increase of contrast enhancement in both existing lesions and in newly detected lesions.[9] Pseudoprogression has been reported in up to 5–10% of patients treated with ICIs.[9]

Radiation necrosis can emerge months to years after SRS. Due to variations in applied definition of RN and uncertainty of the diagnosis, the reported incidence rates vary.[8] In a large,

retrospective study, Kohutek et al have reported RN to develop in ≥25% of BMs treated with SRS.[67]

Of all advanced imaging techniques, perfusion MRI is most commonly applied in clinical practice to discriminate BM progression from PsPD/RN. Relative CBV, as obtained with DSC perfusion MRI, is commonly higher in tumour than in RN due to higher vascularity of BMs.[68] However, optimal cut-off levels for rCBV are difficult to determine, and reported rCBV cut-off points vary across studies, while the literature on BMs – compared to that of primary brain tumours – is scarce.[68–70] Knitter et al evaluated interval changes in several imaging parameters and found this potentially more reliable in predicting the final diagnosis.[71] Taunk et al found the volume transfer constant (K^{trans}) as obtained with DCE perfusion MRI to also be a potentially valid biomarker for predicting response following SRS.[72] Similar findings are reported for ASL (Figure 3)[48]; however, as the signals derived from these different perfusion modalities are obtained using different techniques, sometimes they might show contradicting (or complementary) results. (Figure 4).

On DWI, ADC is usually low in tumour tissue and high in RN, although this distinction is not universal.[73] Using MRS, Cho/Cr-ratio and Cho/N-acetyl-aspartate (NAA)-ratio were found to be higher in tumour than in RN.[74] In MET-PET, uptake is usually higher in progressive BMs than in RN; FDOPA- and FET-PET have also shown a potential discriminating ability in smaller studies.[10,75,76] Larger, multi-centre, randomized cohort studies are required for all these techniques, to determine their true clinical value.

FUTURE PERSPECTIVES

Although research on BM diagnostics is increasing, the explorative nature of these studies limit clinical implementation.[77] Nevertheless, some of these techniques show promise and pave the way for future translational studies.

Figure 3. Axial contrast-enhanced T1W (ce-T1W) and native T1W images and a cerebral blood flow (CBF) map derived from arterial spin labelling (ASL), from a patient with a brain metastasis in the left parietal lobe, treated with stereotactic radiosurgery (SRS). The lesion increased in size 1 month after SRS and was histopathologically confirmed to be a combination of subacute haemorrhage and tumour progression. Most of the lesion is hyperintense before contrast administration, due to subacute haemorrhage. This portion has no perfusion on ASL. One small component is enhancing and shows increased perfusion on ASL (arrow), consistent with tumour progression.
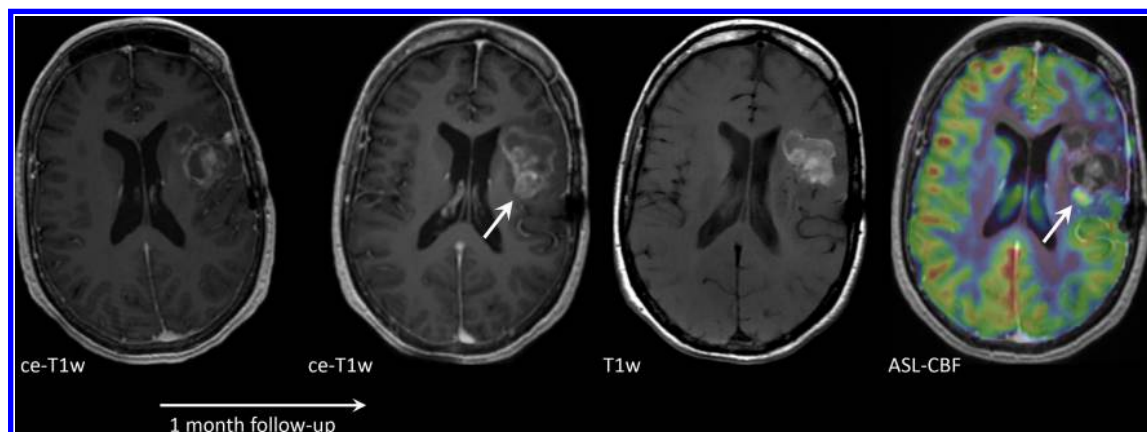
Figure 4. Axial contrast-enhanced T1W (ce-T1W) image, relative cerebral blood volume (rCBV) and cerebral blood flow (CBF) maps derived from dynamic susceptibility contrast enhanced (DSC) performed after a pre-load bolus with leakage correction and arterial spin labelling (ASL), respectively, from a 55-year-old male patient with a history of lung cancer and brain metastasis which was treated with high-dose radiation therapy. The ce-T1W image shows a ring-enhancing lesion adjacent to the left lateral ventricle with a waxing and waning course over time, suspicious of radiation necrosis. However, the lesion remained suspicious for metastasis recurrence due to the high rCBV as measured with DSC. CBF however is low, which is more consistent with the clinical diagnosis and time course of radiation necrosis. The discrepancy between findings with DSC and ASL is presumably due to leakage effects in the DSC images resulting in incorrect estimation of rCBV.

ce-T1w   rCBV (DSC)   CBF (ASL)
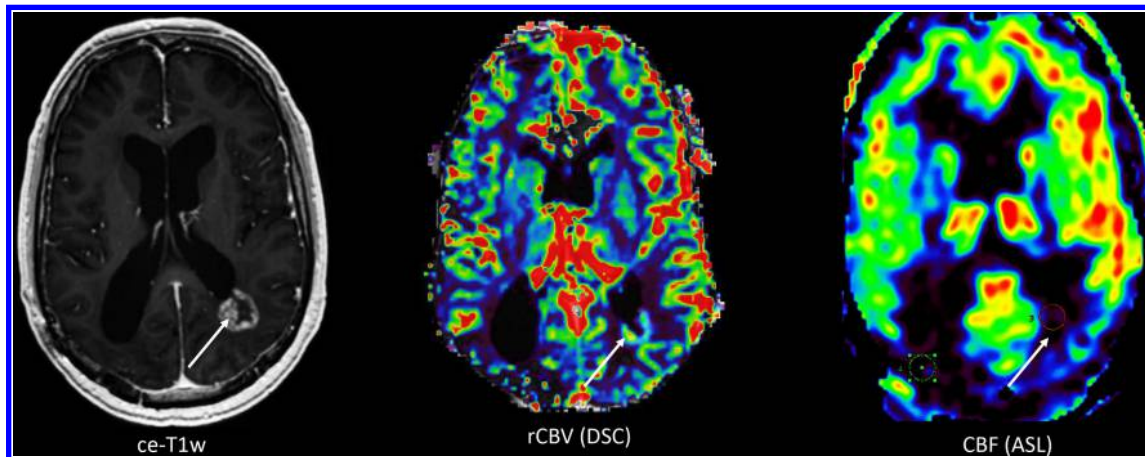
Radiomics and biomarkers

Quantitative imaging is an upcoming field in radiology research. The ability to detect and determine the magnitude of a signal change may help to differentiate between aetiologies in tissue of interest.

Radiomics uses the quantitative features from segmented images that are difficult or even impossible to detect by visual inspection, in order to find associations with clinically relevant outcomes.[78] Machine- and deep-learning techniques facilitate radiomics, by automatically extracting high-dimensional features from original images and learning to recognise characteristic patterns of pathology.[79] In BMs, radiomics has been evaluated to determine primary tumour type and mutational status, but also to evaluate tumour response after treatment.

Kniep et al used radiomics to determine the primary tumour type of BMs; melanoma and SCLC were well recognized by their model (area under the curve [AUC] of 0.80 and 0.74, respectively), but breast cancer and NSCLC were less well differentiated (AUC 0.61 and 0.63, respectively), which could be explained by the heterogeneity of BM characteristics in these types.[80] Park et al used radiomics to determine NSCLC subtypes: DTI and conventional post-contrast T1W imaging could potentially detect the EGFR mutational status in BMs from NSCLC.[81]

In treatment surveillance, radiomics is also widely studied. Peng et al retrospectively studied conventional and, when available, perfusion MRI of 66 patients with 82 BMs that showed a volume increase following SRS.[78] They compared radiomics obtained with machine learning with histopathologic diagnosis. Their model showed a promising accuracy for differentiation of true progression and RN, with an AUC of 0.81.[78] Two other studies also assessed radiomic models in predicting response after SRS

and found similar AUCs.[82,83] Lee et al used radiomics to assess intratumoural heterogeneity following SRS treatment.[65] They identified several potential imaging parameters, such as solid, low-enhancing regions and nonviable tissue regions (*e.g.,* non-enhancing T2 hyperintensity), to have a predictive power for tumour progression.[65] However, their work needs to be interpreted with caution due to several assumptions and lack of standard histopathological confirmation.[65]

Galldiks et al retrospectively investigated quantitative values from ^{18}F-FET-PET imaging in the follow-up of 40 patients with BMs after TT or ICI treatment.[84] Uptake of ^{18}F-FET in BMs was promising in differentiating between progression and PsPD after TT or ICI treatment. Also, ^{18}F-FET-PET showed promise in predicting response to treatment.

Since radiomics could provide information on specific tumour and treatment-related features, it is a promising tool to eventually obviate histopathological diagnosis or verification. However, straightforward, clinically "easy-to-interpret" biomarkers are limited as studies generally use indirect measures such as survival to estimate the implications of a biomarker, while at the same time accuracy requires further improvement.[77]

Although survival might not be the ideal reference standard for validating biomarkers, it is important to be able to estimate prognosis of individual patients. A clinically used and validated prognostic index, created by Sperduto et al, is the Graded Prognostic Assessment (GPA).[85] It combines clinical and molecular prognostic factors to predict prognosis of individual patients with BMs. Zakaria et al combined ADC values of DWI-MRI with existing survival prediction models such as the GPA.[86] Higher tumour ADC at initial BM diagnosis was associated with longer survival, and implementation of ADC values in the existing

models increased the accuracy of these models in predicting prognosis.

Endogenous MRI contrasts

New imaging techniques are constantly being developed. Chemical Exchange Saturation Transfer (CEST) is a technique assessing the concentrations of large molecules such as proteins (amide proton transfer, or APT-CEST) and glucose (glucoCEST).[52] Since BMs have both a higher protein concentration and higher rates of glucose metabolism than normal brain, these techniques are promising for detecting and characterising BMs.

Like CEST, new imaging techniques that provide contrast from endogenous molecules might substitute exogenous contrast agents such as GCBAs. An example is the replacement of DSC-MRI, for which commonly an increased dose of GBCA is used, with non-invasive perfusion imaging techniques. Vu et al demonstrated the use of blood-oxygen-level-dependent (BOLD) MRI, in which transient hypoxia was used to generate contrast.[87]

Optimised treatment delivery

Theranostics combines the diagnostic and therapeutic properties of radiolabelled compounds.[88] In the central nervous system, most theranostics were investigated in glioma. In BMs, the anti-prostate-specific membrane antibody (PSMA) is promising for theranostics. PSMA can be radiolabelled for both diagnosis using PET (Gallium 68 [^{69}Ga]-PSMA) and radionuclide therapy with Lutetium-117 [^{117}Lu]Lu-PSMA-617 and Actinium-225 [^{225}Ac]Ac-PSMA-616.[89] Therefore, theranostics seems to be a next step in optimised BM treatment.

The term "theranostics" is formally reserved for a single compound with both diagnostic and therapeutic abilities. However, PET tracers combined with certain compounds can also be used to predict response to treatment. An example is [^{89}Zr]-pertuzumab, studied in patients with breast cancer to detect human epidermal growth factor receptor 2 (HER2)-positive BMs and to determine optimal dosimetry.[90] Since HER2-positive BMs can be effectively treated with TT, patients can be optimally selected for this therapy. Furthermore, non-responders can be selected upfront, preventing unnecessary TT treatment and side effects.

Poor penetration of systemic drugs into BMs, due to features of the blood-brain-barrier and blood-tumour-barrier, has been a major concern limiting treatment efficacy. Focussed ultrasound has been suggested to improve drug delivery to BMs by opening the blood-brain-barrier and/or blood-tumour-barrier; this has been investigated in glioma and a small trial in patients with breast cancer BMs is currently ongoing.[91]

CONCLUSION

The management of patients with BMs greatly relies on imaging. Screening for BMs is indicated in oncologic subgroups with a higher risk for BMs. However, it is still a matter of debate whether earlier detection of BMs will improve outcome. MRI is the cornerstone of diagnosis and evaluation of BMs. In discriminating BMs from other intracranial lesions or treatment-related effects, more advanced imaging techniques such as perfusion MRI and PET can be of added value. Imaging can also guide local and advanced systemic treatments with increasing precision. Current studies show promise for new imaging biomarkers and contrasts, and in finding ways to optimise treatment of BMs. Ultimately, all these research efforts aim to improve survival and quality of life for patients with BMs.

FUNDING

REFERENCES

1. Dasgupta A, Co J, Winter J, Millar B-A, Laperriere N, Tsang DS, et al. Clinicopathologic and treatment features of long-term surviving brain metastasis patients. *Curr Oncol* 2021; **28**: 549–59. doi: https://doi.org/10.3390/curroncol28010054

2. Hall WA, Djalilian HR, Nussbaum ES, Cho KH. Long-term survival with metastatic cancer to the brain. *Med Oncol* 2000; **17**: 279–86. doi: https://doi.org/10.1007/BF02782192

3. Achrol AS, Rennert RC, Anders C, Soffietti R, Ahluwalia MS, Nayak L, et al. Brain metastases. *Nat Rev Dis Primers* 2019; **5**: 5. doi: https://doi.org/10.1038/s41572-018-0055-y

4. Goldberg SB, Gettinger SN, Mahajan A, Chiang AC, Herbst RS, Sznol M, et al. Pembrolizumab for patients with melanoma or non-small-cell lung cancer and untreated brain metastases: early analysis of a non-randomised, open-label, phase 2 trial. *Lancet Oncol* 2016; **17**: 976–83. doi: https://doi.org/10.1016/S1470-2045(16)30053-5

5. Tawbi HA, Forsyth PA, Algazi A, Hamid O, Hodi FS, Moschos SJ, et al. Combined nivolumab and ipilimumab in melanoma metastatic to the brain. *N Engl J Med* 2018; **379**: 722–30. doi: https://doi.org/10.1056/NEJMoa1805453

6. Niranjan A, Monaco E, Flickinger J, Lunsford LD. Guidelines for multiple brain metastases radiosurgery. *Prog Neurol Surg* 2019; **34**: 100–9. doi: https://doi.org/10.1159/000493055

7. Hartgerink D, Swinnen A, Roberge D, Nichol A, Zygmanski P, Yin F-F, et al. LINAC based stereotactic radiosurgery for multiple brain metastases: guidance for clinical implementation. *Acta Oncol* 2019; **58**: 1275–82. doi: https://doi.org/10.1080/0284186X.2019.1633016

8. Thust SC, van den Bent MJ, Smits M. Pseudoprogression of brain tumors. *J Magn Reson Imaging* 2018; **48**: 571–89. doi: https://doi.org/10.1002/jmri.26171

9. Galldiks N, Kocher M, Ceccon G, Werner J-M, Brunn A, Deckert M, et al. Imaging challenges of immunotherapy and targeted therapy in patients with brain metastases: response, progression, and pseudoprogression. *Neuro Oncol* 2020; **22**: 17–30. doi: https://doi.org/10.1093/neuonc/noz147

10. Lupattelli M, Alì E, Ingrosso G, Saldi S, Fulcheri C, Borghesi S, et al. Stereotactic radiotherapy for brain metastases: imaging

tools and Dosimetric predictive factors for radionecrosis. *J Pers Med* 2020; **10**: 59. doi: https://doi.org/10.3390/jpm10030059

11. Smith BD, Smith GL, Hurria A, Hortobagyi GN, Buchholz TA. Future of cancer incidence in the United States: burdens upon an aging, changing nation. *J Clin Oncol* 2009; **27**: 2758–65. doi: https://doi.org/10.1200/JCO.2008.20.8983

12. Nieder C, Spanne O, Mehta MP, Grosu AL, Geinitz H. Presentation, patterns of care, and survival in patients with brain metastases: what has changed in the last 20 years? *Cancer* 2011; **117**: 2505–12. doi: https://doi.org/10.1002/cncr.25707

13. Lu-Emerson C, Eichler AF. Brain metastases. *Continuum* 2012; **18**: 295–311. doi: https://doi.org/10.1212/01.CON.0000413659.12304.a6

14. Kaufmann TJ, Smits M, Boxerman J, Huang R, Barboriak DP, Weller M, et al. Consensus recommendations for a standardized brain tumor imaging protocol for clinical trials in brain metastases. *Neuro Oncol* 2020; **22**: 757–72. doi: https://doi.org/10.1093/neuonc/noaa030

15. Ostrom QT, Wright CH, Barnholtz-Sloan JS. Brain metastases: epidemiology. *Handb Clin Neurol* 2018; **149**: 27–42. doi: https://doi.org/10.1016/B978-0-12-811161-1.00002-5

16. Barnholtz-Sloan JS, Sloan AE, Davis FG, Vigneau FD, Lai P, Sawaya RE. Incidence proportions of brain metastases in patients diagnosed (1973 to 2001) in the metropolitan Detroit cancer surveillance system. *J Clin Oncol* 2004; **22**: 2865–72. doi: https://doi.org/10.1200/JCO.2004.12.149

17. Goncalves PH, Peterson SL, Vigneau FD, Shore RD, Quarshie WO, Islam K, et al. Risk of brain metastases in patients with nonmetastatic lung cancer: analysis of the metropolitan Detroit surveillance, epidemiology, and end results (SEER) data. *Cancer* 2016; **122**: 1921–7. doi: https://doi.org/10.1002/cncr.30000

18. Hubbs JL, Boyd JA, Hollis D, Chino JP, Saynak M, Kelsey CR. Factors associated with the development of brain metastases: analysis of 975 patients with early stage nonsmall cell lung cancer. *Cancer* 2010; **116**: 5038–46. doi: https://doi.org/10.1002/cncr.25254

19. Chen S, Hua X, Jia J, Wu Y, Wei S, Xu L, et al. Risk factors for brain metastases in patients with non-small cell lung cancer: a meta-analysis of 43 studies. *Ann Palliat Med* 2021; **10**: 3657–72. doi: https://doi.org/10.21037/apm-20-1722

20. Ando T, Kage H, Saito M, Amano Y, Goto Y, Nakajima J, et al. Early stage non-small cell lung cancer patients need brain imaging regardless of symptoms. *Int J Clin Oncol* 2018; **23**: 641–6. doi: https://doi.org/10.1007/s10147-018-1254-y

21. Wrona A. Management of CNS disease in ALK-positive non-small cell lung cancer: is whole brain radiotherapy still needed? *Cancer Radiother* 2019; **23**: 432–8. doi: https://doi.org/10.1016/j.canrad.2019.03.009

22. Cancer Statistics: World Health Organisation (WHO). 2020. Available from: https://www.cancer.gov/about-cancer/understanding/statistics.

23. Martin AM, Cagney DN, Catalano PJ, Warren LE, Bellon JR, Punglia RS, et al. Brain metastases in newly diagnosed breast cancer: a population-based study. *JAMA Oncol* 2017; **3**: 1069–77. doi: https://doi.org/10.1001/jamaoncol.2017.0001

24. Leone JP, Leone BA. Breast cancer brain metastases: the last frontier. *Exp Hematol Oncol* 2015; **4**: 33. doi: https://doi.org/10.1186/s40164-015-0028-8

25. Osella-Abate S, Ribero S, Sanlorenzo M, Maule MM, Richiardi L, Merletti F, et al. Risk factors related to late metastases in 1,372 melanoma patients disease free more than 10 years. *Int J Cancer* 2015; **136**: 2453–7. doi: https://doi.org/10.1002/ijc.29281

26. Zhang D, Wang Z, Shang D, Yu J, Yuan S. Incidence and prognosis of brain metastases in cutaneous melanoma patients: a population-based study. *Melanoma Res* 2019; **29**: 77–84. doi: https://doi.org/10.1097/CMR.0000000000000538

27. Gardner LJ, Ward M, Andtbacka RHI, Boucher KM, Bowen GM, Bowles TL, et al. Risk factors for development of melanoma brain metastasis and disease progression: a single-center retrospective analysis. *Melanoma Res* 2017; **27**: 477–84. doi: https://doi.org/10.1097/CMR.0000000000000382

28. Steindl A, Berghoff AS. Brain metastases in metastatic cancer: a review of recent advances in systemic therapies. *Expert Rev Anticancer Ther* 2021; **21**: 325–39. doi: https://doi.org/10.1080/14737140.2021.1851200

29. Shuch B, La Rochelle JC, Klatte T, Riggs SB, Liu W, Kabbinavar FF, et al. Brain metastasis from renal cell carcinoma: presentation, recurrence, and survival. *Cancer* 2008; **113**: 1641–8. doi: https://doi.org/10.1002/cncr.23769

30. Bonadio RC, Freitas GF, Batista DN, Moreira OAN, Dias CAR, Castria TB, et al. Epidemiology and outcomes of patients with brain metastases from colorectal Cancer-Who are these patients? *Clin Colorectal Cancer* 2021; **20**: e195–200. doi: https://doi.org/10.1016/j.clcc.2021.04.002

31. Yaeger R, Cowell E, Chou JF, Gewirtz AN, Borsu L, Vakiani E, et al. RAS mutations affect pattern of metastatic spread and increase propensity for brain metastasis in colorectal cancer. *Cancer* 2015; **121**: 1195–203. doi: https://doi.org/10.1002/cncr.29196

32. Cagney DN, Martin AM, Catalano PJ, Redig AJ, Lin NU, Lee EQ, et al. Incidence and prognosis of patients with brain metastases at diagnosis of systemic malignancy: a population-based study. *Neuro Oncol* 2017; **19**: 1511–21. doi: https://doi.org/10.1093/neuonc/nox077

33. Kim YZ, Kwon JH, Lim S. A clinical analysis of brain metastasis in gynecologic cancer: a retrospective multi-institute analysis. *J Korean Med Sci* 2015; **30**: 66–73. doi: https://doi.org/10.3346/jkms.2015.30.1.66

34. Levy A, Faivre-Finn C, Hasan B, De Maio E, Berghoff AS, Girard N, et al. Diversity of brain metastases screening and management in non-small cell lung cancer in Europe: results of the European organisation for research and treatment of cancer lung cancer group survey. *Eur J Cancer* 2018; **93**: 37–46. doi: https://doi.org/10.1016/j.ejca.2018.01.067

35. Hochstenbag MM, Twijnstra A, Wilmink JT, Wouters EF, ten Velde GP. Asymptomatic brain metastases (BM) in small cell lung cancer (SCLC): MR-imaging is useful at initial diagnosis. *J Neurooncol* 2000; **48**: 243–8. doi: https://doi.org/10.1023/A:1006427407281

36. Cagney DN, Martin AM, Catalano PJ, Brown PD, Alexander BM, Lin NU, et al. Implications of screening for brain metastases in patients with breast cancer and non-small cell lung cancer. *JAMA Oncol* 2018; **4**: 1001–3. doi: https://doi.org/10.1001/jamaoncol.2018.0813

37. Neugut AI, Sackstein P, Hillyer GC, Jacobson JS, Bruce J, Lassman AB, et al. Magnetic resonance imaging-based screening for asymptomatic brain tumors: a review. *Oncologist* 2019; **24**: 375–84. doi: https://doi.org/10.1634/theoncologist.2018-0177

38. Pope WB. Brain metastases: neuroimaging. *Handb Clin Neurol* 2018; **149**: 89–112. doi: https://doi.org/10.1016/B978-0-12-811161-1.00007-4

39. Fink JR, Muzi M, Peck M, Krohn KA. Multimodality brain tumor imaging: MR imaging, PET, and PET/MR imaging. *J Nucl Med* 2015; **56**: 1554–61. doi: https://doi.org/10.2967/jnumed.113.131516

40. Brindle KM, Izquierdo-García JL, Lewis DY, Mair RJ, Wright AJ. Brain tumor imaging. *J Clin Oncol* 2017; **35**: 2432–8. doi: https://doi.org/10.1200/JCO.2017.72.7636

41. GCTE G, Bockel S, Majer M, Ammari S, Smits M. Imaging of brain metastases: diagnosis and monitoring. *Central Nervous System Metastases* 2019: 145–58. doi: https://doi.org/10.1007/978-3-030-23417-1_12

42. Mills SJ, Thompson G, Jackson A. Advanced magnetic resonance imaging biomarkers of cerebral metastases. *Cancer Imaging* 2012; **12**: 245–52. doi: https://doi.org/10.1102/1470-7330.2012.0012

43. Planchard D, Popat S, Kerr K, Novello S, Smit EF, Faivre-Finn C, et al. Metastatic non-small cell lung cancer: ESMO clinical practice guidelines for diagnosis, treatment and follow-up. *Annals of Oncology* 2018; **29**(Suppl 4): iv192–237. doi: https://doi.org/10.1093/annonc/mdy275

44. Frankel TL, Bamboat ZM, Ariyan C, Coit D, Sabel MS, Brady MS. Predicting the development of brain metastases in patients with local/regional melanoma. *J Surg Oncol* 2014; **109**: 770–4.

45. Breckwoldt M, Bendszus M. [Cerebral MR imaging of malignant melanoma] Zerebrale MR-Bildgebung beim malignen Melanom. *Radiologe* 2015; **55**: 113–9.

46. Kato MK, Tanase Y, Uno M, Ishikawa M, Kato T. Brain metastases from uterine cervical and endometrial cancer. *Cancers* 2021; **13**: 519. doi: https://doi.org/10.3390/cancers13030519

47. Straub S, Laun FB, Freitag MT, Kölsche C, von Deimling A, Denoix M, et al. Assessment of melanin content and its influence on susceptibility contrast in melanoma metastases. *Clin Neuroradiol* 2020; **30**: 607–14. doi: https://doi.org/10.1007/s00062-019-00816-x

48. Haller S, Zaharchuk G, Thomas DL, Lovblad K-O, Barkhof F, Golay X. Arterial spin labeling perfusion of the brain: emerging clinical applications. *Radiology* 2016; **281**: 337–56. doi: https://doi.org/10.1148/radiol.2016150789

49. McKnight CD, Motuzas CL, Srinivasan A. Approach to brain neoplasms: what the oncologist wants to know. *Semin Roentgenol* 2018; **53**: 6–22. doi: https://doi.org/10.1053/j.ro.2017.11.002

50. Huang BY, Kwock L, Castillo M, Smith JK. Association of choline levels and tumor perfusion in brain metastases assessed with proton MR spectroscopy and dynamic susceptibility contrast-enhanced perfusion weighted MRI. *Technol Cancer Res Treat* 2010; **9**: 327–37. doi: https://doi.org/10.1177/153303461000900403

51. Li Y, Park I, Nelson SJ. Imaging tumor metabolism using in vivo magnetic resonance spectroscopy. *Cancer J* 2015; **21**: 123–8. doi: https://doi.org/10.1097/PPO.0000000000000097

52. Jones KM, Pollard AC, Pagel MD. Clinical applications of chemical exchange saturation transfer (CEST) MRI. *J Magn Reson Imaging* 2018; **47**: 11–27. doi: https://doi.org/10.1002/jmri.25838

53. Chen H, Pang Y, Wu J, Zhao L, Hao B, Wu J, et al. Comparison of [^{68}Ga]Ga-DOTA-FAPI-04 and [^{18}F] FDG PET/CT for the diagnosis of primary and metastatic lesions in patients with various types of cancer. *Eur J Nucl Med Mol Imaging* 2020; **47**: 1820–32. doi: https://doi.org/10.1007/s00259-020-04769-z

54. Pyatigorskaya N, Habert M-O, Rozenblum L. Contribution of PET-MRI in brain diseases in clinical practice. *Curr Opin Neurol* 2020; **33**: 430–8. doi: https://doi.org/10.1097/WCO.0000000000000841

55. Wang JL, Elder JB. Techniques for open surgical resection of brain metastases. *Neurosurg Clin N Am* 2020; **31**: 527–36. doi: https://doi.org/10.1016/j.nec.2020.06.003

56. Soffietti R, Abacioglu U, Baumert B, Combs SE, Kinhult S, Kros JM, et al. Diagnosis and treatment of brain metastases from solid tumors: guidelines from the European Association of Neuro-Oncology (EANO). *Neuro Oncol* 2017; **19**: 162–74. doi: https://doi.org/10.1093/neuonc/now241

57. Kiesel B, Thomé CM, Weiss T, Jakola AS, Darlix A, Pellerino A, et al. Perioperative imaging in patients treated with resection of brain metastases: a survey by the European Association of Neuro-Oncology (EANO) Youngsters Committee. *BMC Cancer* 2020; **20**: 410. doi: https://doi.org/10.1186/s12885-020-06897-z

58. Salem U, Kumar VA, Madewell JE, Schomer DF, de Almeida Bastos DC, Zinn PO, et al. Neurosurgical applications of MRI guided laser interstitial thermal therapy (LITT). *Cancer Imaging* 2019; **19**: 65. doi: https://doi.org/10.1186/s40644-019-0250-4

59. Teyateeti A, Brown PD, Mahajan A, Laack NN, Pollock BE. Brain metastases resection cavity radio-surgery based on T2-weighted MRI: technique assessment. *J Neurooncol* 2020; **148**: 89–95. doi: https://doi.org/10.1007/s11060-020-03492-x

60. Putz F, Mengling V, Perrin R, Masitho S, Weissmann T, Rösch J. Magnetic resonance imaging for brain stereotactic radiotherapy : A review of requirements and pitfalls Magnetresonanztomographie für die stereotaktische Strahlentherapie des Gehirns: Anforderungen und Fehlerquellen – eine Übersicht. *Strahlenther Onkol* 2020; **196**: 444–56.

61. Benveniste RJ, Yechieli R, Diwanji T. Early magnetic resonance imaging after gamma knife radiosurgery of brain metastases. *World Neurosurg* 2021; **146**: e1177–81. doi: https://doi.org/10.1016/j.wneu.2020.11.119

62. Long GV, Trefzer U, Davies MA, Kefford RF, Ascierto PA, Chapman PB, et al. Dabrafenib in patients with Val600Glu or Val600Lys BRAF-mutant melanoma metastatic to the brain (BREAK-MB): a multicentre, open-label, phase 2 trial. *Lancet Oncol* 2012; **13**: 1087–95. doi: https://doi.org/10.1016/S1470-2045(12)70431-X

63. Okada H, Weller M, Huang R, Finocchiaro G, Gilbert MR, Wick W, et al. Immunotherapy response assessment in neuro-oncology: a report of the RANO working group. *Lancet Oncol* 2015; **16**: e534–42. doi: https://doi.org/10.1016/S1470-2045(15)00088-1

64. Lin NU, Lee EQ, Aoyama H, Barani IJ, Barboriak DP, Baumert BG, et al. Response assessment criteria for brain metastases: proposal from the RANO group. *Lancet Oncol* 2015; **16**: e270–8. doi: https://doi.org/10.1016/S1470-2045(15)70057-4

65. Lee DH, Park JE, Kim N, Park SY, Kim Y-H, Cho YH, et al. Tumor habitat analysis by magnetic resonance imaging distinguishes tumor progression from radiation necrosis in brain metastases after stereotactic radiosurgery. *Eur Radiol* 2021. doi: https://doi.org/10.1007/s00330-021-08204-1

66. Chukwueke UN, Wen PY. Use of the Response Assessment in Neuro-Oncology (RANO) criteria in clinical trials and clinical practice. *CNS Oncol* 2019; **8**: CNS28. doi: https://doi.org/10.2217/cns-2018-0007

67. Kohutek ZA, Yamada Y, Chan TA, Brennan CW, Tabar V, Gutin PH, et al. Long-term risk of radionecrosis and imaging changes after stereotactic radiosurgery for brain metastases. *J Neurooncol* 2015; **125**: 149–56. doi: https://doi.org/10.1007/s11060-015-1881-3

68. Muto M, Frauenfelder G, Senese R, Zeccolini F, Schena E, Giurazza F, et al. Dynamic susceptibility contrast (DSC) perfusion MRI in differential diagnosis between radionecrosis and neoangiogenesis in cerebral metastases using rCBV, rCBF and K2. *Radiol Med* 2018; **123**: 545–52. doi: https://doi.org/10.1007/s11547-018-0866-7

69. Hu LS, Baxter LC, Smith KA, Feuerstein BG, Karis JP, Eschbacher JM, et al. Relative cerebral blood volume values to differentiate high-grade glioma recurrence from posttreatment radiation effect: direct correlation between image-guided tissue histopathology and localized dynamic susceptibility-weighted contrast-enhanced

perfusion MR imaging measurements. *AJNR Am J Neuroradiol* 2009; **30**: 552–8. doi: https://doi.org/10.3174/ajnr.A1377

70. Morabito R, Alafaci C, Pergolizzi S, Pontoriero A, Iati' G, Bonanno L, et al. DCE and DSC perfusion MRI diagnostic accuracy in the follow-up of primary and metastatic intra-axial brain tumors treated by radiosurgery with cyberknife. *Radiat Oncol* 2019; **14**: 65. doi: https://doi.org/10.1186/s13014-019-1271-7

71. Knitter JR, Erly WK, Stea BD, Lemole GM, Germano IM, Doshi AH, et al. Interval change in diffusion and perfusion MRI parameters for the assessment of pseudoprogression in cerebral metastases treated with stereotactic radiation. *AJR Am J Roentgenol* 2018; **211**: 168–75. doi: https://doi.org/10.2214/AJR.17.18890

72. Taunk NK, Oh JH, Shukla-Dave A, Beal K, Vachha B, Holodny A, et al. Early posttreatment assessment of MRI perfusion biomarkers can predict long-term response of lung cancer brain metastases to stereotactic radiosurgery. *Neuro Oncol* 2018; **20**: 567–75. doi: https://doi.org/10.1093/neuonc/nox159

73. Shah AD, Shridhar Konar A, Paudyal R, Oh JH, LoCastro E, Nuñez DA, et al. Diffusion and perfusion MRI predicts response preceding and shortly after radiosurgery to brain metastases: a pilot study. *J Neuroimaging* 2021; **31**: 317–23. doi: https://doi.org/10.1111/jon.12828

74. Weybright P, Sundgren PC, Maly P, Hassan DG, Nan B, Rohrer S, et al. Differentiation between brain tumor recurrence and radiation injury using MR spectroscopy. *AJR Am J Roentgenol* 2005; **185**: 1471–6. doi: https://doi.org/10.2214/AJR.04.0933

75. Ceccon G, Lohmann P, Stoffels G, Judov N, Filss CP, Rapp M, et al. Dynamic O-(2-18F-fluoroethyl)-L-tyrosine positron emission tomography differentiates brain metastasis recurrence from radiation injury after radiotherapy. *Neuro Oncol* 2017; **19**: 281–8. doi: https://doi.org/10.1093/neuonc/now149

76. Cicone F, Minniti G, Romano A, Papa A, Scaringi C, Tavanti F, et al. Accuracy of F-DOPA PET and perfusion-MRI for differentiating radionecrotic from progressive brain metastases after radiosurgery. *Eur J Nucl Med Mol Imaging* 2015; **42**: 103–11. doi: https://doi.org/10.1007/s00259-014-2886-4

77. Aneja S, Omuro A. Imaging biomarkers for brain metastases: more than meets the eye. *Neuro Oncol* 2019; **21**: 1493–4. doi: https://doi.org/10.1093/neuonc/noz193

78. Peng L, Parekh V, Huang P, Lin DD, Sheikh K, Baker B, et al. Distinguishing true progression from radionecrosis after stereotactic radiation therapy for brain metastases with machine learning and radiomics. *Int J Radiat Oncol Biol Phys* 2018; **102**: 1236–43. doi: https://doi.org/10.1016/j.ijrobp.2018.05.041

79. Lohmann P, Kocher M, Ruge MI, Visser-Vandewalle V, Shah NJ, Fink GR, et al. PET/MRI Radiomics in patients with brain metastases. *Front Neurol* 2020; **11**: 1. doi: https://doi.org/10.3389/fneur.2020.00001

80. Kniep HC, Madesta F, Schneider T, Hanning U, Schönfeld MH, Schön G, et al. Radiomics of brain MRI: utility in prediction of metastatic tumor type. *Radiology* 2019; **290**: 479–87. doi: https://doi.org/10.1148/radiol.2018180946

81. Park YW, An C, Lee J, Han K, Choi D, Ahn SS, et al. Diffusion tensor and postcontrast T1-weighted imaging radiomics to differentiate the epidermal growth factor receptor mutation status of brain metastases from non-small cell lung cancer. *Neuroradiology* 2021; **63**: 343–52. doi: https://doi.org/10.1007/s00234-020-02529-2

82. Karami E, Soliman H, Ruschin M, Sahgal A, Myrehaug S, Tseng C-L, et al. Quantitative MRI biomarkers of stereotactic radiotherapy outcome in brain metastasis. *Sci Rep* 2019; **9**: 19830. doi: https://doi.org/10.1038/s41598-019-56185-5

83. Cha YJ, Jang WI, Kim M-S, Yoo HJ, Paik EK, Jeong HK, et al. Prediction of response to stereotactic radiosurgery for brain metastases using Convolutional neural networks. *Anticancer Res* 2018; **38**: 5437–45. doi: https://doi.org/10.21873/anticanres.12875

84. Galldiks N, Abdulla DSY, Scheffler M, Wolpert F, Werner J-M, Hüllner M, et al. Treatment Monitoring of Immunotherapy and Targeted Therapy Using ^{18}F-FET PET in Patients with Melanoma and Lung Cancer Brain Metastases: Initial Experiences. *J Nucl Med* 2021; **62**: 464–70. doi: https://doi.org/10.2967/jnumed.120.248278

85. Sperduto PW, Kased N, Roberge D, Xu Z, Shanley R, Luo X, et al. Summary report on the graded prognostic assessment: an accurate and facile diagnosis-specific tool to estimate survival for patients with brain metastases. *J Clin Oncol* 2012; **30**: 419–25. doi: https://doi.org/10.1200/JCO.2011.38.0527

86. Zakaria R, Chen YJ, Hughes DM, Wang S, Chawla S, Poptani H, et al. Does the application of diffusion weighted imaging improve the prediction of survival in patients with resected brain metastases? A retrospective multicenter study. *Cancer Imaging* 2020; **20**: 16. doi: https://doi.org/10.1186/s40644-020-0295-4

87. Vu C, Chai Y, Coloigner J, Nederveen AJ, Borzage M, Bush A, et al. Quantitative perfusion mapping with induced transient hypoxia using BOLD MRI. *Magn Reson Med* 2021; **85**: 168–81. doi: https://doi.org/10.1002/mrm.28422

88. Moek KL, Giesen D, Kok IC, de Groot DJA, Jalving M, Fehrmann RSN, et al. Theranostics using antibodies and Antibody-Related therapeutics. *J Nucl Med* 2017; **58**(Supplement 2): 83S–90. doi: https://doi.org/10.2967/jnumed.116.186940

89. Pruis IJ, van Dongen GAMS, Veldhuijzen van Zanten SEM. The added value of diagnostic and theranostic PET imaging for the treatment of CNS tumors. *Int J Mol Sci* 2020; **21**: 1029. doi: https://doi.org/10.3390/ijms21031029

90. Ulaner GA, Lyashchenko SK, Riedl C, Ruan S, Zanzonico PB, Lake D, et al. First-in-human human epidermal growth factor receptor 2-targeted imaging using [89]Zr-pertuzumab PET/CT: dosimetry and clinical application in patients with breast cancer. *J Nucl Med* 2018; **59**: 900–6. doi: https://doi.org/10.2967/jnumed.117.202010

91. Curley CT, Stevens AD, Mathew AS, Stasiak K, Garrison WJ, Miller GW, et al. Immunomodulation of intracranial melanoma in response to blood-tumor barrier opening with focused ultrasound. *Theranostics* 2020; **10**: 8821–33. doi: https://doi.org/10.7150/thno.47983

FEMALE GENITOURINARY ONCOLOGY SPECIAL FEATURE: REVIEW ARTICLE

Ovary: MRI characterisation and O-RADS MRI

[1]ELIZABETH A SADOWSKI, MD, FSAR, [2]KATHERINE E MATUREN, MD, MS, [3]ANDREA ROCKALL, MRCP, FRCR, [4]CAROLINE REINHOLD, MD, MSc, [5]HELEN ADDLEY, BMBCh, MRCP, FRCR, [6]PRIYANKA JHA, MD, [7]NISHAT BHARWANI, BSc, MBBS, MRCP, FRCR and [8]ISABELLE THOMASSIN-NAGGARA, MD

[1]Departments of Radiology, Obstetrics and Gynecology, University of Wisconsin School of Medicine and Public Health, Madison, WI, USA
[2]Department of Radiology and Obstetrics and Gynecology, University of Michigan, Ann Arbor, MI, USA
[3]Division of Surgery and Cancer, Imperial College London, London, UK
[4]McGill University Health Center, McGill University, Montreal, Canada
[5]Cambridge University Hospitals NHS Foundation Trust, Cambridge, UK
[6]Department of Radiology, University of California San Francisco, San francisco, CA, USA
[7]Department of Radiology, St Mary's Hospital, Imperial College Healthcare NHS Trust, London, UK
[8]Sorbonne Université, Paris, France

Address correspondence to: Elizabeth A Sadowski
E-mail: *ESadowski@uwhealth.org*

ABSTRACT

Ultrasound has a high specificity for the diagnosis of a benign lesion in cases of classic appearing simple cyst, hemorrhagic cyst, endometrioma and dermoid. However, ultrasound can sometimes be limited for definitive characterisation and risk stratification of other types of lesions, including those with echogenic content that may appear solid, with or without blood flow. Frequently, MRI can be used to further characterise these types of lesions, due to its ability to distinguish solid tissue from non-tissue solid components such as fat, blood, or debris. Incorporating the MR imaging into the evaluation of adnexal lesions can improve diagnostic certainty and guide clinical management potentially avoiding inappropriate surgery for benign lesions and expediting appropriate treatment for malignant lesions, particularly in the females with sonographically indeterminate adnexal lesions.

INTRODUCTION

The estimated prevalence of adnexal lesions found on ultrasound is approximately 15% in the general population.[1–4] Patients with adnexal lesions are managed based on the imaging appearance of the lesion and clinical parameters, such as history and serum tumour markers.[5–11] Radiologists play a key role in assessing whether an adnexal lesion is benign appearing or has malignant features, and there are many imaging-based scoring systems available.[7,10,12,13] Accurately characterising adnexal lesions on imaging can avoid inappropriate surgery in benign lesions and expeditiously triage suspected cancers to a gynaecological oncologist. Furthermore, MRI can classify the subtype of ovarian neoplasm and stage of the disease. This allows for the clinical team to tailor treatment options, which has been shown to improve clinical outcomes.[14–17] For example, females with benign and borderline tumours on pre-operative imaging can be counselled and offered fertility-sparing surgery, while females with potentially invasive cancers can be referred for complete staging surgery.[18–21]

In a majority of patients with adnexal lesions, ultrasound can be used as a standalone imaging exam. For example, if a simple cyst, haemorrhagic cyst, endometrioma or dermoid are seen, these can be confidently diagnosed as benign with less than a 1% chance of malignancy.[7,9,22,23] However, when there is a lesion that does not have classic features for one of these four types of lesions, there is a risk of malignancy ranging from approximately 10% to greater than 50%.[7,13,23–25] In these cases, correlation with clinical history and laboratory assessment and/or further assessment with MRI has been shown to increase the accuracy for predicting the risk of malignancy.[26–33]

MRI can accurately classify adnexal lesions increasing the specificity for the diagnosis of malignancy in sonographically indeterminate adnexal lesions to 93%.[34] Furthermore, the presence of enhancing solid tissue indicates a potentially malignant lesion, whereas the absence of any enhancement is a reliable sign of benignity.[12,33,35–39] When solid tissue is present, its signal characteristics on T_2 weighted images (T_2 WI), diffusion weighted images (DWI) and on

Figure 1. This figure is reproduced by permission of ACR. O-RADS MRI Risk Stratification System. ^Approximate PPV based on data from Thomassin-Naggara, et al. O-RADS MRI Score for Risk Stratification of Sonographically Indeterminate Adnexal Masses. *JAMA Network Open*. 2020;3(1):e1919896. Please note that the PPV provided applies to the score category overall and not to individual characteristics. Definitive PPV are not currently available for individual characteristics. The PPV values for malignancy include both borderline tumours and invasive cancers. * Solid tissue is defined as a lesion component that enhances and conforms to one of these morphologies: papillary projection, mural nodule, irregular septation/wall or other larger solid portions. ** Minimal enhancement of Rokitansky nodules in lesion containing lipid does not change to O-RADS MRI 4. *** Hemorrhagic cyst ≤3 cm in pre-menopausal female is O-RADS MRI 1. DCE, Dynamic contrast enhancement with a time resolution of 15 sec or less; DWI, Diffusion weighted images PPV, positive predictive value.

O-RADS MRI Score	Risk Category	Positive Predictive Value for Malignancy^	Lexicon Description
0	Incomplete Evaluation	N/A	N/A
1	Normal Ovaries	N/A	No ovarian lesion
			Follicle defined as simple cyst ≤ 3 cm in a premenopausal woman
			Hemorrhagic cyst ≤ 3 cm in a premenopausal woman
			Corpus luteum +/- hemorrhage ≤ 3 cm in a premenopausal woman
2	Almost Certainly Benign	<0.5%^	Cyst: Unilocular- any type of fluid content ▪ No wall enhancement ▪ No enhancing solid tissue*
			Cyst: Unilocular – simple or endometriotic fluid content ▪ Smooth enhancing wall ▪ No enhancing solid tissue
			Lesion with lipid content** ▪ No enhancing solid tissue
			Lesion with "dark T2/dark DWI" solid tissue ▪ Homogeneously hypointense on T2 and DWI
			Dilated fallopian tube - simple fluid content ▪ Thin, smooth wall/endosalpingeal folds with enhancement ▪ No enhancing solid tissue
			Para-ovarian cyst – any type of fluid ▪ Thin, smooth wall +/- enhancement ▪ No enhancing solid tissue
3	Low Risk	~5%^	Cyst: Unilocular – proteinaceous, hemorrhagic or mucinous fluid content*** ▪ Smooth enhancing wall ▪ No enhancing solid tissue
			Cyst: Multilocular - Any type of fluid, no lipid content ▪ Smooth septae and wall with enhancement ▪ No enhancing solid tissue
			Lesion with solid tissue (excluding T2 dark/DWI dark) ▪ Low risk time intensity curve on DCE MRI
			Dilated fallopian tube – ▪ Non-simple fluid: Thin wall /folds ▪ Simple fluid: Thick, smooth wall/ folds ▪ No enhancing solid tissue
4	Intermediate Risk	~50%^	Lesion with solid tissue (excluding T2 dark/DWI dark) ▪ Intermediate risk time intensity curve on DCE MRI ▪ If DCE MRI is not feasible, score 4 is any lesion with solid tissue (excluding T2 dark/DWI dark) that is enhancing ≤ myometrium at 30-40s on non-DCE MRI
			Lesion with lipid content ▪ Large volume enhancing solid tissue
5	High Risk	~90%^	Lesion with solid tissue (excluding T2 dark/DWI dark) ▪ High risk time intensity curve on DCE MRI ▪ If DCE MRI is not feasible, score 5 is any lesion with solid tissue (excluding T2 dark/DWI dark) that is enhancing > myometrium at 30-40s on non-DCE MRI
			Peritoneal, mesenteric or omental nodularity or irregular thickening with or without ascites

post-contrast T_1 weighted images (T_1WI) can many times distinguish between benign, borderline and invasive tumours.[33,34,37–39] Recently, a codified risk score assessment, O-RADS MRI risk stratification system, was developed and validated in a large prospective, multicentre European study demonstrating an accuracy of 91% for the diagnosis of malignancy[10,34] (Figure 1). This scoring system is based on the appearance of the adnexal lesion on MRI and assigns a numerical score from 1 to 5. The higher the risk score, the greater the risk of malignancy. This article reviews the use of the O-RADS MRI score in the assessment of malignancy risk in adnexal lesions seen on MRI.

Adnexal lesions: MRI assessment and the O-RADS MRI risk score
MRI scanning technique
MRI analysis of adnexal lesions is best achieved using a 1.5 or 3 T scanner. Patient preparation may include asking the patient to fast prior to the exam and allowing the patient to void just prior to entering the scanner. Antiperistaltic agents also help to optimise the MRI images. The imaging protocol should include a pre-contrast axial T_1WI series, T_2WI series (preferably in two planes), DWI series and a post-contrast T_1WI series. There

Figure 2. Time–intensity curve comparing the enhancing solid tissue in adnexal lesions to the enhancement of the myometrium. (a) Low risk curve with no shoulder and a gradual increase in enhancement over time. (b) Intermediate risk curve with a shoulder and initial slope of enhancement less than or equal to the myometrium. (c) High risk curve with a shoulder and initial slope of enhancement greater than the myometrium.
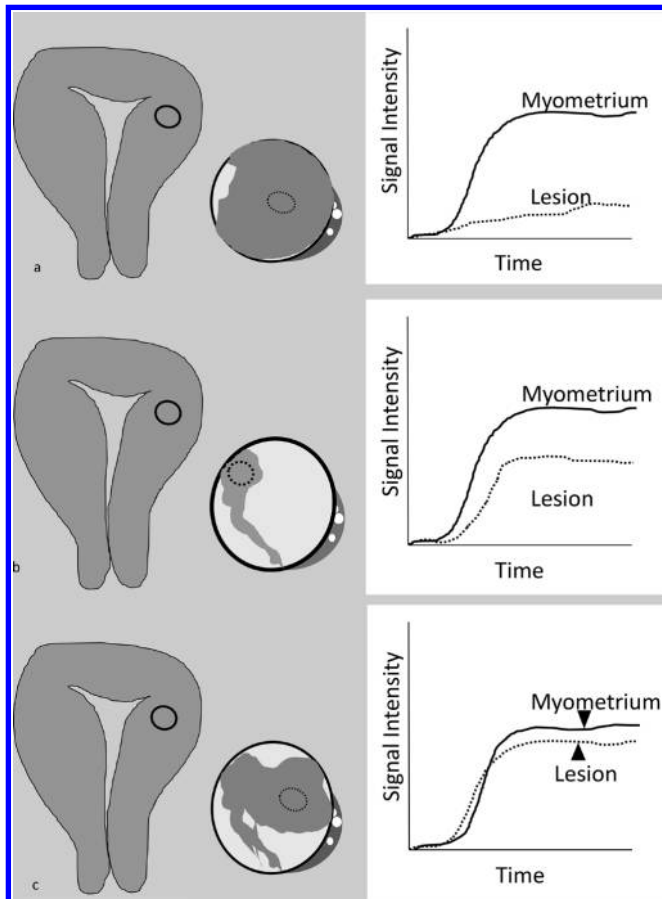
should be a fat saturated and non-fat saturated set of either T_1WI or T_2WI in order to detect macroscopic fat within the lesion, as well as in-phase and out-of-phase T_1WI to detect intra voxel fat. A slice thickness of 3 mm or less for the T_2WI and contrast-enhanced T_1WI is recommended to assure the proper resolution for detecting small papillary projections. The high B-value acquisition on DWI should have a B-value greater or equal to 1000. Performing a dynamic contrast-enhanced MRI series (temporal resolution $\leq$15 sec) and time–intensity curve (TIC) analysis is recommended. From the DCE MRI series, TIC curves for the solid tissue identified within the adnexal lesion and the outer myometrium should be generated using commercially available perfusion analysis software, to determine if a low risk, intermediate risk, or high risk curve is present (Figure 2). In the absence of a uterus, the curve analysis can only differentiate low risk curve (no shoulder) from intermediate/high risk curves (shoulder with plateau). If DCE MRI is not possible, a T_1WI series at 30–40 sec post-contrast injection can be performed instead, however, this

will limit evaluation and adnexal lesions with enhancing solid tissue will only be able to be scored as O-RADS MRI 4 or 5.

O-RADS MRI risk stratification system: when it should be used

It is beneficial to refer adnexal lesions to MRI for further characterisation when ultrasound is unable to classify the lesion as a classic benign entity (simple or haemorrhagic cyst, dermoid, or endometrioma) or when the lesion is considered indeterminate for malignancy. When a lesion has indeterminate ultrasound features, the positive predictive value for malignancy has a broad range from 7 to 50%.[7,13,24,35,40] When these lesions are assessed with MRI using the O-RADS MRI Risk score, the positive predictive value for cancer increases to 71%. Equally important is the scores negative predictive value of 98%, which is very reassuring to the treating physician and ultimately in supporting conservative management of the adnexal lesion.

There are guiding principles for applying the O-RADS MRI risk stratification system to the characterisation of adnexal lesions (Figure 1). First, the system was designed for an average risk population of females without acute symptoms. Its performance in high-risk females is unknown and in the acute setting, the score may not be diagnostically accurate in the assessment of the adnexal lesion. Second, clinical history and laboratory assessment should guide treatment of the patient in addition to the imaging features. Lastly, if the adnexal lesion has a classic appearance, a final diagnosis (*e.g.* dermoid, granulosa cell tumour, papillary serous tumours, peritoneal pseudocyst, etc.) can be reported in addition to the O-RADS MRI risk score.

O-RADS MRI risk stratification system: how to use it

Assessing a suspected lesion in the female pelvis begins with determining if the observation on MRI is adnexal in origin and if the observation is truly an adnexal lesion. If the lesion is not associated with the ovary or adnexa, the O-RADS MRI risk score should not be used. An adnexal lesion is defined as an observation associated with the ovary or adnexa that is not part of normal physiology. Follicles and corpus luteal cysts are not considered adnexal lesions, and if these are the only findings in the adnexa, the exam is assigned an O-RADS MRI score 1.

Once it has been determined there is an adnexal lesion, assessment for enhancement of any portion of the lesion should be performed. If there is no enhancement present, the lesion is assigned an O-RADS MRI score 2 (Figure 3). If there is enhancement of the lesion, then the next steps in the assessment are to determine the absence or presence of lipid content, whether there is wall enhancement and any enhancing solid tissue.

Lipid content is hyperintense on T_2WI and T_1WI with a visible decrease in signal on fat-saturated imaging. Microscopic or intravoxel fat is best depicted on opposed phase images and may not exhibit signal loss on fat saturated images in the way macroscopic fat does. If lipid content is present, the lesion is assigned an O-RADS score 2 and the diagnosis of dermoid or mature teratoma can be made. Dermoids may have both wall/

Figure 3. Example of an O-RADS MRI score two lesion with no enhancement on sagittal T_1WI (a), T_2WI (b) and post-contrast T_1WI (c). Unilocular adnexal cyst with T_2 hyperintense fluid (black asterisk), T_1 hypointense fluid (white asterisk), and no significant wall enhancement on the post-contrast T_1WI (arrows). T_1WI, T_1
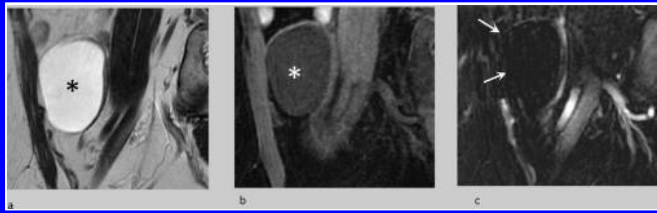
septal enhancement and can contain an enhancing Rokitansky nodule (Figure 4). If a Rokitansky nodule is present, the dermoid is still assigned an O-RADS MRI score 2. However, one caveat to keep in mind is that there is a minimal risk of malignant transformation in dermoids and there is a small risk of an immature teratoma if the patient is young. Malignant degeneration of a dermoid or an immature teratoma can be suspected if there is a large enhancing component with irregular margins, and the lesion would be assigned an O-RADS MRI score 4.

If the adnexal lesion does not contain lipid, and wall enhancement is noted but no other enhancing components are present, the fluid content of the lesion should be analysed on T_1WI and T_2WI. Simple fluid follows the signal intensity of cerebral spinal fluid or urine on T_1WI and T_2WI, exhibiting hypointense signal on T_1WI and hyperintense signal on T_2WI. Endometriotic fluid exhibits hyperintense signal on T_1WI and hypointense/intermediate signal on T_2WI, also known as shading.[41] Haemorrhagic fluid has variable signal depending on the age of the blood, and in the late acute phase can appear as hyperintense in signal on T_1WI and T_2WI.[42] Proteinaceous fluid is variable in signal,

Figure 4. Example of a dermoid (O-RADS MRI score 2) on selected axial T_2WI (a), T_1WI (b), fat-saturated T_1WI prior to administration of intravenous gadolinium (c), and subtraction post-contrast T_1WI (d). This right ovarian dermoid has layering fat (black asterisks), which has signal loss on the fat-suppressed T_1W (white asterisk). There is an enhancing Rokitansky nodule (white arrows). T_1WI, T_1 weighted imaging.

Figure 5. O-RADS MRI score 2 example on selected axial T_2WI (a), fat-saturated T_1WI (b), and subtraction post-contrast T_1WI (c). Multilocular endometrioma with locules of fluid that exhibit variable T_2 hypointense signal (white asterisks) and variable hyperintense T_1 signal (black asterisks), suggesting blood products of different age. There is enhancement of smooth septations and of the smooth wall (arrowheads). T_1WI, T_1 weighted imaging.
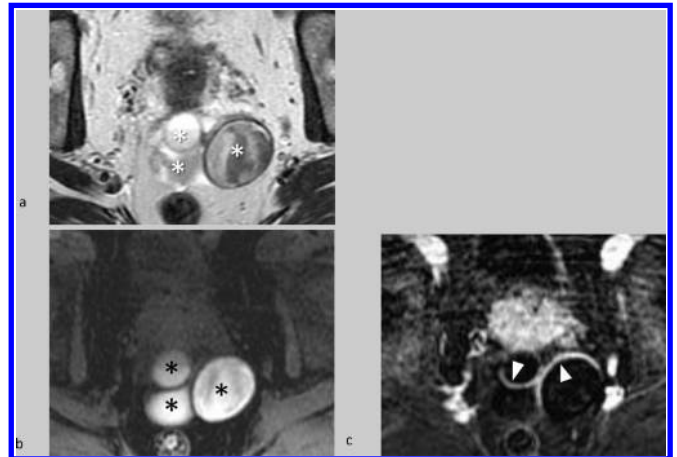
and can be hypointense/intermediate signal on T_2WI and can exhibit any type of signal intensity on T_1WI. If the lesion has wall enhancement and contains simple or endometriotic fluid, the lesion is assigned an O-RADS MRI score 2 (Figure 5). If the lesion has wall enhancement and haemorrhagic or proteinaceous fluid, the lesion is assigned an O-RADS MRI score 3 (Figure 6). One exception is in pre-menopausal females, a haemorrhagic cyst measuring ≤3 cm is assigned an O-RADS MRI score 2.

If the adnexal lesion does not contain lipid, and on interrogation there is solid tissue present, then assessment of the signal intensity of the solid tissue and the type of enhancement is the next step. Both benign and malignant lesions can have solid tissue on MRI. The O-RADS MRI definition of solid tissue is a solid component that enhances and appears as a papillary projection, mural nodule, or irregular septation/wall (Figure 7). The solid tissue seen on MRI should be interrogated to determine the signal intensity on T_2WI, high B-value DWI ($B \geq 1000$) and the enhancement pattern. This analysis is helpful in both the diagnosis and assignment of the O-RADS MRI score.
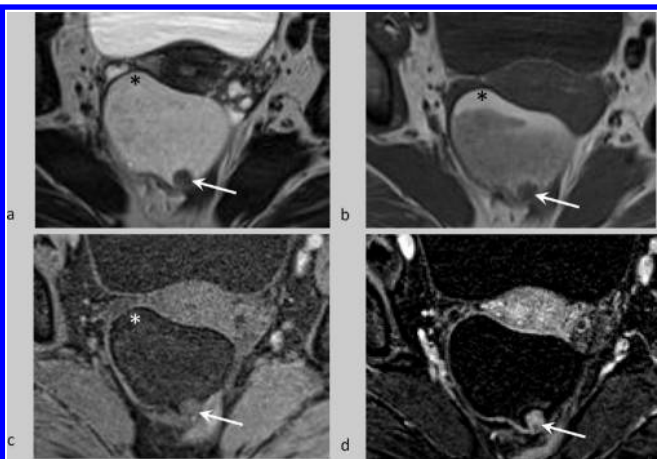
Figure 6. O-RADS MRI score 3 example on selected axial T_2WI (a), fat-saturated T_1WI (b), and subtraction post-contrast T_1WI (c). Haemorrhagic cyst with fluid that is T_2 and T_1 hyperintense, and an enhancing wall (arrowheads). T_1WI, T_1 weighted imaging.
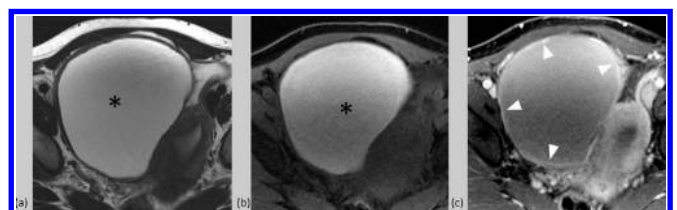
Figure 7. Example of solid tissue, which is by definition, solid components of an adnexal lesion that enhance and conform to one of these morphologic categories: irregular septations, nodules, papillary projections, or solid lesion. Clear cell carcinoma on selected axial T_2WI (a), high B-value DWI (b), and post-contrast T_1WI (c) with enhancing nodules (arrows) along the posterior wall of the lesion. DWI, diffusion-weighted imaging; T_1WI, T_1 weighted imaging.
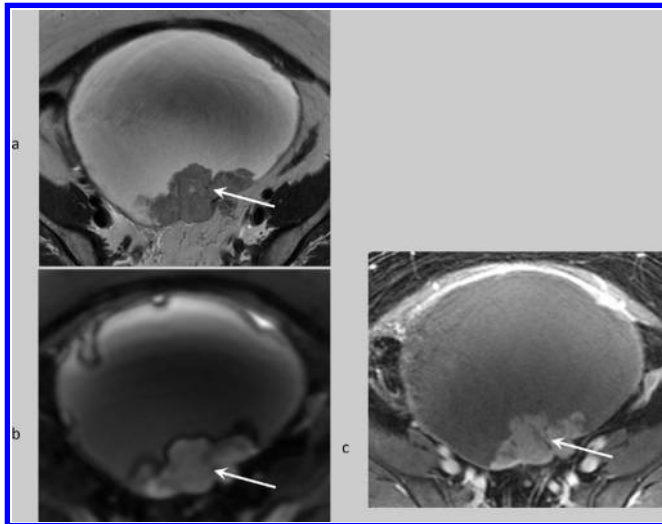
If the signal of the solid tissue is homogenously dark signal on T_2WI and the high B-value DWI (termed dark T2 dark/dark DWI), then the lesion is assigned an O-RADS MRI Score 2 and most likely represents a fibrous tumour, such as an ovarian fibroma (Figure 8). If there is solid tissue in the lesion that is heterogeneous in signal or isointense/hyperintense on T_2WI and high signal (higher than the urine) on the high B-value DWI, then assessing the enhancement pattern will be important to assign an O-RADS MRI risk score. On dynamic MRI, a lesion with a low risk TIC is assigned a O-RADS MRI score 3, an intermediate risk TIC is assigned a O-RADS MRI score 4 and high risk TIC is assigned a O-RADS MRI score 5 (Figure 9). DCE MRI is the recommended method for assessing enhancement, however if a dynamic acquisition is not possible, comparing the enhancement of the solid tissue to the outer myometrium at 30–40 sec post-contrast injection can be made. An adnexal lesion

Figure 8. Example of a dark T2/dark DWI adnexal lesion scored a O-RADS MRI 2. Ovarian fibroma (arrows) on selected axial T_2WI (a) and $B = 1000$ DWI (b) which is homogeneous hypointense on T2 and the high B-value DWI image (dark T2/dark DWI) and the same signal intensity characteristics as the incidental uterine fibroid (arrowheads) in keeping with a lesion containing fibrous material. DWI, diffusion-weighted imaging.
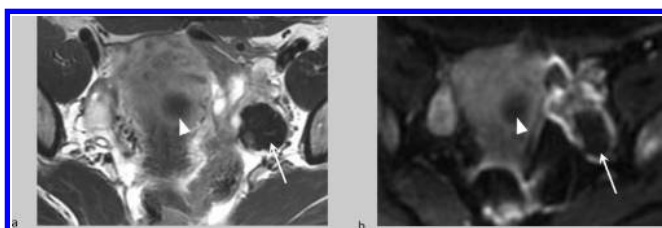
Figure 9. Examples of O-RADS MRI score 3, 4, five with enhancing solid tissue. O-RADS MRI score three lesion with ehancing solid tissue (white arrow) on selected axial T_2WI (a), post-contrast T_1WI (b), and corresponding low risk TIC curve (c). O-RADS MRI score 4 lesion with ehancing solid tissue (white arrow) on selected axial T_2WI (d), post-contrast T_1WI (e), and corresponding intermediate risk TIC curve (f). O-RADS MRI score 5 lesion with ehancing solid tissue (white arrow) on selected axial T_2WI (g), post-contrast T_1WI (h), and corresponding high risk TIC curve (I). T_1 Wi, T_1 weighted imaging; TIC, time–intensity curve.
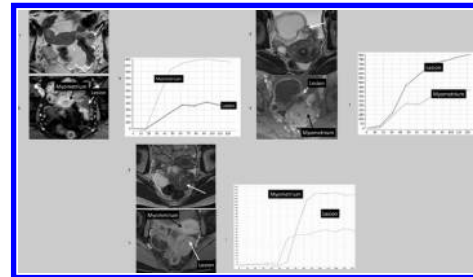
with solid tissue that enhances less than or equal to the myometrium is assigned an O-RADS MRI score 4, and lesion with solid tissue that enhances greater than the myometrium is assigned an O-RADS MRI score 5. It is important to underscore that if DCE MRI is not utilised, a lesion with enhancing solid tissue cannot be assigned an O-RADS MRI score 3 based on comparison between outer myometrium and solid tissue on a single phase.

Management of adnexal lesions: ongoing studies

MRI can help convey the suspicion of ovarian cancer in an adnexal lesion to the clinician with a high level of accuracy in prospective multicentre studies testing MRI scoring systems.[33,34,37–39] However, currently there is no prospective data on management of adnexal lesions beyond assignment of the percent risk of cancer based on assigning score. There are two prospective multicentre studies that when completed, will guide future recommendations for management of adnexal lesion imaged with MRI.

The ASCORDIA protocol (ClinicalTrials.gov Identifier: NCT02664597) aims to: limit surgery on benign adnexal lesions and to expedite assessment of patients with potential ovarian cancer and assure patients undergo the correct primary surgery. This is a currently ongoing prospective French multicentre randomised diagnostic study involving nine centres. In the control group, the adnexal mass will be managed according to the standard strategy and treatment plan routinely used by the multidisciplinary team. In the intervention group, patients will undergo pelvic MR imaging (1.5T or 3T). Prospectively, a senior radiologist will independently analyse any adnexal lesions and classify them using the O-RADS MRI risk score. The patient in the intervention group will be managed according to the O-RADS MRI risk score as follows:

- For lesions less than 4 cm:

When a lesion measuring less than 4 cm is Scored ≤3, follow-up imaging will be performed, if Scored = 4, diagnostic surgery will

be performed and if Scored 5, oncologic cytoreduction surgery will be performed.

- For lesions between 4 and 6 cm:

When a lesion measuring between 4 and 6 cm is scored ≤3, follow-up imaging will be performed, except for suspicion of dermoid cysts and endometriomas, if scored = 4, diagnostic surgery will be performed, and if scored 5, oncologic cytoreduction surgery will be performed.

- For lesions greater than 6 cm:

When a lesion measuring greater than 6 cm is scored ≤2, no surgery will be performed, except for dermoid cysts and endometriomas, ifscore 3 or 4, diagnostic surgery will be performed, and if score 5, oncologic cytoreduction surgery will be performed

The primary assessment criterion is the rate of inappropriate surgical intervention defined as oncologic surgery for benign lesions and incomplete staging for borderline or invasive cancer. This study began in December 2016 and has enrolled 377 patients.

A second multi-center trial in the UK (NIHR funded MROC(MR in Ovarian Cancer) study: ClinicalTrials.gov Identifier: ISRCTN51246892) is a prospective multicenter research study designed to evaluate the utility of MRI in clinical management in females with suspected or confirmed ovarian cancer compared to CT. The study includes 645 females in whom both MRI and CT will be obtained during the evaluation prior to treatment management. The CT reports will first be review by the clinical team and treatment plan will be recorded. Then the clinical team will be provided with the MRI report, and if the MRI changes the treatment plan, the adjusted plan will be recorded. Treatment plan options include: benign follow-up, fertility preserving surgery, cytoreductive surgery and chemotherapy. The females will then be followed to determine if the appropriate treatment was rendered. The definition of inappropriate surgery includes over extensive surgery for ovarian lesions that were benign or borderline at histology or attempted cytoreductive ovarian cancer surgery which could not be achieved due to extensive disease. The reference standard for stage and appropriate treatment choice will be final expert panel review with all results from surgery, histology, complications and clinical outcome at 9 months following the first treatment. Currently this study has enrolled all 645 subjects and is in the follow-up and statistical analysis phases.

CONCLUSION

Utilising MRI for the evaluation of adnexal lesions seen on ultrasound can increase the diagnostic accuracy of characterising a lesion as benign *vs* possibly malignant, particularly in the case of sonographically indeterminate adnexal lesions. This more promptly guides the management of the patient, avoiding surgery or over extensive surgery in benign lesions and borderline tumours, while expeditiously referring patients with possible malignancies to a gynecologic oncologist. Ongoing clinical trials will add information to help standardise the imaging evaluation of adnexal lesions and the role for different imaging modalities in staging of ovarian cancer.

DISCLOSURE

Andrea Rockall: Reports personal fees from Guerbet Laboratories, outside the submitted work. Imperial Cancer Research UK Centre and Imperial National Institute of Health Research Biomedical Research Centre. Isabelle Thomassin-Naggara: GE, Siemens, Hologic, Canon, Guerbet (remunerated lecture in breast imaging not related to the subject of the paper).

REFERENCES

1. Buys SS, Partridge E, Greene MH, Prorok PC, Reding D, Riley TL, et al. Ovarian cancer screening in the prostate, lung, colorectal and ovarian (PLCO) cancer screening trial: findings from the initial screen of a randomized trial. *Am J Obstet Gynecol* 2005; **193**: 1630–9. doi: https://doi.org/10.1016/j.ajog.2005.05.005

2. Greenlee RT, Kessel B, Williams CR, Riley TL, Ragard LR, Hartge P, et al. Prevalence, incidence, and natural history of simple ovarian cysts among women >55 years old in a large cancer screening trial. *Am J Obstet Gynecol* 2010; **202**: 373.e1–373.e9. doi: https://doi.org/10.1016/j.ajog.2009.11.029

3. Sharma A, Apostolidou S, Burnell M, Campbell S, Habib M, Gentry-Maharaj A, et al. Risk of epithelial ovarian cancer in asymptomatic women with ultrasound-detected ovarian masses: a prospective cohort study within the UK Collaborative trial of ovarian cancer screening (UKCTOCS. *Ultrasound Obstet Gynecol* 2012; **40**: 338–44. doi: https://doi.org/10.1002/uog.12270

4. Jacobs IJ, Menon U, Ryan A, Gentry-Maharaj A, Burnell M, Kalsi JK, et al. Ovarian cancer screening and mortality in the UK Collaborative trial of ovarian cancer screening (UKCTOCS): a randomised controlled trial. *Lancet* 2016; **387**: 945–56. doi: https://doi.org/10.1016/S0140-6736(15)01224-6

5. Atri M, Alabousi A, Reinhold C, Akin EA, Benson CB, Bhosale PR, et al. ACR appropriateness Criteria® clinically suspected adnexal mass, no acute symptoms. *J Am Coll Radiol* 2019; **16**: S77–93. doi: https://doi.org/10.1016/j.jacr.2019.02.011

6. Stein EB, Roseland ME, Shampain KL, Wasnik AP, Maturen KE. Contemporary guidelines for adnexal mass imaging: a 2020 update. *Abdom Radiol* 2020;20 Oct 2020. doi: https://doi.org/10.1007/s00261-020-02812-z

7. Andreotti RF, Timmerman D, Strachowski LM, Froyman W, Benacerraf BR, Bennett GL, et al. O-RADS us risk stratification and management system: a consensus guideline from the ACR Ovarian-Adnexal reporting and data system Committee. *Radiology* 2020; **294**: 168–85. doi: https://doi.org/10.1148/radiol.2019191150

8. Forstner R, Thomassin-Naggara I, Cunha TM, Kinkel K, Masselli G, Kubik-Huch R, et al. ESUR recommendations for MR imaging of the sonographically indeterminate adnexal mass: an update. *Eur*

Radiol 2017; **27**: 2248–57. doi: https://doi.org/10.1007/s00330-016-4600-3

9. Levine D, Brown DL, Andreotti RF, Benacerraf B, Benson CB, Brewster WR, et al. Management of asymptomatic ovarian and other adnexal cysts imaged at US Society of radiologists in ultrasound consensus conference statement. *Ultrasound Q* 2010; **26**: 121–31. doi: https://doi.org/10.1097/RUQ.0b013e3181f09099

10. ACRO-RADS-MR-risk-stratification-system-table. 2020. Available from: https://www.acr.org/Clinical-Resources/Reporting-and-Data-Systems/O-Rads#MRI.

11. Kaijser J, Vandecaveye V, Deroose CM, Rockall A, Thomassin-Naggara I, Bourne T, et al. Imaging techniques for the pre-surgical diagnosis of adnexal tumours. *Best Pract Res Clin Obstet Gynaecol* 2014; **28**: 683–95. doi: https://doi.org/10.1016/j.bpobgyn.2014.03.013

12. Thomassin-Naggara I, Aubert E, Rockall A, Jalaguier-Coudray A, Rouzier R, Daraï E, et al. Adnexal masses: development and preliminary validation of an Mr imaging scoring system. *Radiology* 2013; **267**: 432–43. doi: https://doi.org/10.1148/radiol.13121161

13. Timmerman D, Van Calster B, Testa A, Savelli L, Fischerova D, Froyman W, et al. Predicting the risk of malignancy in adnexal masses based on the simple rules from the International ovarian tumor analysis group. *Am J Obstet Gynecol* 2016; **214**: 424–37. doi: https://doi.org/10.1016/j.ajog.2016.01.007

14. Kurman RJ, Shih I-M. The dualistic model of ovarian carcinogenesis: revisited, revised, and expanded. *Am J Pathol* 2016; **186**: 733–47. doi: https://doi.org/10.1016/j.ajpath.2015.11.011

15. Shim S-H, Kim S-N, Jung P-S, Dong M, Kim JE, Lee SJ. Impact of surgical staging on prognosis in patients with borderline ovarian tumours: a meta-analysis. *Eur J Cancer* 2016; **54**: 84–95. doi: https://doi.org/10.1016/j.ejca.2015.11.005

16. Zhou J, Wu S-G, Wang J, Sun J-Y, He Z-Y, Jin X, et al. The effect of histological subtypes on outcomes of stage IV epithelial ovarian cancer. *Front Oncol* 2018; **8**: 577. doi: https://doi.org/10.3389/fonc.2018.00577

17. Trimbos JB. Surgical treatment of early-stage ovarian cancer. *Best Pract Res Clin Obstet Gynaecol* 2017; **41**: 60–70. doi: https://doi.org/10.1016/j.bpobgyn.2016.10.001

18. McEvoy SH, Nougaret S, Abu-Rustum NR, Vargas HA, Sadowski EA, Menias CO, et al. Fertility-Sparing for young patients with gynecologic cancer: how MRI can guide patient selection prior to conservative management. *Abdom Radiol* 2017; **42**:

2488–512. doi: https://doi.org/10.1007/s00261-017-1179-3

19. Morice P, Denschlag D, Rodolakis A, Reed N, Schneider A, Kesic V, et al. Recommendations of the fertility Task force of the European Society of gynecologic oncology about the conservative management of ovarian malignant tumors. *Int J Gynecol Cancer* 2011; **21**: 951–63. doi: https://doi.org/10.1097/IGC.0b013e31821bec6b

20. Rockall AG, Qureshi M, Papadopoulou I, Saso S, Butterfield N, Thomassin-Naggara I, et al. Role of imaging in fertility-sparing treatment of gynecologic malignancies. *Radiographics* 2016; **36**: 2214–33. doi: https://doi.org/10.1148/rg.2016150254

21. Stein EB, Hansen JM, Maturen KE. Fertility-Sparing approaches in gynecologic oncology: role of imaging in treatment planning. *Radiol Clin North Am* 2020; **58**: 401–12. doi: https://doi.org/10.1016/j.rcl.2019.10.006

22. Modesitt SC, Pavlik EJ, Ueland FR, DePriest PD, Kryscio RJ, van Nagell JR. Risk of malignancy in unilocular ovarian cystic tumors less than 10 centimeters in diameter. *Obstet Gynecol* 2003; **102**: 594–9. doi: https://doi.org/10.1016/s0029-7844(03)00670-7

23. Timmerman D, Ameye L, Fischerova D, Epstein E, Melis GB, Guerriero S, et al. Simple ultrasound rules to distinguish between benign and malignant adnexal masses before surgery: prospective validation by iota group. *BMJ* 2010; **341**: c6839. doi: https://doi.org/10.1136/bmj.c6839

24. Patel-Lippmann KK, Sadowski EA, Robbins JB, Paroder V, Barroilhet L, Maddox E, et al. Comparison of international ovarian tumor analysis simple rules to Society of radiologists in ultrasound guidelines for detection of malignancy in adnexal cysts. *AJR Am J Roentgenol* 2020; **214**: 694–700. doi: https://doi.org/10.2214/AJR.18.20630

25. Sadowski EA, Paroder V, Patel-Lippmann K, Robbins JB, Barroilhet L, Maddox E, et al. Indeterminate adnexal cysts at US: prevalence and characteristics of ovarian cancer. *Radiology* 2018; **287**: 1041–9. doi: https://doi.org/10.1148/radiol.2018172271

26. Adusumilli S, Hussain HK, Caoili EM, Weadock WJ, Murray JP, Johnson TD, et al. Mri of sonographically indeterminate adnexal masses. *AJR Am J Roentgenol* 2006; **187**: 732–40. doi: https://doi.org/10.2214/AJR.05.0905

27. Anthoulakis C, Nikoloudis N. Pelvic MRI as the "gold standard" in the subsequent evaluation of ultrasound-indeterminate adnexal lesions: a systematic review. *Gynecol Oncol* 2014; **132**: 661–8. doi: https://doi.org/10.1016/j.ygyno.2013.10.022

28. Hricak H, Chen M, Coakley FV, Kinkel K, Yu KK, Sica G, et al. Complex adnexal masses: detection and characterization with MR imaging--multivariate analysis. *Radiology* 2000; **214**: 39–46. doi: https://doi.org/10.1148/radiology.214.1.r00ja3939

29. Kaijser J, Sayasneh A, Van Hoorde K, Ghaem-Maghami S, Bourne T, Timmerman D, et al. Presurgical diagnosis of adnexal tumours using mathematical models and scoring systems: a systematic review and meta-analysis. *Hum Reprod Update* 2014; **20**: 449–62. doi: https://doi.org/10.1093/humupd/dmt059

30. Kinkel K, Lu Y, Mehdizade A, Pelte M-F, Hricak H. Indeterminate ovarian mass at US: incremental value of second imaging test for characterization--meta-analysis and Bayesian analysis. *Radiology* 2005; **236**: 85–94. doi: https://doi.org/10.1148/radiol.2361041618

31. Maturen KE, Blaty AD, Wasnik AP, Patel-Lippmann K, Robbins JB, Barroilhet L, et al. Risk stratification of adnexal cysts and cystic masses: clinical performance of Society of radiologists in ultrasound guidelines. *Radiology* 2017; **285**: 650–9. doi: https://doi.org/10.1148/radiol.2017161625

32. Nunes N, Ambler G, Foo X, Naftalin J, Widschwendter M, Jurkovic D. Use of iota simple rules for diagnosis of ovarian cancer: meta-analysis. *Ultrasound Obstet Gynecol* 2014; **44**: 503–14. doi: https://doi.org/10.1002/uog.13437

33. Pereira PN, Sarian LO, Yoshida A, Araújo KG, Silva ACB, de Oliveira Barros RH, et al. Improving the performance of iota simple rules: sonographic assessment of adnexal masses with resource-effective use of a magnetic resonance scoring (ADNEX MR scoring system. *Abdominal Radiology* 2020; **45**: 3218–29. doi: https://doi.org/10.1007/s00261-019-02207-9

34. Thomassin-Naggara I, Poncelet E, Jalaguier-Coudray A, Guerra A, Fournier LS, Stojanovic S, et al. Ovarian-Adnexal reporting data system magnetic resonance imaging (O-RADS MRI) score for risk stratification of Sonographically indeterminate adnexal masses. *JAMA Netw Open* 2020; **3**: e1919896. doi: https://doi.org/10.1001/jamanetworkopen.2019.19896

35. Sadowski EA, Robbins JB, Rockall AG, Thomassin-Naggara I. A systematic approach to adnexal masses discovered on ultrasound: the ADNEX Mr scoring system. *Abdom Radiol* 2018; **43**: 679–95. doi: https://doi.org/10.1007/s00261-017-1272-7

36. Bernardin L, Dilks P, Liyanage S, Miquel ME, Sahdev A, Rockall A. Effectiveness of semi-quantitative multiphase dynamic contrast-enhanced MRI as a predictor of

malignancy in complex adnexal masses: radiological and pathological correlation. *Eur Radiol* 2012; **22**: 880–90. doi: https://doi.org/10.1007/s00330-011-2331-z

37. Pereira PN, Sarian LO, Yoshida A, Araújo KG, Barros RHO, Baião AC, et al. Accuracy of the ADNEX Mr scoring system based on a simplified MRI protocol for the assessment of adnexal masses. *Diagn Interv Radiol* 2018; **24**: 63–71. doi: https://doi.org/10.5152/dir.2018.17378

38. Ruiz M, Labauge P, Louboutin A, Limot O, Fauconnier A, Huchon C. External validation of the Mr imaging scoring system for the management of adnexal

masses. *Eur J Obstet Gynecol Reprod Biol* 2016; **205**: 115–9. doi: https://doi.org/10.1016/j.ejogrb.2016.07.493

39. Sasaguri K, Yamaguchi K, Nakazono T, Mizuguchi M, Aishima S, Yokoyama M, et al. External validation of ADNEX MR scoring system: a single-centre retrospective study. *Clin Radiol* 2019; **74**: 131–9. doi: https://doi.org/10.1016/j.crad.2018.10.014

40. Zhang X, Mao Y, Zheng R, Zheng Z, Huang Z, Huang D, et al. The contribution of qualitative CEUS to the determination of malignancy in adnexal masses, indeterminate on conventional US - a

multicenter study. *PLoS One* 2014; **9**: e93843. doi: https://doi.org/10.1371/journal.pone.0093843

41. Togashi K, Nishimura K, Kimura I, Tsuda Y, Yamashita K, Shibata T, et al. Endometrial cysts: diagnosis with MR imaging. *Radiology* 1991; **180**: 73–8. doi: https://doi.org/10.1148/radiology.180.1.2052726

42. Zhou H, Ma X, Sheng M, Lai C, Fu J. Evolution of intramural duodenal hematomas on magnetic resonance imaging. *Pediatr Radiol* 2018; **48**: 1593–9. doi: https://doi.org/10.1007/s00247-018-4178-9

FULL PAPER

Dynamic contrast-enhanced MRI can quantitatively identify malignant transformation of sinonasal inverted papilloma

[1]ZHENG LI, MD, [2]MU XIAN, MD, [1]JIAN GUO, MD, [2]CHENG SHUO WANG, MD, [2]LUO ZHANG, MD and [1]JUNFANG XIAN, MD, PhD

[1]Department of Radiology, Beijing Tongren Hospital, Capital Medical University, Beijing, China
[2]Department of Otolaryngology Head and Neck Surgery, Beijing Tongren Hospital, Capital Medical University, Beijing, China

Address correspondence to:
Luo Zhang
E-mail: *dr.luozhang@139.com*
Dr Junfang Xian
E-mail: *cjr.xianjunfang@vip.163.com*

Objective: To investigate the diagnostic performance of quantitative and semi-quantitative parameters derived from dynamic contrast-enhanced MRI (DCE-MRI) in differentiating sinonasal inverted papilloma (SIP) from SIP with coexisting malignant transformation into squamous cell carcinoma (MT-SIP).

Methods: This retrospective study included 122 patients with 88 SIP and 34 MT-SIP. Quantitative and semi-quantitative parameters derived from DCE-MRI were compared between SIP and MT-SIP. The multivariate logistic regression analysis was performed to identify independent indicators and construct regression model for distinguishing MT-SIP and SIP. Diagnostic performance of independent indicators and regression model were evaluated using receiver operating coefficient (ROC) analysis and compared using DeLong test.

Results: There were significant differences in maximum slope of increase, contrast-enhancement ratio, bolus arrival time, volume of extravascular extracellular space (V_e), and rate constant (K_{ep}) between SIP and MT-SIP (p < 0.05). There were no significant differences in initial area under the gadolinium curve (p = 0.174) and volume transfer constant (p = 0.105) between two groups. Multivariate analysis results showed that V_e and K_{ep} were identified as the independent indicators for differentiating MT-SIP from SIP (p < 0.001). Areas under the ROC curves (AUCs) for predicting MT-SIP were 0.779 for V_e and 0.766 for K_{ep}. The AUC of the combination of V_e and K_{ep} was 0.831, yielding 83% specificity and 76.5% sensitivity.

Conclusion: DCE-MRI can quantitatively differentiate between MT-SIP and SIP. The combination of V_e and K_{ep} yielded an optimal performance for discriminating SIP from its malignant mimics.

Advances in knowledge: DCE-MRI with quantitative and semi-quantitative parameters can provide valuable evidences for quantitatively identifying MT-SIP.

Sinonasal inverted papilloma (SIP) is a benign sinonasal neoplasm with an incidence of 0.74–1.5 per 100.000 per year.[1] However, squamous cell carcinoma can be associated with SIP in approximately 7–11% of cases either synchronously or metachronously.[2–4] SIP with coexisting malignant transformation into squamous cell carcinoma (MT-SIP) has different prognoses and treatment. Minimally invasive endoscopic surgery is the standard for treatment of SIP, while aggressive surgical resection combined with post-operative adjuvant radiotherapy or chemoradiotherapy is needed.[5–7] Therefore, it is necessary to identify MT-SIP before surgery.

Accurate diagnosis of MT-SIP remains clinically challenging pre-operatively. Biopsy is the current reference standard for quantifying the degree of cellular atypia and demonstrating MT-SIP.[1] However, biopsy is invasive with the risk of hemorrhagic complications. Moreover, misdiagnosis is frequently encountered due to sampling errors.[8,9] MR imaging including diffusion-weighted imaging (DWI) and dynamic contrast-enhanced (DCE)-MR imaging plays a vital role in distinguishing SIP from MT-SIP with specificity ranging from 78 to 93% and sensitivity ranging from 62 to 100%.[3,10] Nonetheless, the repeatability and reliability concerns have been raised in these studies because of the variation of evaluating

morphological features and the type of time–intensity curve on MRI among different investigators.

Several studies have involved semi-quantitative and quantitative parameters derived from DCE-MRI to characterize the vascular properties of sinonasal tumors, yielding a high accuracy in discriminating benign from malignant sinonasal tumors.[11–13] Moreover, the quantitative nature of these imaging parameters could greatly increase reliability in the clinical setting. In addition, the pseudocolor maps of these parameters can provide visual–anatomical information on tumor boundaries, hence facilitating region of interest (ROI) selection.[14] Therefore, we hypothesized that the quantitative and semi-quantitative parameters derived from DCE-MRI can be a useful tool for the detection of MT-SIP. This study aims to investigate the diagnostic performance of quantitative and semi-quantitative parameters derived from DCE-MRI in differentiation between SIP and MT-SIP, which would provide more accurate information for identifying MT-SIP.

METHODS AND MATERIALS
Our institutional review board approved this retrospective case–control study. Written informed consent was waived because of the retrospective nature of the study.

SIP and MT-SIP patients
From January 2016 to December 2020, 141 consecutive patients with SIP and MT-SIP proven by pathology were retrospectively reviewed. The inclusion criteria were as follows: (1) MR scanning was performed before the biopsy and treatment. (2) DCE-MRI sequences were available. Exclusion criteria included: (1) patients with poor quality of images (n = 11) and (2) patients with the tumor less than 10 mm in short-axis diameters (n = 8).[15] Ultimately, a total of 122 patients, including 88 patients with SIP [65 male and 23 female; age range 30–80 years; median age 54 years; median tumor volume 35.5 ($\times 10^3$/mm^3)] and 34 patients with MT-SIP [31 male and three female; age range 31–79 years; median age 62 years; median tumor volume 32.4 ($\times 10^3$/mm^3)], were enrolled in this study. The specific location of tumors detected by surgery for each patient.

MRI acquisition
Sinonasal MR imaging was performed at 3.0 T MR system (68 patients with Signa HDxt and 54 patient with Discovery MR750, GE Healthcare, Milwaukee, WI) with an 8-channel head coil. The acquisition parameters of axial T_1 weighted fast spin echo imaging were repetition time (TR)/echo time (TE) = 560–590 ms/7–10 ms, slice thickness = 3.5–4 mm, slice gap = 0.3–0.4 mm, number of excitations (NEX) = 2; acquisition matrix = 320 × 256 or 288 × 224. Parameters of axial T_2 weighted fast spin echo imaging were TR/TE = 3975–4720 ms/85–89 ms, slice thickness = 3.5–4 mm, slice gap = 0.3–0.4 mm, NEX = 2; acquisition matrix = 320 × 256 or 288 × 224.

DCE-MR images were acquired via a fast-spoiled gradient recalled (FSPGR) T_1WI. Detailed imaging parameters were as follows: TR/TE = 3.9 ms/1.6 ms, slice thickness = 4–5 mm, no slice gap, flip angle = 11°, NEX = 2, acquisition matrix = 256×160. After the

acquisition of one baseline phase of images, gadopentetate dimeglumine (Magnevist, Bayer Schering, Berlin, Germany) (a dose of 0.1 mmol/kg) was intravenously bolus injected via a power injector at a flow rate of 2 ml s^{-1} followed by a 20 ml saline flush at the same rate. Then, a total of 31 or 36 phases of images were sequentially acquired with a temporal resolution of 8 sec. After the DCE-MRI sequence, a post-contrast axial T1WI with fat saturation was obtained with parameters same as unenhanced T1WI, followed by post-contrast coronal and sagittal T_1-weighted images (TR/TE = 450–720 ms/10–12 ms; slice thickness = 3–4 mm, slice gap = 5.5 mm; NEX = 2; acquisition matrix = 320 × 256).

DCE-MRI derived parameters
DCE-MRI data were postprocessed using Advantage Workstation (v. 4.6, GE Healthcare, Milwaukee, WI). Signal intensity changes in internal carotid were automatically measured for arterial input function (AIF). Then, pixel-based maps for DCE parameters were calculated using GenIQ software (GE Healthcare, Milwaukee, WI).

All quantitative analysis on DCE-MR images were based on two-compartment modified Tofts model. The calculated quantitative parameters were the transfer constant between intra- and extravascular extracellular spaces (K^{trans}; min^{-1}), the volume of the extravascular extracellular space (V$_e$), and the transfer constant from the extravascular extracellular space to plasma (K$_{ep}$; min^{-1}, K$_{ep}$ = K^{trans}/ $_{Ve}$).

The average signal intensity within the pixel was plotted against time, and TICs were constructed. The semi-quantitative parameters were calculated on a pixel-by-pixel basis from the TICs, including maximum slope of the steepest part of the concentration curve (MaxSlope; mmol/s); the contrast-enhancement ratio (CER) = (peak signal-baseline signal)/(baseline signal); the bolus arrival time (BAT; s)=the time from the start of contrast injection to tracer bolus arrival at a lesion; and the initial area under the signal intensity–time curve (IAUGC) = (area under the tissue concentration curve from BAT to 60 s from the start of contrast injection)/(area under the AIF concentration curve from BAT to 60 s from the start of contrast injection).

Imaging analysis
Two readers (Reader 1 and Reader 2 with 8 and 20 years of experience in head and neck radiology, respectively) were blinded to the pathological results and delineated two-dimensional ROIs manually. The ROIs covered the largest single-slice at the level of maximum diameter of tumor based on DCE-MR images, avoiding the obvious necrotic, cystic, and hemorrhagic areas inside tumor and surrounding blood vessels (Figure 1). Edges of lesions were also excluded from ROI to minimize the effect of partial volume averaging. The measurements of two readers were used to assess the interobserver consistency. For intraobserver consistency, Reader 1 repeated the process of ROI placement with a month interval, and the average results of Reader 1 were used for statistical analysis.

Statistical analyses
Inter- and intraobserver consistency of each quantitative parameters based on ROIs were assessed by using the intraclass

Figure 1. Illustrations of ROI placement. A 2D-ROI covered a slice with the largest diameter of tumor based on DCE sequence, avoiding the obvious necrotic, cystic, and hemorrhagic areas inside tumor and surrounding blood vessels. 2D, two-dimensional; DCE, dynamic contrast-enhanced; ROI, region of interest.
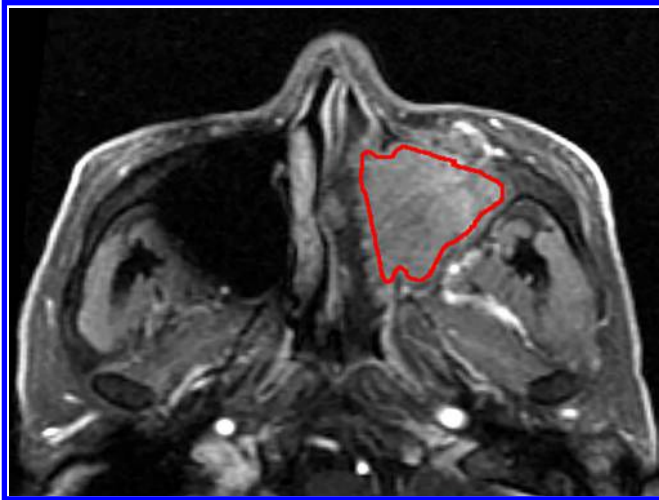
correlation coefficient (ICC). The consistency was defined as follows: <0.40, fair; 0.41–0.60, moderate; 0.61–0.80, good; and >0.80, excellent.

The Kolmogorov–Smirnov test was used to test the normality for each continuous variable, after which the variable was expressed as median (interquartile range) when data non-normally distributed. Mann–Whitney U test (non-normally distributed) was used to compare parametric values between SIP and MT-SIP groups. The significantly different parameters were involved in a forward stepwise multivariable logistic regression analysis for determining independent diagnostic parameters and the best logistic regression model. Receiver operating characteristic (ROC) curve analyses were performed to evaluate the diagnostic performance of independent diagnostic parameters and regression model in differentiating MT-SIP from SIP. The optimal threshold of each independent diagnostic parameter was determined by the maximum *Youden index* (*Youden index*

= sensitivity + specificity −1). Differences of area under the ROC curve (AUC) were compared using the DeLong's test.

All statistical analyses were performed with statistical software (SPSS v. 19.0, SPSS, Chicago, IL; and Medcalc v. 9.0, MedCalc Software, Mariakerke, Belgium). The $p < 0.05$ values were considered significant.

RESULTS

Tumor location
SIPs were found in the maxillary sinus in 31 cases (35.2%), in the nasal cavity in 28 cases (31.8%), in the ethmoid sinus in 15 cases (17.1%), in the frontal sinus in 9 cases (10.2%), and in the sphenoid sinus in 5 cases (5.7%). MT-SIPs were identified in the maxillary sinus in 16 cases (47.1%), in the nasal cavity in 9 cases (26.5%), in the ethmoid sinus in 6 cases (17.6%), and in the sphenoid sinus in 3 cases (8.8%).

Comparison of quantitative and semi-quantitative parameters derived from DCE-MRI between SIP and MT-SIP
Maxslope, CER, BAT and V_e were significantly higher in SIP than those in MT-SIP ($p < 0.05$). K_{ep} was significantly lower in SIP than that in MT-SIP ($p < 0.05$) (Table 1). There was no significant difference in IAUGC and K^{trans} ($p > 0.05$) between two groups (Table 1).

Inter- and intraobserver agreement
The inter- and intraobserver agreement for each parameter derived from DCE-MRI were indicated in Table 1. The inter- and intraobserver agreement were both excellent (ICCs = 0.816–0.982) for CER, BAT, IAUGC, K^{trans}, V_e, and K_{ep}. Good inter- and intraobserver agreement were shown in Maxslope (ICCs = 0.614, 0.762).

Multivariate logistic regression analysis
Multivariate logistic regression analysis demonstrated that V_e [Odds ratio (OR)=0.004; 95% confidence interval (95% CI)=0.001–0.065; $p < 0.001$] and K_{ep} (OR = 3.852; 95%CI = 1.609–9.219; $p = 0.002$) were independent indicators for

Table 1. Comparisons of DCE-MRI parameters between SIP and MT-SIP and ICCs of intra- and interobserver consistency

Parameters	SIP ($n = 88$)	MT-SIP ($n = 34$)	p-value	Interobserver consistency		Intraobserver consistency	
				ICC	95% CI	ICC	95% CI
Maxslope(mmol/s)	0.03 (0.02,0.05)	0.02 (0.02,0.04)	0.003	0.614	0.490–0.713	0.762	0.660–0.834
CER	1.76 (1.59,2.11)	1.50 (1.22,1.79)	<0.001	0.816	0.756–0.868	0.903	0.864–0.931
IAUGC	0.30 (0.21,0.43)	0.31 (0.25,0.63)	0.174	0.863	0.810–0.902	0.938	0.913–0.956
BAT(s)	33.09 (23.25,42.43)	24.08 (19.44,33.64)	0.022	0.975	0.965–0.983	0.981	0.973–0.987
K^{trans}(min^{-1})	0.37 (0.24,0.54)	0.44 (0.29,0.66)	0.105	0.954	0.935–0.968	0.939	0.914–0.957
V_e	0.66 (0.56,0.84)	0.49 (0.36,0.58)	<0.001	0.843	0.770–0.881	0.850	0.792–0.893
K_{ep}(min^{-1})	0.62 (0.45,0.88)	1.05 (1.33,0.79)	<0.001	0.963	0.947–0.974	0.982	0.975–0.988

BAT, the bolus arrival time; CER, the contrast-enhancement ratio; CI, confidence interval; IAUGC, the initial area under the signal intensity–time curve; ICC, intraclass correlation coefficient; MT-SIP, malignant transform of sinonasal inverted papillomas; ROI, region of interest; SIP, sinonasal inverted papillomas.

Figure 2. A 43-year-old male with malignant inverted papilloma transformation in the right maxillary sinus. Pseudocolor map of V_e(a) shows a mean value of V_e of malignant inverted papilloma transformation (red arrow) is 0.48, lower than the cutoff value of 0.58. Pseudocolor map of K_{ep} (b) shows a mean value of K_{ep} of malignant inverted papilloma transformation (red arrow) is 1.03(min^{-1}), higher than the cut-off value of 0.75 (min^{-1}).
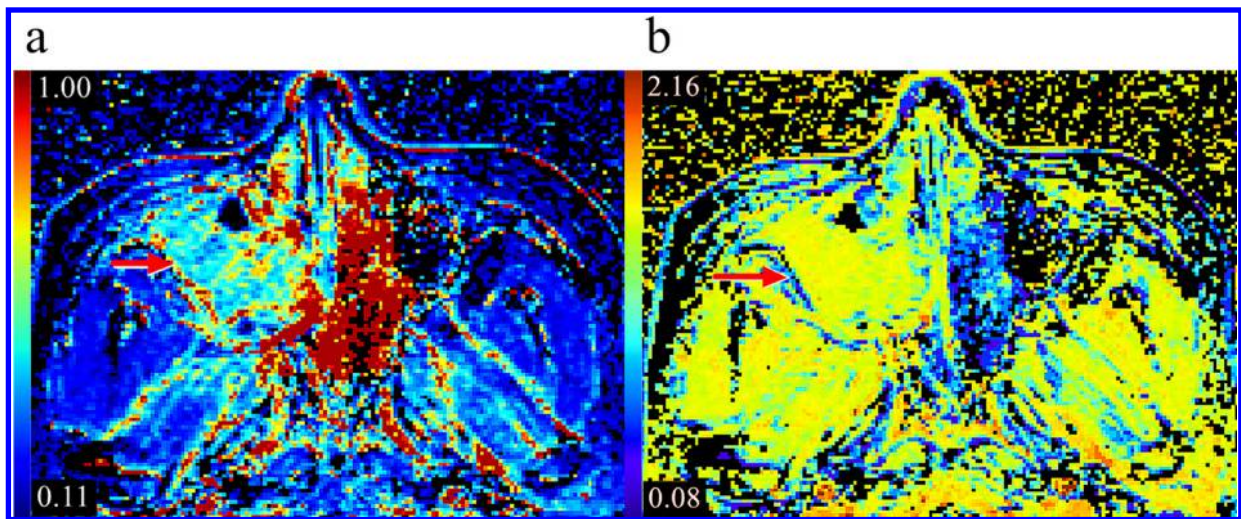
differentiating MT-SIP from SIP (Figures 2 and 3, Supplementary Material 1).

ROC curve analysis

The AUC, sensitivity, specificity, positive-predicted value, and negative-predicted value of each independently diagnostic parameter and regression model discriminating SIP and MT-SIP were showed in Table 2 and Figure 4. Using a V_e value of 0.582 or a Kep value of 0.747 as a threshold value for diagnosis, the sensitivity and specificity were 79.4 and 68.2%, respectively. The AUC for diagnosis of V_e and K_{ep} were 0.779 (95%CI = 0.695–0.849) and 0.766 (95%CI = 0.681–0.838), respectively.

When combined V_e and K_{ep}, the specificity increased to 83% from 68.2%, while the sensitivity decreased to 76.5% from 79.4%. The combination of V_e and K_{ep} showed the largest AUC of 0.831 (95%CI = 0.752–0.892) in discrimination of SIP and MT-SIP. However, there was no significant difference of AUC among them (V_e *vs* K_{ep}, p = 0.846; combined model *vs* V_e, p = 0.0654; combined model *vs* K_{ep}, p = 0.1274). The Hosmer-Lemeshow goodness-of-fit test result was not significantly different for the combined model.

Figure 3. A 60-year-old male with inverted papilloma in the left maxillary sinus. Pseudocolor map of V_e(a) shows a mean value of V_e of inverted papilloma (red arrow) is 0.66, higher than the cut-off value of 0.58. Pseudocolor map of K_{ep} (b) shows a mean value of K_{ep} of inverted papilloma (red arrow) is 0.57 (min^{-1}), lower than the cut-off value of 0.75 (min^{-1}).
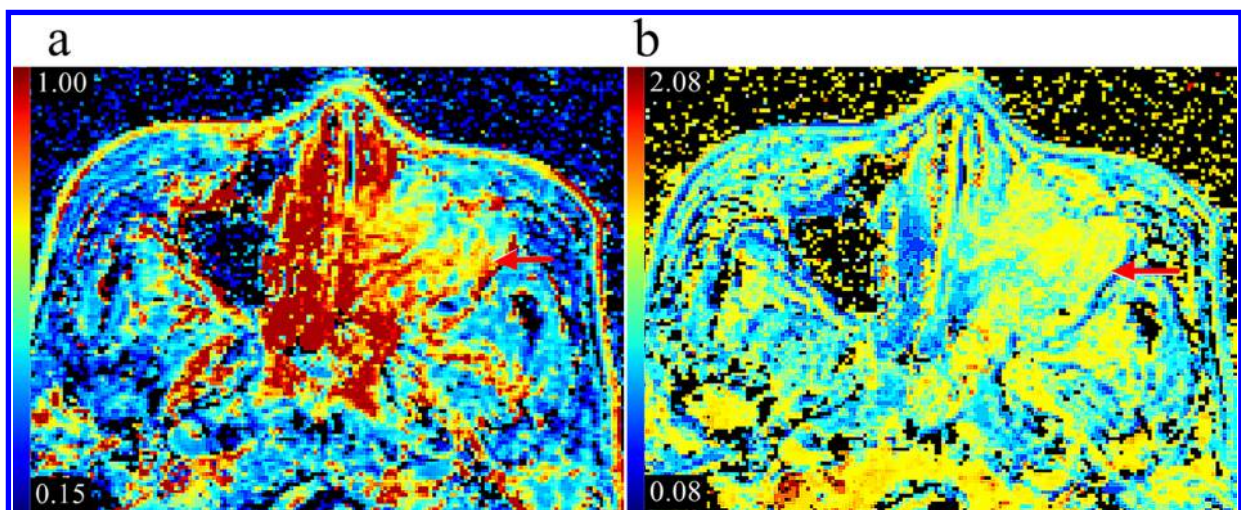
Table 2. ROC analysis for V_e, K_{ep}, and their combination model in distinguishing between SIP and MT-SIP

Parameters	Cut-off	SEN (%)	SPE (%)	PPV (%)	NPV (%)	AUC (95% CI)
V_e	0.582	79.4	68.2	49.1	89.6	0.779 (0.695–0.849)
K_{ep} (min^{-1})	0.747	79.4	68.2	49.1	89.6	0.766 (0.681–0.838)
$V_e + K_{ep}$		76.5	83.0	63.4	90.1	0.831 (0.752–0.892)

AUC, area under the curve; IAUGC, the initial area under the signal intensity–time curve; NPV, negative predictive value; PPV, positive predictive value; ROC, receiver operating characteristics; ROI, region of interest; SEN, sensitivity; SPE, specificity.

DISCUSSION

Given its aggressive nature and poor prognosis, MT-SIPs require radical treatment strategies. Hence, it is of great importance to discriminate MT-SIP from SIP before making a treatment decision. This retrospective study compared a variety of parameters derived from DCE-MRI and suggested that Maxslope, CER, BAT, V_e and K_{ep} were significantly different between SIP and MT-SIP, with excellent to good repeatability. Moreover, V_e and K_{ep} were independent indicators for discriminating MT-SIP from SIP, and combination of V_e and K_{ep} yielded an optimal diagnostic performance with an AUC of 0.831. Hence, DCE-MRI can be a quantitative technique for detecting MT-SIP non-invasively.

DCE-MRI was suggested to reflect microvascular environment in sinonasal cancers using pharmacokinetic models with quantitative parameters.[11,16] However, there was a paucity of quantitative parameters derived from DCE-MRI that focused on differentiation between SIP and MT-SIP. K_{ep} is a quantitative parameter that refers to the contrast agent transfer from the tissue space to the blood and has been shown to be positively associated with vascular permeability of tumor.[17] Our study showed that K_{ep} values were significantly larger in MT-SIP than that in SIP, suggesting that MT-SIP has incomplete microvascular circulation and high permeability. However, K^{trans}, as another quantitative parameter relates to vascular permeability, showed no significant difference between MT-SIP and SIP. One possible

reason for this phenomenon may be due to the fact that K^{trans} can be affected by microvascular density of tumor beside the vascular permeability.[18] For example, a high microvascular density in the peripheral portion of SIP would definitely elevate its mean value of K^{trans}, and therefore the K^{trans} of SIP may be comparable with that of MT-SIP, which mainly attributed to high permeability.[18]

While noting the limitations posed by lacking reproducibility, previous studies concluded that DWI with apparent diffusion coefficient value can reflect cellularity of tumors and can be a highly sensitive tool for differentiation between SIP and MT-SIP.[3] However, it has not developed into a standalone diagnostic tool due to its relatively low specificity. Moreover, V_e is a quantitative parameter derived from DCE-MRI, which can simultaneously quantify cellularity and vascular properties of tumor.[19] Depending mainly on the cell density and the composition of the extravascular extracellular matrix, V_e value is correlated inversely with the tumor cellularity and positively with the volume of extravascular extracellular space.[20] Our study showed that V_e was significantly lower in MT-SIP than that in SIP. This result was very similar to that of the previous study[3] and suggested that MT-SIP has a higher cellularity and a lower extracellular space compared to SIP.

Furthermore, this study demonstrated that K_{ep} and V_e can be independently used to distinguish SIP from MT-SIP. The change in vascular permeability and cellularity seemed to be the major factors in malignant transformation of SIP. This result contained an important message that monitoring malignant transformation of SIP might be objectively estimated by quantitative parameters derived from DCE-MRI. In addition, ROC analysis suggested a powerful prediction of K_{ep} and V_e with an AUC of 0.766 and 0.779, respectively. However, a combination of these two parameters was needed for improving the specificity in predicting MT-SIP.

Combination of V_e and K_{ep} showed a satisfactory performance in predicting MT-SIP with an AUC of 0.831. Further, the combined model increased the specificity of DCE-MRI, although the sensitivity slightly decreased. These results indicated that comprehensive evaluation of quantitative parameters may further refine our ability to differentiate benign from malignant sinonasal tumors on DCE-MRI and may reduce the need for biopsy.

Semi-quantitative parameters derived from DCE-MRI may help for reflecting divergent hemodynamic patterns of tumors.[21] Further, the semi-quantitative data are unlikely to be influenced

Figure 4. ROC curves and AUC (in brackets) for V_e, K_{ep}, and their combination model.AUC, area under the curve; ROC, receiver operating coefficient; ROI, region of interest.
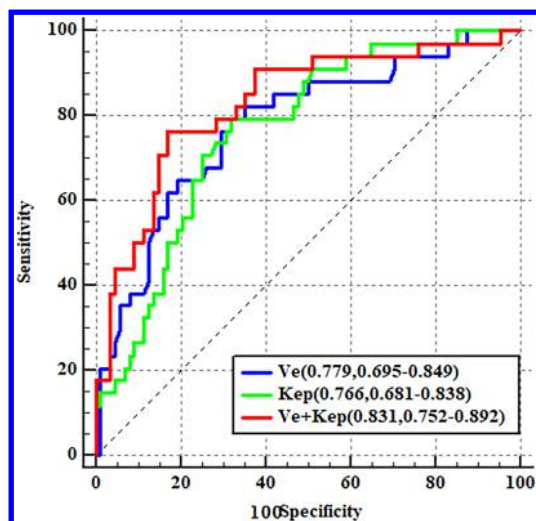
by variation of scanning protocols and is easier in post-processing compared with the quantitative data.[22] In our study, Maxslope and CER in SIP significantly were higher than those in MT-SIP, suggesting that degree of enhancement in SIP was higher than MT-SIP. While, shorter BAT for MT-SIP might associate with shunt formation and low-resistance and high-flow pathways within tumor. However, none of semi-quantitative parameters were independently associated with MT-SIP based on multivariate logistic regression analysis. This finding, to some degree, suggested that the diagnostic performance of semi-quantitative parameters was inferior to that of quantitative parameters in detecting MT-SIP.

LIMITATIONS

Our study had several limitations. First, the study included a relatively small population from a single institution. Multicentric studies with larger patient populations were required to further validate our results. Second, we did not report on the conventional MRI features for the differentiation of tumors, the assessment of which was not within the scope of our study. Finally, obtaining the completed surgical specimen for histopathological analysis is difficult in clinical practice, thus a head-to-head evaluation of images and histopathological findings of areas covered by ROI had not been performed.

CONCLUSIONS

In conclusion, DCE-MRI can quantitatively differentiate between MT-SIP and SIP. V_e and K_{ep} were independent indicators for discriminating MT-SIP from SIP with high repeatability. The combination of V_e and K_{ep} may obtain an optimal performance for discriminating SIP from its malignant mimics.

ACKNOWLEDGMENTS

REFERENCES

1. Lisan Q, Laccourreye O, Bonfils P. Sinonasal inverted papilloma: from diagnosis to treatment. *Eur Ann Otorhinolaryngol Head Neck Dis* 2016; **133**: S1879-7296(16)30054-0: 337–41: . https://doi.org/10.1016/j.anorl.2016.03.006

2. Lee JJ, Roland LT, Licata JJ, Orlowski HLP, Jiramongkolchai P, et al. Morphologic, intraoperative, and histologic risk factors for sinonasal inverted papilloma recurrence. *Laryngoscope* 2020; **130**: 590–96. https://doi.org/10.1002/lary.28078

3. Yan CH, Tong CCL, Penta M, Patel VS, Palmer JN, et al. Imaging predictors for malignant transformation of inverted papilloma. *Laryngoscope* 2019; **129**: 777–82. https://doi.org/10.1002/lary.27582

4. Udager AM, McHugh JB, Goudsmit CM, Weigelin HC, Lim MS, et al. Human papillomavirus (HPV) and somatic EGFR mutations are essential, mutually exclusive oncogenic mechanisms for inverted sinonasal papillomas and associated sinonasal squamous cell carcinomas. *Ann Oncol* 2018; **29**: S0923-7534(19)35054-9: 466–71: . https://doi.org/10.1093/annonc/mdx736

5. Re M, Gioacchini FM, Bajraktari A, Tomasetti M, Kaleci S, et al. Malignant transformation of sinonasal inverted papilloma and related genetic alterations: a systematic review. *Eur Arch Otorhinolaryngol* 2017; **274**: 2991–3000. https://doi.org/10.1007/s00405-017-4571-2

6. Contrera KJ, Woody NM, Rahman M, Sindwani R, Burkey BB, et al. Clinical management of emerging sinonasal malignancies. *Head Neck* 2020; **42**: 2202–12. https://doi.org/10.1002/hed.26150

7. Lee JJ, Peterson AM, Embry TW, Wamkpah NS, Kallogjeri D, et al. Survival outcomes of de novo vs inverted papilloma-associated sinonasal squamous cell carcinoma: a systematic review and meta-analysis. *JAMA Otolaryngol Head Neck Surg* 2021; **147**: 350–59. https://doi.org/10.1001/jamaoto.2020.5261

8. Marri UK, Das P, Kalaivani M, Srivastava DN, et al. Noninvasive staging of liver fibrosis using 5-minute delayed dual-energy CT: comparison with US elastography and correlation with histologic findings. *Radiology* 2021; **298**: 600–608. https://doi.org/10.1148/radiol.2021202232

9. Schreiber A, Rampinelli V, Ferrari M, Mattavelli D, Farina D, et al. Diagnostic reliability of pretreatment biopsy in malignant nasoethmoidal tumors: A retrospective study of 77 cases. *Laryngoscope* 2018; **128**: 1772–77. https://doi.org/10.1002/lary.27077

10. Zhang L, Fang G, Yu W, Yang B, Wang C, et al. Prediction of malignant sinonasal inverted papilloma transformation by preoperative computed tomography and magnetic resonance imaging. *Rhinology* 2020; **58**: 248–56. https://doi.org/10.4193/Rhin19.240

11. Xian J, Du H, Wang X, Yan F, Zhang Z, et al. Feasibility and value of quantitative dynamic contrast enhancement MR imaging in the evaluation of sinonasal tumors. *Chin Med J (Engl)* 2014; **127**: 2259–64.

12. Wang X, Zhang Z, Chen X, Li J, Xian J, et al. Value of magnetic resonance imaging including dynamic contrast-enhanced magnetic resonance imaging in differentiation between inverted papilloma and malignant tumors in the nasal cavity. *Chin Med J (Engl)* 2014; **127**: 1696–1701.

13. Wang X-Y, Yan F, Hao H, Wu J-X, Chen Q-H, et al. Improved performance in differentiating benign from malignant sinonasal tumors using diffusion-weighted combined with dynamic contrast-enhanced magnetic resonance imaging. *Chin Med J (Engl)* 2015; **128**: 586–92. https://doi.org/10.4103/0366-6999.151649

14. Cheng J, Shao S, Chen W, Zheng N, et al. Application of diffusion kurtosis imaging and dynamic contrast-enhanced magnetic resonance imaging in differentiating benign and malignant head and neck lesions. *J Magn Reson Imaging* 2022; **55**: 414–23. https://doi.org/10.1002/jmri.27885

15. Xiao Z, Zhong Y, Tang Z, Qiang J, Qian W, et al. Standard diffusion-weighted, diffusion kurtosis and intravoxel incoherent motion MR imaging of sinonasal malignancies: correlations with ki-67 proliferation status. *Eur Radiol* 2018; **28**: 2923–33. https://doi.org/10.1007/s00330-017-5286-x

16. Song C, Cheng P, Cheng J, Zhang Y, Sun M, et al. Differential diagnosis of nasopharyngeal carcinoma and nasopharyngeal lymphoma based on DCE-MRI and RESOLVE-DWI. *Eur Radiol* 2020; **30**: 110–18. https://doi.org/10.1007/s00330-019-06343-0

17. Cheng Z, Wu Z, Shi G, Yi Z, Xie M, et al. Discrimination between benign and malignant breast lesions using volumetric quantitative dynamic contrast-enhanced MR imaging. *Eur Radiol* 2018; **28**: 982–91. https://doi.org/10.1007/s00330-017-5050-2

18. Qian W, Xu X-Q, Hu H, Su G-Y, Wu J-F, et al. Dynamic contrast-enhanced MRI in orbital lymphoproliferative disorders: effects of region of interest selection methods on time efficiency, measurement reproducibility, and diagnostic ability. *J Magn Reson Imaging* 2018; **47**: 1298–1305. https://doi.org/10.1002/jmri.25859

19. Dong Ji X, Yan S, Xia S, Guo Y, Shen W, et al. Quantitative parameters correlated well with differentiation of squamous cell carcinoma at head and neck: a study of dynamic contrast-enhanced MRI. *Acta Radiol* 2019; **60**: 962–68. https://doi.org/10.1177/0284185118809543

20. Meyer H-J, Hamerla G, Leifels L, Höhn AK, Surov A, et al. Histogram analysis parameters derived from DCE-MRI in head and neck squamous cell cancer - associations with microvessel density. *Eur J Radiol* 2019; **120**: S0720-048X(19)30319-5: 108669: . https://doi.org/10.1016/j.ejrad.2019.108669

21. Ota Y, Liao E, Capizzano AA, Kurokawa R, Bapuraj JR, et al. Diagnostic role of diffusion-weighted and dynamic contrast-enhanced perfusion MR imaging in paragangliomas and schwannomas in the head and neck. *AJNR Am J Neuroradiol* 2021; **42**: 1839–46. https://doi.org/10.3174/ajnr.A7266

22. Lee JY, Cheng KL, Lee JH, Choi YJ, Kim HW, et al. Detection of local recurrence in patients with head and neck squamous cell carcinoma using voxel-based color maps of initial and final area under the curve values derived from DCE-MRI. *AJNR Am J Neuroradiol* 2019; **40**: 1392–1401. https://doi.org/10.3174/ajnr.A6130

FULL PAPER

Dynamic contrast-enhanced breast magnetic resonance imaging findings that affect the magnetic resonance-directed ultrasound correlation of non-mass enhancement lesions: a single-center retrospective study

[1]ALMILA COSKUN BILGE, [2]PINAR ILHAN DEMIR, [3]HALE AYDIN and [1]ISIL ESEN BOSTANCI

[1]Department of Radiology, Dr Abdurrahman Yurtaslan Ankara Oncology Training and Research Hospital, Ankara, Turkey
[2]Department of Radiology, Ministry of Health Ankara City Hospital, Ankara, Turkey
[3]Department of Radiology, Gulhane School of Medicine, University of Health Sciences, Ankara, Turkey

Address correspondence to: Dr Almila Coskun Bilge
E-mail: *almilacoskun@gmail.com*

Objective: Our single-center retrospective study aimed to evaluate the relationship between magnetic resonance (MR)-directed ultrasound (MDUS) detectability and MRI findings of non-mass enhancement (NME) lesions, regarding the morphologic and enhancement features, the distance from the skin and nipple, and the presence of concomitant landmarks.

Methods: A total of 350 MRI-detected NME lesions that were determined between January 2015 and May 2019 and subsequently underwent MDUS were analyzed. The MRI findings, biopsy results, and follow-up outcomes of lesions were recorded. The correlation between the MRI findings of the lesions and MDUS detectability was analyzed.

Results: 114 (32.6%) of the 350 lesions had a counterpart in the MDUS. Respectively, 66 (37.9%), 38 (43.2%) and 59 (38.3%) of the lesions detected in MDUS were larger than 20 mm in size, with a distance of less than 20 mm to the nipple and 15 mm to the skin. The lesion size and lesion distance to the nipple and skin were significantly associated with a ultrasound correlate ($p < 0.05$). The MDUS detection rate was significantly higher in NME lesions with MR findings including diffuse distribution ($p < 0.001$), clustered-ring enhancement pattern ($p < 0.001$), washout kinetic curve ($p = 0.006$), and MR-BIRADS category 5 ($p < 0.001$). Multivariate logistic regression showed that only the clustered-ring enhancement pattern was significantly associated with an MDUS correlation ($p < 0.001$).

Conclusion: Statistically significant correlations were found between the size, distance to the nipple and skin, distribution pattern, enhancement pattern and kinetic curve of the NME lesions on MRI and ultrasound detectability.

Advances in knowledge: We found that clustered-ring enhancement patterns were significantly more frequent in MR-directed ultrasound detectable lesions.

INTRODUCTION

Dynamic contrast-enhanced magnetic resonance imaging (DCE-MRI) has high sensitivity in detecting breast lesions.[1–4] Lesions that cannot be detected on mammography (MG) and ultrasonography (US), especially in dense breasts, can be detected in MRI.[3,5,6] MRI-guided biopsy or follow-up of the lesion with MRI, which are used for the management of these pathologies, is expensive, time-consuming, and uncomfortable for the patient.[7,8] Therefore, MRI-directed ultrasound (MDUS) is often used when suspicious or indeterminate MRI findings are obtained.[2,9]

MDUS is a repetition of US after MRI that is carefully performed to evaluate the location of the pathology detected in MRI.[1,10]

Biopsy and follow-up of lesions detected on MRI and correlated with the US are performed under US guidance. A US-guided biopsy is cheaper, more accessible, more comfortable, takes little time, and does not require the use of a contrast agent compared with an MRI-guided biopsy.[11–13] However, failure to detect lesions in MDUS or incorrect correlation may have disadvantages such as time-wasting and additional costs.[9]

Non-mass enhancement (NME) has been defined by the Breast Imaging Reporting and Data System (BIRADS) lexicon of the American College of Radiology (ACR) as an area of contrast enhancement whose morphology is not compatible with the focus or the space-occupying mass.[14] Both malignant and benign lesions may present as NME on MRI.[15,16] The features of NME lesions are less specific and more compelling than those of masses.[15,17] Therefore, additional auxiliary methods such as MDUS are used to increase the accuracy of MRI in the characterization of these lesions.[10,15,16] In previous studies, the detectability of NME lesions in MDUS was found to be lower than in mass lesions.[2,3,7,8] Referring NME lesions for MDUS that are predicted to be highly detectable in MDUS according to MRI findings, and managing the diagnosis and follow-up of other lesions with MRI without being directed to MDUS will save time and expense. In the literature, only a few studies have solely evaluated the MDUS correlation of NME lesions.[1,9]

Our study aimed to evaluate the relationship between the MRI findings of NME lesions including morphologic and enhancement features, their distance from the skin and nipple, and the presence of accompanying landmarks and their US correlations.

METHODS AND MATERIALS
Patient data
This single center retrospective study was approved by the institutional review board. The data of patients who underwent breast DCE-MRIs between January 2015 and May 2019 were retrieved from the electronic medical data archive of the radiology department of Dr Abdurrahman Yurtaslan Ankara Oncology Training and Research Hospital. As a result, 5680 patients were identified. The records of the clinical information, MRI examinations, and other breast imaging examination reports of the patients were evaluated. Figure 1 shows the flowchart illustrating how patients

were selected for inclusion in the study. We found 927 patients who had lesions that could not be detected in the previous US and MG examinations, had no palpation findings, could only be observed on MRI, and were recommended for MDUS as a complimentary examination. Among these patients, those with NME lesions detected on MRI were selected. Accordingly, a total of 412 patients who were recommended to undergo MDUS and had NME lesions were recruited for the study. 28 of these patients were excluded because they did not attend MDUS examinations and 53 were excluded because they did not attend the recommended MRI or US-guided biopsy or did not complete the 2 year follow-up. 21 patients were excluded from the study when it was determined that they did not have NME lesions during the reanalysis of the MR images according to the BIRADS fifth edition lexicon by radiologists experienced in breast imaging.[14] Thus, the final study group comprised 338 patients. 12 patients had NME lesions in both breasts. Therefore, MRI findings of 350 lesions were included in our study.

The ages of the patients and the clinical indications for MRI scans were obtained from the electronic medical data archive. All patients were females. The average age of the patients was 46.01 ± 11.12 (range, 20–81) years. Of the 338 patients, 105 had breast cancer in their first-degree relatives and were in the high-risk group. 49 patients had biopsy-proven primary breast cancer who had not received any treatment before undergoing imaging. The indications for breast MRI were as follows: screening at high risk of breast cancer (105 of 338 [67.0%]), pre-operative staging of newly diagnosed breast cancer (49 of 338 [23.8%]), and problem-solving for any findings detected in MG or US (184 of 338 [9.2%]). 350 lesions were obtained from 338 patients. Of the lesions, 37 (32.5%) had a 2-year US follow-up, 77 (67.5%) underwent US-guided Tru-cut biopsy, 183 (77.5%) had a 2-year MRI follow-up, and 53 (22.5%) underwent MRI-guided Tru-cut

Figure 1. Inclusion flowchart. MDUS, magnetic resonance-directed ultrasound; NME, non-mass enhancement.
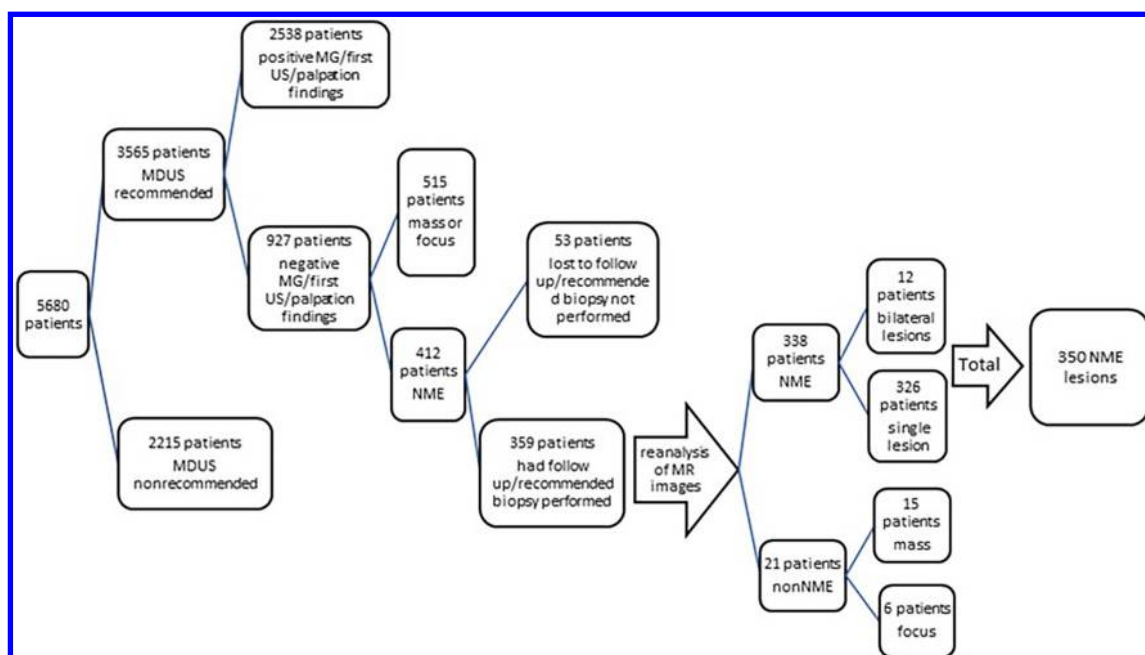
biopsy. The outcomes of the patients who were followed up for 2 years and the pathology results of those who underwent biopsy were evaluated.

MRI technique

All patients were examined using a 1.5 T MR scanner (SignaHDx; GE Healthcare, Wisconsin). All patients were examined in the prone position using a breast array coil. Imaging parameters were as follows: repetition time/echo time (TR/TE) = 6500/45, TI: 150 ms, field of view (FOV): 320 mm, matrix: 416 × 224, number of excitations (NEX): 1, and slice thickness (ST): 5 mm for axial STIR sequences; TR/TE = 400/8.8, FOV: 320 mm, matrix: 448 × 224, NEX: one and ST: 5 mm for axial T_1W images; TR/TE = 4/1.5, FA: 10°, FOV: 320 mm, matrix: 350 × 350, NEX: one and ST: 2.8 mm for dynamic axial fat-saturated (FS) T_1W images (before and after contrast injection); and TR/TE = 1000/83, FOV: 320 mm, matrix: 192 × 192, NEX: four and ST: 5 mm for echoplanar imaging (EPI) based diffusion-weighted imaging (DWI). Gadobutrol/Gadoterate meglumine with a dose of 0.1 mmol/kg was used as a contrast agent for dynamic contrast-enhanced sequences. Images were taken once before the contrast agent and five times after contrast injection. Standard subtraction images were obtained by automatically subtracting pre-contrast images from post-contrast images. Maximum-intensity projection (MIP), and multiplanar reconstruction (MPR) images were reconstructed. Conventional kinetic analysis was performed using a time–intensity curve in the delayed phase for NME lesions. Measurements were made from the most intensely enhanced areas of the NME lesions by excluding normal breast tissues. Kinetic curves were constructed automatically by the device.

Analysis of MR images

MR images were evaluated retrospectively on one workstation by two radiologists who had 2 and 6 years' experience in breast imaging. The radiologists were blinded to the clinical indications and the pathology reports and 2-year follow-up results. Each case was evaluated through consensus between the two radiologists. Breast density (BD) and background parenchymal enhancement (BPE) were recorded and categorized according to the BIRADS lexicon.[14] BD was evaluated considering the proportion of fibroglandular tissue (FGT) in the breast on the T_1W and T_2W images and was classified as predominantly fatty, scattered, heterogeneously dense or extremely dense. BPE was interpreted as minimal, mild, moderate, and marked, by evaluating the degree of normal FGT contrast enhancement in the early phase of post-contrast T_1W FS sequences.[14] The size of each NME lesion and its distance from anatomic structures including the nipple and skin were evaluated using post-contrast T_1W FS, MIP, and MPR images. The largest size of the lesions was recorded. Telegrafo et al measured the distances of the lesions to the skin and the nipple separately using MRI and ultrasonography and found that the displacement caused by the difference in position in both imaging modalities was less than 1 cm.[18] Therefore, in our study, we also used these anatomic structures to locate the lesions on MR images. The distances from the lesion to the nipple and from the lesion to the skin were measured from

the margin of the NME closest to these structures to the base of the nipple and skin, respectively.

The lesions were evaluated according to the definition of NME specified in the BIRADS lexicon, "an enhancement area with non-enhancing fatty or glandular tissue areas that is unlike a focus (punctuate enhancement less than 5 mm in size) or mass (an enhancement lesion larger than 5 mm in three dimensions occupying space)."[14] When the lesions of the study patients were evaluated according to this definition, 18 lesions were reclassified as mass and three as foci, and these lesions were excluded from the study. The distribution and the internal enhancement patterns of the NME lesions were analyzed according to the lexicon on the post-contrast subtraction, MIP, and sagittal MPR images (Figure 2).[14,19] The distributions of the NME lesions were classified as focal, linear, segmental, regional, multiple regions, and diffuse. The internal enhancement pattern was evaluated as homogeneous, heterogeneous, clumped, and clustered-ring. The kinetic characteristics of the enhancement pattern of the lesions were analyzed as washout, plateau, or persistent curve types. Finally, in line with the BIRADS lexicon, each lesion was assigned an MR-BIRADS category of 3, 4, or 5.

LANDMARK EVALUATION

To determine the location of the lesions detected in MRI more clearly with ultrasonography, MRI findings adjacent to the lesion, called landmarks, if available, were used as a guide. Landmark types were determined as post-operative changes (scar or seroma), and malignant and benign lesions. The presence of landmarks was investigated in MR images. Landmark type and the distance between landmarks and lesions were noted. If the lesion evaluated had an accompanying landmark, its position regarding the landmark was evaluated on MR images and this area was carefully examined during the US examination.

MR-DIRECTED ULTRASONOGRAPHY

Recommended MDUS examinations were performed by radiologists an average of 9 (range, 1–26) days after MRI. A 6–15 MHz linear array transducer (Logiq S7 Expert; General Electric Healthcare Ultrasound Systems, Chicago, USA) was used. Before performing the US examination, the patient's MRI report and images were carefully examined. US was performed for the NME lesion, for which MDUS was recommended, considering the location of the lesion, its size, presence of landmarks, distance to the nipple and skin, and if present, the landmark. During US imaging, the patients were in the supine or supine oblique position with their arms raised. It was noted whether the lesion could be detected in the US examination. The reports of the MDUS were collected retrospectively from the electronic medical data archive. Each MDUS report was evaluated by two radiologists and it was recorded whether the NME lesions correlated with the US findings. MDUS correlation of the NME lesions was ensured by examining the compatibility of the location, size, and morphologic features of the MR images of the NME lesions and their counterparts specified in the MDUS report. US imaging findings of lesions detected in MDUS were determined. The imaging findings, including the lesion shape (oval/round or irregular), margin (circumscribed, indistinct, angular,

Figure 2. A 48-year-old female with bloody nipple discharge from the right breast. No abnormalities were seen on the mammogram and first ultrasonography. (a) Axial post-contrast T_1 weighted fat-suppressed MR subtraction image shows BIRADS category 4 non-mass enhancement with heterogeneous internal pattern and segmental distribution (arrows). (b) MR-directed ultrasonography image shows an irregularly shaped, hypoechoic lesion parallel to the skin with indistinct margins and no posterior shadowing, in the location of the NME on MRI (arrows). The final biopsy showed low-grade ductal carcinoma *in situ*. NME, non-mass enhancement.
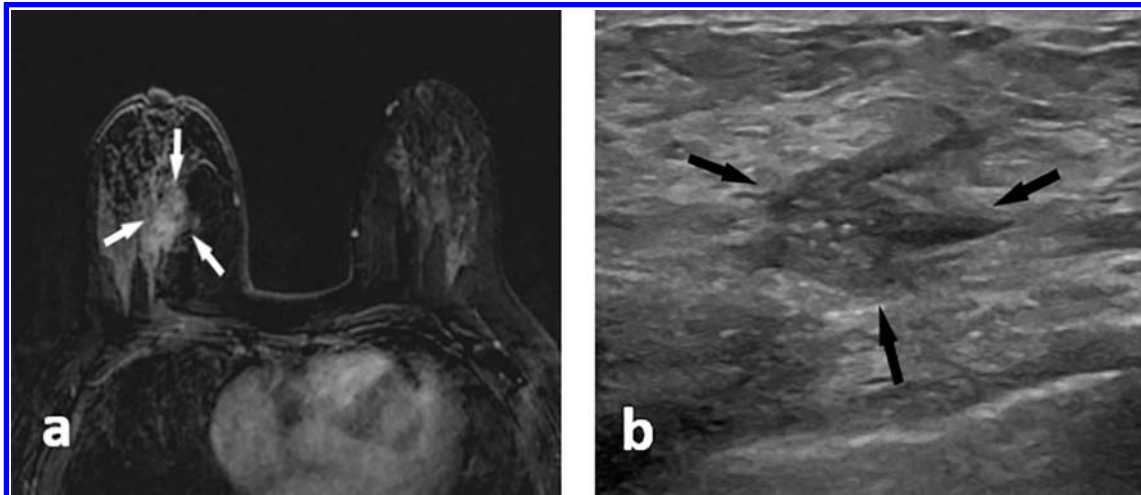
microlobulated, spiculated), orientation (parallel, not parallel) echo pattern (anechoic, hyperechoic, hypoechoic, isoechoic, mixed), and posterior acoustic features (no features, enhancement, shadowing, combined pattern) of the correlated lesions, were noted.

DATA EVALUATION

DCE-MRI images and MDUS results were reevaluated for each lesion by the radiologists according to the lexicon. Patients with NME lesions suggestive of being benign had imaging follow-up for 2 years. NME lesions that could be detected on the MDUS were followed up using US, and those that were not detected were followed up using MRI. The US detection of NME lesions suspected of malignancy has enabled US-guided biopsy. Otherwise, an MRI-guided biopsy was performed for sonographically occult lesions. The 2 year follow-up and pathology results of the study patients were obtained from the electronic medical data archive and recorded. Lesions that were stable after 2 years of imaging follow-up were considered benign. The pathologic diagnoses of the biopsied lesions were examined and classified as benign and malignant lesions.

STATISTICAL ANALYSIS

Statistical analyses were performed using the IBM SPSS package program v. 24.0 (IBM Corporation, Armonk, NY). Continuous variables including patient age, lesion and landmark size, and lesion distance to the nipple/skin/landmark are expressed as mean ± standard deviation, or median (min-max), and categorical data including the number of pathologic diagnoses of the lesions, the sonographic features of the lesions with MDUS correlation, the distribution of MRI findings, and the landmark characteristics according to MDUS non-correlated and correlated lesions as numbers and percentages. In the intergroup analysis of continuous variables, normality analyses were performed using the Kolmogorov–Smirnov goodness-of-fit test. Intergroup analyses

of continuous variables with normal distribution were performed using the independent samples *t*-test, and those that did not fit were performed using the Mann–Whitney *U* test. Univariate logistic regression was performed on the variables of BD, BPE, lesion to skin/nipple distance (grouped), lesion size (grouped), lesion distribution, lesion enhancement pattern, lesion kinetic curve type, MR-BIRADS category, presence of landmarks, and pathologic results. The lesion to skin/nipple distance (grouped), lesion size (grouped), lesion distribution, lesion enhancement pattern, lesion kinetic curve type, MR-BIRADS category pathologic type results that were statistically significant were included in multivariate analysis. A multivariate classification and regression tree algorithm was used to calculate a predictive model for MDUS detection rates. The Hosmer–Lemeshow test was used for model fit. The Type 1 error to define the presence of statistical was set to 5% for all statistical analyses. A *p*-value less than 0.05 was accepted to show statistical significance.

RESULTS

In the current study, 350 lesions of 338 patients were evaluated. All 350 lesions included in the study were of the NME lesion type and MDUS was performed on all of them. 114 (32.6%) of the lesions had a counterpart in the MDUS, 236 (67.4%) did not.

Follow-up and biopsy results of NME lesions

After evaluation of the follow-up and biopsy results, 58 of 350 lesions were found as malignant and 292 as benign. Biopsy was performed on all malignant lesions and 72 of the 292 benign lesions. The pathologic diagnoses obtained are shown in Table 1. 26 (44.8%) of 58 malignant lesions and 88 (30.1%) of the 292 benign lesions were correlated with the US findings. The relationship between the pathologic lesion type and the MDUS correlation was statistically significant (*p* = 0.031). The detection rate of malignant NME lesions in US was 1.8 times higher than for benign lesions.

Table 1. The pathologic diagnoses of NME lesions

Pathology	No. of lesions (n)(%)	Pathology	No. of lesions (n) (%)
Malignant lesions	**58 (100)**	**Benign lesions**	**72 (100)**
DCIS	47 (81)	Adenosis	17 (23.6)
IDC	5 (8.6)	IDP	14 (19.4)
ILC	3 (5.2)	ADEH	11 (15.3)
Papillary carcinoma	2 (3.5)	Fibrocystic changes	9 (12.5)
Micropapillary carcinoma	1 (1.7)	LCIS	8 (11.1)
		Sclerosing lesions	5 (6.9)
		Mastitis	3 (4.2)
		Fat necrosis	3 (4.2)
		Fibroepithelial lesion	2 (2.8)

NME, non-mass enhancement; DCIS, ductal carcinoma *in-situ*; IDC, invasive ductal carcinoma; ILC, invasive lobular carcinoma; IDP, intraductal papilloma; ADEH, atypical ductal epithelial hyperplasia; LCIS, lobular carcinoma *in situ*

RELATION OF BREAST DENSITY ON MRI TO MDUS VISIBILITY OF NME

When the breast density on MRI was considered as predominantly fatty, scattered, heterogeneously dense, and extremely dense, the detection rates in MDUS were 6 (24%) in 25 lesions, 16 (35.6%) in 45 lesions, 58 (30.9%) in 188 lesions, and 34 (37%) in 92 lesions, respectively; no statistically significant difference was found between the groups ($p = 0.556$) (**Table 2**).

DCE-MRI findings associated with MDUS visibility of NME

DCE-MRI findings were analyzed to determine predictors of NME lesions having MDUS correlation. When BPE was compared with detectability in MDUS separately, no statistically significant difference was found between them ($p = 0.861$) (Table 2). The size of NME lesions detected on MRI was 2 (range, 7–106) mm in US correlated lesions, whereas it was 19 (range, 5–87) mm in cases not correlated with the US, which was statistically significantly different ($p = 0.002$). When the lesion sizes were classified as smaller and larger than 20 mm, the detection rate of lesions larger than 20 mm in the MDUS was found 1.6 times higher than the other group.

Table 2. Comparison of MR-directed ultrasonography non-correlated and correlated NME lesions in terms of patients' age, numerical values related to the NME lesions, breast density, and background parenchymal enhancement.

	MR-directed ultrasonography non-correlated ($n = 236$)	MR-directed ultrasonography correlated ($n = 114$)	*p*-value
Age (year) (mean ± SD)	45.97 ± 11.14	46.10 ± 11.13	0.916
Lesion median size (mm) (min.–max.)	19 (5–87)	25 (7–106)	0.002
Distance to the nipple (mm) (mean ± SD)	34.37 ± 20.09	30.25 ± 19.86	0.072
Distance to the skin (mm) (mean ± SD)	19.03 ± 9.28	16.16 ± 8.12	0.005
Breast density (n) (%)			
Predominantly fatty	19 (76)	6 (24)	0.556
Scattered	29 (64.4)	16 (35.6)	
Heterogeneously dense	130 (69.1)	58 (30.9)	
Extremely dense	58 (63)	34 (37)	
BPE (n) (%)			
Minimal	72 (64.9)	39 (35.1)	0.861
Mild	78 (70.3)	33 (29.7)	
Moderate	58 (67.4)	28 (32.6)	
Marked	28 (66.7)	14 (33.3)	

NME, non-mass enhancement; BPE, background parenchymal enhancement

In DCE-MRI, the distances of NME lesions to the nipple were 30.25 ± 19.86 mm and 34.37 ± 20.09 mm in those detected and undetected on the MDUS, respectively, and no statistically significant difference was found between the two groups (*p* = 0.072) **(Table 2).** However, when the nipple–lesion distance was classified as closer than 20 mm, between 20 and 45 mm and farther than 45 mm, the lesions closer than 20 mm to the nipple had the highest detection rate (43.2%) in MDUS, which was statistically significantly different (*p* = 0.004) (Table 3). Lesions closer than 20 mm to the nipple were 2.3 times more detectable

Table 3. The distribution of MRI findings of NME lesions according to MR-directed US non-correlated and correlate

MRI findings	MR-directed ultrasonography non-correlated (n)(%)	MR-directed ultrasonography correlated (n)(%)	*p*-value	Odds ratio (95% CI)
Lesion size				
≥20 mm	128 (72.7)	48 (27.3)	0.034	1.00
<20 mm	108 (62.1)	66 (37.9)		1.63 (1.03–2.55)
Distance to the nipple				
>45 mm	73 (76.8)	22 (23.2)	0.017	1.00
20–45 mm	113 (67.7)	54 (32.3)	0.087	1.58 (0.88–2.83)
<20 mm	50 (56.8)	38 (43.2)	0.004	2.30 (1.20–4.40)
Distance to the skin				
>15 mm	141 (71.9)	55 (28.1)	0.043	1.00
≤15 mm	95 (61.7)	59 (38.3)		1.59 (1.01–2.49)
Distribution of the lesion				
Focal	94 (68.1)	44 (31.9)	0.003	1.00
Regional	81 (68.1)	38 (31.9)	0.993	1.00 (0.59–1.69)
Linear	54 (78.3)	15 (21.7)	0.130	0.59 (0.30–1.16)
Segmental	6 (35.3)	11 (64.7)	0.011	3.91 (1.36–11.27)
Diffuse	1 (14.3)	6 (85.7)	0.020	12.81 (1.49–109.71)
Internal enhancement patterns of the lesion				
Homogeneous	48 (78.7)	13 (21.3)	<0.001	1.00
Heterogeneous	77 (67.5)	37 (32.5)	0.122	1.77 (0.85–3.67)
Clumped	108 (69.2)	48 (30.8)	0.166	1.64 (0.81–3.30)
Clustered ring	3 (15.8)	16 (84.2)	<0.001	19.692 (4.96–78.04)
Delayed phase kinetic curve type				
Persistent	141 (74.6)	48 (25.4)	0.007	1.00
Plateau	54 (61.4)	34 (38.6)	0.026	1.85 (1.07–3.17)
Washout	41 (56.2)	32 (43.8)	0.004	2.29 (1.30–4.04)
MR-BIRADS				
Category 3	189 (82.2)	41 (17.8)	<0.001	1.00
Category 4	45 (42.5)	61 (57.5)	<0.001	6.24 (3.74–10.42)
Category 5	2 (14.3)	12 (85.7)	<0.001	27.65 (5.96–128.31)
Presence of landmark				
No	183 (68.3)	85 (31.7)	0.376	1.00
Yes	53 (64.6)	29 (35.4)		1.17 (0.70–1.98)
Pathology results				
Benign	204 (69.9)	88 (30.1)	0.031	1.00
Malignant	32 (55.2)	26 (44.8)		1.88 (1.06–3.34)

NME, non-mass enhancement; CI, confidence interval

Figure 3. A 39-year-old female with a familial high risk for breast cancer. No abnormalities were seen on the mammogram and first ultrasonography. (a) Axial post-contrast T_1 weighted fat-suppressed MR subtraction image shows BIRADS category 4 non-mass enhancement with clustered ring internal pattern and regional distribution in right breast (arrows). (b) MR-directed ultrasonography image shows an irregularly shaped, hypoechoic area parallel to the skin with indistinct margins and no posterior shadowing in the localization of NME on MRI (arrows). The final biopsy showed low-grade ductal carcinoma *in situ*. NME, non-mass enhancement.

than those farther than 45 mm. The distances of NME lesions to the skin were measured as 16.16 ± 8.12 mm and 19.03 ± 9.28 mm detected and undetected on the MDUS, respectively, and a statistically significant difference was found between the two groups ($p = 0.005$) **(Table 2).** When the skin–lesion distance was class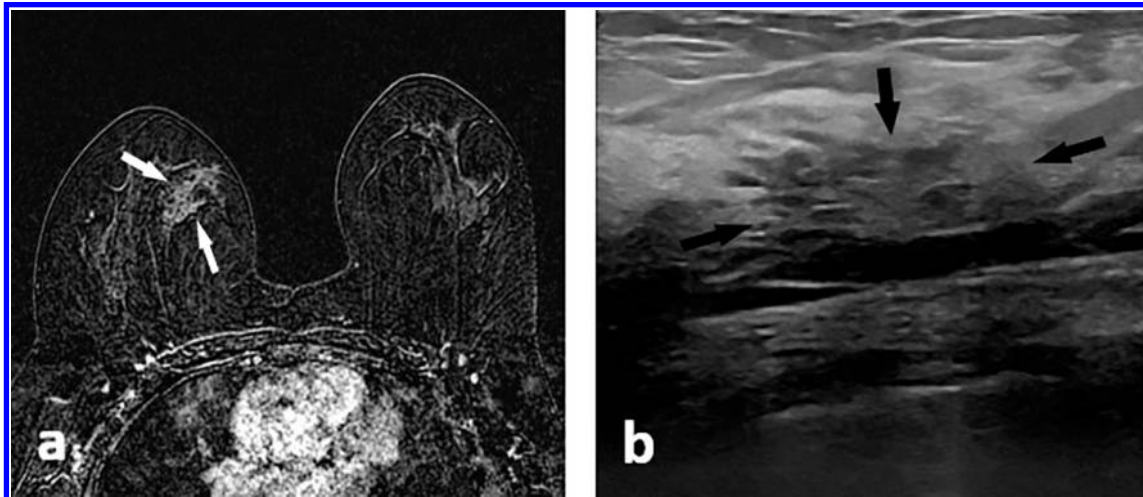ified as farther than 15 mm and closer than 15 mm, the detection rates of MDUS were 55 (28.1%) in 196 lesions and 59 (38.3%) in 154 lesions, respectively. It was found that if the distance of the lesion to the skin was closer than 15 mm, it was 1.5 times more likely to be detected in the MDUS compared to those that were farther apart.

When the distribution of NME lesions on MRI was considered as focal, regional, segmental, diffuse, and linear, the detection rates in MDUS were 44 (31.9%) in 138 lesions, 38 (31.9%) in 119 lesions, 15 (21.7%) in 69 lesions, 11 (64.7%) in 17 lesions, and 6 (85.7%) in 7 lesions, respectively **(Table 3).** There were no NME lesions with multiple region distribution in our study. The rate of MDUS detectability was significantly higher in the lesions with diffuse distribution compared with other distributions ($p = 0.020$).

According to the enhancement patterns of NME lesions, MDUS detectability rates were 21.3%, 32.5%, 30.8%, and 84.2% in homogeneous, heterogeneous, clumped, and clustered-ring enhancement patterns, respectively **(Table 3).** Compared with homogeneously enhanced lesions, clustered-ring enhanced lesions were detected 19 times more in MDUS, which was statistically significant ($p < 0.001$) (Figure 3).

Among the NME lesions, 48 (25.4%) of 189 lesions were persistent kinetic curve type, 34 (38.6%) of 88 lesions were plateau, and 32 (43.8%) of 73 lesions with washout were detected in MDUS. The probability of detecting kinetic curve-type lesions in MDUS was found to be statistically significant ($p = 0.007$)

(Table 3). Compared with lesions with a persistent kinetic curve, the detection rates of lesions with plateau and washout in US were 1.85 and 2.3 times higher, respectively.

MR-BIRADS category of NME associated with MDUS visibility

According to the MR-BIRADS, MDUS detectability rates were 17.8%, 57.5%, and 85.7%, in BIRADS category 3, 4, and 5, respectively, and were statistically significant ($p < 0.001$) **(Table 3).** Compared with BIRADS category 3 lesions, category 4 lesions were detected 6.2 times and category 5 lesions 27.6 times more in MDUS.

MDUS imaging findings of the correlated lesions

The shape, margin, orientation, echo pattern, and posterior acoustic features of the 114 NME lesions identified in MDUS are shown in Table 2. These lesions tended to be suspicious (73.7% had an indistinct margin, 89.5% of lesions were hypoechoic). Findings suggestive of malignancy were often not present (only 6.1% of lesions had spiculated margin, and 19.3% exhibited posterior acoustic shadowing) (Table 4).

Relationship between presence of landmarks and the detectability of NMEs in MDUS

In our study, 82 (23.4%) NME lesions had landmarks. Landmark types were benign lesions in 46 (56.1%) (Figure 4), malignant lesions in 31 (37.8%), and post-operative changes in five (6.1%). The mean landmark size was 16.1 ± 10.2 (range: 3–55) mm. The mean distance between the landmark and the lesion was 6.7 ± 5.8 (range: 0–31) mm. Landmarks accompanied 29 (25.4%) US-correlated lesions and 53 (22.4%) US non-correlated lesions. No statistically significant difference was found between the US correlation of NME lesions and the presence of landmarks, size, type, and distances between landmarks and lesions (Table 5).

Table 4. Sonographic features of the 114 NME lesions with MDUS correlation

Sonographic feature	No. of lesions (n) (%)
Shape	
Oval or round	77 (67.5)
Irregular	37 (32.5)
Margin	
Circumscribed	6 (5.3)
Indistinct	84 (73.7)
Angular	8 (7)
Microlobulated	9 (7.9)
Spiculated	7 (6.1)
Orientation	
Parallel	92 (80.7)
Not parallel	22 (19.3)
Echo pattern	
Hypoechoic	102 (89.5)
Mixed	12 (10.5)
Other (anechoic, isoechoic, hyperechoic)	0 (0)
Posterior acoustic features	
No posterior acoustic features	82 (72)
Posterior acoustic shadow	16 (14)
Combined pattern	16 (14)

NME, non-mass enhancement

Multivariate analysis of findings

A multivariate logistic model was developed for the variables including the lesion size, lesion distance to skin and nipple, pathologic results, MR-BIRADS category, kinetic curve type, enhancement pattern, and distribution. Among these variables, the most significant parameter was found to be the lesion enhancement pattern. Accordingly, the clustered-ring pattern was found to be a predictor for MDUS detection of NMEs ($p < 0.001$).

DISCUSSION

NME lesions are a challenging subgroup that can be detected incidentally in MRI, which is challenging in interpretation and management. In the management of suspicious and undetermined NME lesions detected in MRI and in preventing false-positive diagnoses, MDUS plays an important role by providing additional information.[3,7,15,20] In the literature, studies are investigating the success of MDUS in detecting MR-only lesions.[1–3,7–12,20] In these studies, the detection rate of NME lesions in MDUS is 0–88%, which is a wide range. This may be due to the inclusion of all lesion types, including masses, NME, and foci in the studies, and the low rate of NME lesions among them. However, Newburg et al and Hsu et al evaluated NME lesions only, and the number of the lesions was 284 and 102, respectively. In our study, the number of NME lesions was 350, which was higher compared with other studies in the literature. The rates of MDUS-correlated lesions were 23% in the study of Newburg et al, 43% in the study of Hsu et al, and 29% in the meta-analysis of Spick et al.[9,15,21] In our study, this rate was found as 32.6%, which is compatible with the literature.

The results of our study indicated that the dynamic MRI features of NME lesions, including distribution, enhancement pattern, and contrast enhancement kinetics, had important roles in US detectability. The NME lesions with segmental and diffuse distribution, with clustered-ring enhancement patterns, and with washout contrast enhancement kinetics tended to be detected in MDUS more frequently. The detectability of NME lesions with linear distribution in US was found to be the lowest, which is consistent with the study of Bumberger et al.[22] By contrast, Newburg et al found no correlation between the dynamic MRI features of NME lesions and US correlation.[9] However, in their study, the number of lesions with the clustered-ring enhancement pattern and with washout enhancement kinetics was quite low compared with our study.

Figure 4. A 46-year-old female with bloody nipple discharge from the left breast. No abnormalities were seen on the mammogram and first ultrasonography. (a) Axial post-contrast T_1 weighted fat-suppressed MR subtraction image shows BIRADS category 4 non-mass enhancement with clumped internal pattern and regional distribution (arrows). (b) Axial T_2 weighted fat-suppressed MR image shows a landmark as cystic focal ductal ectasia areas next to the NME lesion (arrows). (c) MR-directed ultrasonography image shows oval-shaped, lobulated margined, hypoechoic lesions parallel to the skin (white arrows) with cystic ectatic duct-like structures (black arrows) at the NME localization in MRI. The final biopsy showed intraductal papillomas. NME, non-mass enhancement.
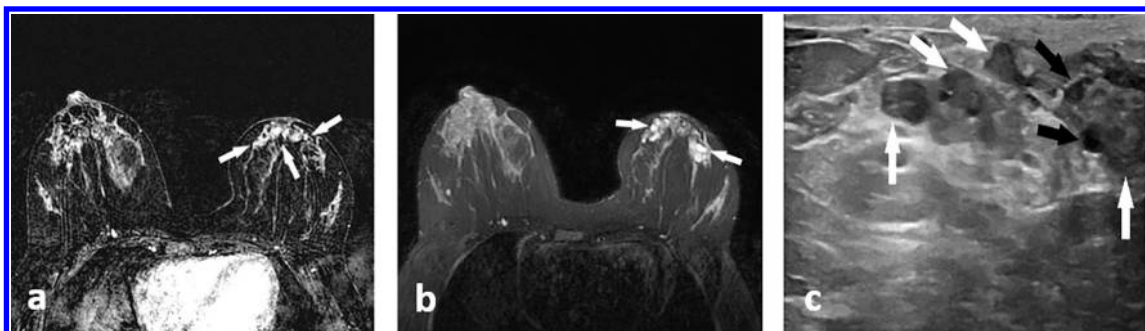
Table 5. Comparison of MR-directed ultrasonography non-correlated and correlated NME lesions in terms of landmark characteristics

	MRI-directed ultrasonography non-correlated ($n = 53$)	MRI-directed ultrasonography correlated ($n = 29$)	*p*-value
Landmark type (%)			
Benign lesion	32 (69.6)	14 (30.4)	0.093
Malign lesion	20 (64.5)	11 (35.5)	
Post-operative changes	1 (20)	4 (80)	
Landmark size (mm) (mean ± SD)	16.28 ± 10.39	15.76 ± 10.12	0.826
Distance to landmark (mm) (mean ± SD)	7.61 ± 5.90	5.10 ± 5.37	0.059

NME, non-mass enhancement.

Our study demonstrated that NME lesions with a more suspicious appearance on MRI (*i.e.* MR-BIRADS category 5 *vs* 4 and category 4 *vs* 3) were more likely to be detected in US. This finding is similar to some studies in the literature.[3,23] Unlike our study, Bumberger et al found no association between MR-BIRADS and ultrasonography correlation.[22] However, in these studies and our study, the number of MR-BIRADS category 5 lesions was quite low.

As in previously published studies, we found a relationship between lesion size and detectability in MDUS.[7,10,11] The probability of lesions larger than 20 mm being detected in US was higher than for lesions smaller than 20 mm. This may be the reason why the lesions with diffuse distribution, which occupy more space in the breast, are easier to visualize in US compared with other distributions. On the other hand, some studies in the literature have shown that lesion size has no impact on US correlation.[2,3,15]

As expected, we found that the distance of lesions to the nipple and skin affected their detectability in US. Lesions closer than 20 mm to the nipple and 15 mm to the skin were more likely to be detected in MDUS than those farther away. Considering that the breast size of each patient is different, Bumberger et al classified the position of the lesions in the breast as those close to the nipple as "retroareolar," those in the prepectoral area as "posterior," and those outside the prepectoral area as "central."[22] Similar to our study, Bumberger et al found that lesions close to the nipple were more likely to be detected in MDUS, but no statistical difference was found between them when compared with other locations.[22] In breast US, as tissue thickness increases, the penetration of US beams decreases, so deep posterior tissues are more difficult to visualize.[24] Consistent with this technical knowledge, the detectability of lesions close to the skin in US was found to be higher in our study.

Chikarmane et al found that the probability of detecting lesions in US in patients with minimal and mild BPE was higher than those with moderate and marked BPE.[11] The reason for this may be that moderate and marked BPE appear as NME, leading to false-positive diagnoses.[25,26] Consistent with some previous studies, we found no relationship between BD and BPE with the detectability of lesions in MDUS.[3,9]

In other studies in the literature, similar to our study, high rates have been reported for indistinct margins and hypoechoic echo patterns as the ultrasonography equivalent of NME lesions.[7,15,27] Uematsu and Sotome et al defined lesion-like hypoechoic areas with indistinct margins on two different projections with no obvious form or contours as non-mass lesions in US and found that these lesions tended to appear as NMEs on breast MRI.[28,29] We also found that NMEs detected on MRI were highly present with indistinct margins and hypoechoic echo patterns in US. In addition, we detected benign US findings including round/oval shape, parallel orientation, and having no posterior acoustic shadowing. We thought that this was because the majority of the lesions detected in US (88 of 114 lesions) in our study were benign lesions.

In our study, the detection rate of malignant lesions in MDUS was 44.8%, and for benign lesions, it was 30.1%, which was statistically significant. The results were compatible with the study of Newburg et al.[9] In the studies of Hsu et al and Abe et al, the rates of US-correlated malignant lesions were 77 and 100%, respectively, which were higher compared with our study.[7,15] The reason for this is that although the number of malignant and benign NME lesions in the aforementioned studies were close to each other, this rate was in favor of benign lesions in our study. In addition, in the study by Abe et al, the number of NME lesions was quite low compared with our study.

Of the malignant NME lesions in our study, 81% were diagnosed as ductal carcinoma *in situ* (DCIS) and 13.8% as invasive carcinoma. In the studies by Hsu et al and Newburg et al, DCIS rates were 66.6 and 60%, respectively, and were higher than for invasive carcinoma, similar to our study.[9,15] We thought that this was because DCIS lesions more frequently (60–81%) presented as NME on MRI.[17,30–34]

Breast US is performed in the supine or supine-oblique position with the arms raised to reduce tissue thickness and movement, and breast MRI is performed in the prone position within the breast coil. Due to the positional difference in both modalities, lesions can be observed more anteriorly or in a different location by up to 3–6 cm in the breast in MRI than in US.[35,36] Therefore, accompanying landmarks, if any, are used to accurately predict the location of the lesion in US.[35,37,38] Newburg et al found that

the presence of landmarks at a distance of 3 cm or closer to the lesion increased the probability of US correlation.[9] However, in our study, no statistically significant relationship was found between the presence of landmarks, their size, distance to the lesion and its type, and the probability of detecting lesions in MDUS.

The first limitation of our study is that it is a retrospective and single-center study. Second, the NME lesions included in our study were lesions for which only MDUS was recommended and had no findings in the MG, the first US, and physical examination, so they did not represent all NME lesions. Third, MDUS is practitioner-dependent. As the fourth limitation, because we did not place a clip after the biopsy to lesions in which US-guided biopsy was performed, it was not always possible to be sure of the exact MR-US correlation of these lesions.

CONCLUSION

In conclusion, the size, distance to the nipple and skin, MR-BI-RADS category, distribution patterns, enhancement pattern, and kinetic curve types of NME lesions on MRI, affect the probability of detecting lesions in MDUS. Our results showed that the most significant predictor for MDUS detection of NME was the clustered-ring pattern of enhancement.

REFERENCES

1. Shin JH, Han BK, Choe YH, Ko K, Choi N. Targeted ultrasound for mr-detected lesions in breast cancer patients. *Korean J Radiol* 2007; **8**: 475–83. https://doi.org/10.3348/kjr.2007.8.6.475

2. Wiratkapun C, Duke D, Nordmann AS, Lertsithichai P, Narra V, Barton PT, et al. Indeterminate or suspicious breast lesions detected initially with mr imaging: value of mri-directed breast ultrasound. *Acad Radiol* 2008; **15**: 618–25. https://doi.org/10.1016/j.acra.2007.10.016

3. Lee SH, Kim SM, Jang M, Yun BL, Kang E, Kim SW, et al. Role of second-look ultrasound examinations for mr-detected lesions in patients with breast cancer. *Ultraschall Med* 2015; **36**: 140–48. https://doi.org/10.1055/s-0034-1399143

4. Saadatmand S, Obdeijn I-M, Rutgers EJ, Oosterwijk JC, Tollenaar RA, Woldringh GH, et al. Survival benefit in women with brca1 mutation or familial risk in the mri screening study (mrisc). *Int J Cancer* 1, 2015; **137**: 1729–38. https://doi.org/10.1002/ijc.29534

5. Kuhl CK, Strobel K, Bieling H, Leutner C, Schild HH, Schrading S. Supplemental breast mr imaging screening of women with average risk of breast cancer. *Radiology* 2017; **283**: 361–70. https://doi.org/10.1148/radiol.2016161444

6. Bakker MF, de Lange SV, Pijnappel RM, Mann RM, Peeters PHM, Monninkhof EM, et al. Supplemental mri screening for women with extremely dense breast tissue. *N Engl J Med* November 28, 2019; **381**: 2091–2102. https://doi.org/10.1056/NEJMoa1903986

7. Abe H, Schmidt RA, Shah RN, Shimauchi A, Kulkarni K, Sennett CA, et al. MR-directed ("Second-look") ultrasound examination for breast lesions detected initially on mri: mr and sonographic findings. *AJR Am J Roentgenol* 2010; **194**: 370–77. https://doi.org/10.2214/AJR.09.2707

8. Hong MJ, Cha JH, Kim HH, Shin HJ, Chae EY, Shin JE, et al. Second-look ultrasonography for mri-detected suspicious breast lesions in patients with breast cancer. *Ultrasonography* 2015; **34**: 125–32. https://doi.org/10.14366/usg.14046

9. Newburg AR, Chhor CM, Young Lin LL, Heller SL, Gillman J, Toth HK, et al. Magnetic resonance imaging-directed ultrasound imaging of non-mass enhancement in the breast: outcomes and frequency of malignancy. *J Ultrasound Med* 2017; **36**: 493–504. https://doi.org/10.7863/ultra.16.03001

10. Carbognin G, Girardi V, Calciolari C, Brandalise A, Bonetti F, Russo A, et al. Utility of second-look ultrasound in the management of incidental enhancing lesions detected by breast mr imaging. *Radiol Med* 2010; **115**: 1234–45. https://doi.org/10.1007/s11547-010-0561-9

11. Chikarmane SA, Jin B, Giess CS. Accuracy of mri-directed ultrasound and subsequent ultrasound-guided biopsy for suspicious breast mri findings. *Clin Radiol* March 2020; **75**: S0009-9260(19)30626-9: 185–93: . https://doi.org/10.1016/j.crad.2019.10.013

12. Park SY, Han B-K, Ko ES, Ko EY, Cho EY. Additional lesions seen in magnetic resonance imaging of breast cancer patients: the role of second-look ultrasound and imaging-guided interventions. *Ultrasonography* 2019; **38**: 76–82. https://doi.org/10.14366/usg.18002

13. Mazzei MA, Di Giacomo L, Fausto A, Gentili F, Mazzei FG, Volterrani L. Efficacy of second-look ultrasound with mr coregistration for evaluating additional enhancing lesions of the breast: review of the literature. *Biomed Res Int* 2018; **2018**: 3896946. https://doi.org/10.1155/2018/3896946

14. Morris EA, Comstock CE, Lee CH, et al. ACR BI-RADS® Magnetic resonance imaging. *ACR BI-RADS® Atlas, Breast imaging reporting and data system*. Reston, VA: American College of Radiology; 2013, pp. 56–71.

15. Hsu H-H, Chang T-H, Chou Y-C, Peng Y-J, Ko K-H, Chang W-C, et al. Breast nonmass enhancement detected with mri: uility and lesion characterization with second-look ultrasonography. *Breast J* 2015; **21**: 579–87. https://doi.org/10.1111/tbj.12491

16. Thomassin-Naggara I, Trop I, Chopier J, David J, Lalonde L, Darai E, et al. Nonmasslike enhancement at breast mr imaging: the added value of mammography and us for lesion categorization. *Radiology* 2011; **261**: 69–79. https://doi.org/10.1148/radiol.11110190

17. Mann RM, Cho N, Moy L. Breast mri: state of the art. *Radiology* September 2019; **292**: 520–36. https://doi.org/10.1148/radiol.2019182947

18. Telegrafo M, Rella L, Stabile Ianora AA, Angelelli G, Moschetta M. Supine breast us: how to correlate breast lesions from prone mri. *Br J Radiol* 2016; **89**: 20150497: 1059: . https://doi.org/10.1259/bjr.20150497

19. Rao AA, Feneis J, Lalonde C, Ojeda-Fournier H. A pictorial review of changes in the bi-rads fifth edition. *Radiographics* 2016; **36**: 623–39. https://doi.org/10.1148/rg.2016150178

20. Lunkiewicz M, Forte S, Freiwald B, Singer G, Leo C, Kubik-Huch RA. Interobserver variability and likelihood of malignancy for fifth edition bi-rads mri descriptors in non-mass breast lesions. *Eur Radiol* 2020; **30**: 77–86. https://doi.org/10.1007/s00330-019-06312-7

21. Spick C, Baltzer PAT. Diagnostic utility of second-look us for breast lesions identified at mr imaging: systematic review and meta-

analysis. *Radiology* 2014; **273**: 401–9. https://doi.org/10.1148/radiol.14140474

22. Bumberger A, Clauser P, Kolta M, Kapetas P, Bernathova M, Helbich TH, et al. Can we predict lesion detection rates in second-look ultrasound of mri-detected breast lesions? a systematic analysis. *Eur J Radiol* 2019; **113**: S0720-048X(19)30059-2: 96–100: . https://doi.org/10.1016/j.ejrad.2019.02.008

23. Meissnitzer M, Dershaw DD, Lee CH, Morris EA. Targeted ultrasound of the breast in women with abnormal mri findings for whom biopsy has been recommended. *AJR Am J Roentgenol* 2009; **193**: 1025–29. https://doi.org/10.2214/AJR.09.2480

24. Hooley RJ, Scoutt LM, Philpotts LE. Breast ultrasonography: state of the art. *Radiology* 2013; **268**: 642–59. https://doi.org/10.1148/radiol.13121606

25. Liao GJ, Henze Bancroft LC, Strigel RM, Chitalia RD, Kontos D, Moy L, et al. Background parenchymal enhancement on breast mri: a comprehensive review. *J Magn Reson Imaging* January 2020; **51**: 43–61. https://doi.org/10.1002/jmri.26762

26. Shao Z, Wang H, Li X, Liu P, Zhang S, Cao S. Morphological distribution and internal enhancement architecture of contrast-enhanced magnetic resonance imaging in the diagnosis of non-mass-like breast lesions: a meta-analysis. *Breast J* 2013; **19**: 259–68. https://doi.org/10.1111/tbj.12101

27. Kwon BR, Chang JM, Kim SY, Lee SH, Shin SU, Yi A, et al. Utility and diagnostic performance of automated breast ultrasound system in evaluating pure non-mass enhancement on breast magnetic resonance imaging. *Korean J Radiol* November 2020; **21**: 1210–19. https://doi.org/10.3348/kjr.2019.0881

28. Uematsu T. Non-mass-like lesions on breast ultrasonography: a systematic review. *Breast Cancer* 2012; **19**: 295–301. https://doi.org/10.1007/s12282-012-0364-z

29. Sotome K, Yamamoto Y, Hirano A, Takahara T, Hasegawa S, Nakamaru M, et al. The role of contrast enhanced mri in the diagnosis of non-mass image-forming lesions on breast ultrasonography. *Breast Cancer* 2007; **14**: 371–80. https://doi.org/10.2325/jbcs.14.371

30. Greenwood HI, Heller SL, Kim S, Sigmund EE, Shaylor SD, Moy L. Ductal carcinoma in situ of the breasts: review of mr imaging features. *Radiographics* 2013; **33**: 1569–88. https://doi.org/10.1148/rg.336125055

31. Chan S, Chen J-H, Agrawal G, Lin M, Mehta RS, Carpenter PM, et al. Characterization of pure ductal carcinoma in situ on dynamic contrast-enhanced mr imaging: do nonhigh grade and high grade show different imaging features? *J Oncol* 2010; **2010**: 431341. https://doi.org/10.1155/2010/431341

32. Mossa-Basha M, Fundaro GM, Shah BA, Ali S, Pantelic MV. Ductal carcinoma in situ of the breast: mr imaging findings with histopathologic correlation. *Radiographics* 2010; **30**: 1673–87. https://doi.org/10.1148/rg.306105510

33. Sakamoto N, Tozaki M, Higa K, Tsunoda Y, Ogawa T, Abe S, et al. Categorization of non-mass-like breast lesions detected by mri. *Breast Cancer* 2008; **15**: 241–46. https://doi.org/10.1007/s12282-007-0028-6

34. Gity M, Ghazi Moghadam K, Jalali AH, Shakiba M. Association of different mri birads descriptors with malignancy in non mass-like breast lesions. *Iran Red Crescent Med J* 2014; **16**(12): e26040. https://doi.org/10.5812/ircmj.26040

35. Park VY, Kim MJ, Kim EK, Moon HJ. Second-look us: how to find breast lesions with a suspicious mr imaging appearance. *Radiographics* 2013; **33**: 1361–75. https://doi.org/10.1148/rg.335125109

36. Carbonaro LA, Tannaphai P, Trimboli RM, Verardi N, Fedeli MP, Sardanelli F. Contrast enhanced breast mri: spatial displacement from prone to supine patient's position. preliminary results. *Eur J Radiol* 2012; **81**: e771-4. https://doi.org/10.1016/j.ejrad.2012.02.013

37. Izumori A, Kokubu Y, Sato K, Gomi N, Morizono H, Sakai T, et al. Usefulness of second-look ultrasonography using anatomical breast structures as indicators for magnetic resonance imaging-detected breast abnormalities. *Breast Cancer* 2020; **27**: 129–39. https://doi.org/10.1007/s12282-019-01003-z

38. Ando T, Ito Y, Ido M, Osawa M, Kousaka J, Mouri Y, et al. Pre-operative planning using real-time virtual sonography, an mri/ultrasound image fusion technique, for breast-conserving surgery in patients with non-mass enhancement on breast mri: a preliminary study. *Ultrasound Med Biol* July 2018; **44**: S0301-5629(18)30086-3: 1364–70: . https://doi.org/10.1016/j.ultrasmedbio.2018.03.001

INNOVATIONS IN PROSTATE CANCER SPECIAL FEATURE : FULL PAPER

Zonal anatomy of the prostate using magnetic resonance imaging, morphometrics, and radiomic features: impact of age-related changes

[1]SOPHIE LASCHKAR, MD, [1,2]SARAH MONTAGNE, MD, [3]ERIC DE KERVILER, MD, PhD, [2,4]MORGAN ROUPRET, MD, PhD, [1]OLIVIER LUCIDARME, MD, PhD, [2,5]OLIVIER CUSSENOT, MD, PhD and [1,2]RAPHAELE RENARD PENNA, MD, PhD

[1]Academic Department of Radiology, Hôpital Pitié-Salpétrière, Assistance Publique des Hôpitaux de Paris, Paris, France
[2]Sorbonne Universités, GRC n° 5, Oncotype-Uro, Paris, France
[3]Academic Departement of Radiology, Hôpital Saint Louis, Assistance Publique des Hôpitaux de Paris, Paris, France
[4]Academic Department of Urology, Hôpital Pitié-Salpétrière, Assistance Publique des Hôpitaux de Paris, Paris, France
[5]Academic Department of Urology, Hôpital Tenon, Assistance Publique des Hôpitaux de Paris, Paris, France

Address correspondence to: Pr Raphaele Renard Penna
E-mail: *raphaele.renardpenna@aphp.fr*

Objective: To evaluate the impact of age on the zonal anatomy of the prostate by MRI using morphometric and textural analysis.

Methods: A total of 154 men (mean age: 63 years) who underwent MRI due to a high prostate-specific antigen (PSA) level were included retrospectively. At each MRI examination the following variables were measured: overall dimensions of the prostate (whole gland (WG), transitional zone (TZ), and peripheral zone (PZ)), and thickness of the anterior fibromuscular stroma (AFMS) and the periprostatic venous plexus (PPVP) on T_2 weighted images. Identical regions of interest (ROIs) were delineated on the apparent diffusion coefficient (ADC) map on the anterior (horn) and posterior part of the PZ. Textural (TexRAD®) parameter differences between TZ and PZ ROIs on T_2 weighted images were analyzed by linear regression. Results were correlated

with age (distributed into five decades from 22 to 89 years).

Results: Age was positively correlated with PSA level and glandular volumes (WG, TZ, and TZ/WG ratio; $p < 0.0001$) and was negatively correlated with AFSM and PPVP thickness ($p < 0.0001$). There was a positive correlation between ADC values of the PZ and age ($p = 0.003$) and between entropy of the TZ and PZ and age ($p < 0.001$).

Conclusion: Gradual variations in morphologic and textural features of the prostate were observed with age, mainly due to the increase in TZ volume while PZ volume tended to decrease. These modifications resulted in textural changes mainly at the expense of entropy.

Advances in knowledge: Entropy could be relevant for studying the process of aging of the prostate.

INTRODUCTION

MRI is the reference for detecting and localizing prostate cancer[1,18–20] Prostate MRI interpretation depends on zonal anatomy; whether lesion are located in the peripheral or in the transitional zone.[2–4] Given the importance of zonal anatomy for prostate MRI interpretation, knowledge of age-related morphologic changes is essential. Currently, the most commonly used nomenclature to describe prostatic structures and morphologic and pathologic changes related to the age of the human prostate is McNeal's zonal anatomy classification.[5] McNeal divided the prostate into four histologically distinct areas: a non-glandular anterior fibromuscular stroma (AFMS), two glandular regions termed peripheral (PZ) and central zones (CZ), and an

additional glandular region that surrounded the prostatic urethra, referred to as the transition zone (TZ). Some data have been published on the changes seen by MRI during prostatic ageing, including an increase in prostate volume, morphologic distortion of the prostatic edges, and signal intensity modifications related to age.[6–8] However, none of these studies have evaluated the relationship between morphological changes and textural analysis of prostate parenchyma.

Textural analysis is a novel imaging analysis technique that can quantify image heterogeneity resulting from changes not appreciated by the human eye. We hypothesized that complex morphologic changes in the prostate gland during

normal development may be associated with textural changes, and that texture analysis tools could refine our comprehension of morphologic changes related to age.

The aim of this study was to evaluate the impact of age on the zonal anatomy of the prostate on MRI, combining morphometric and textural analysis.

Subjects and methods

Study population

Our institutional radiology database was reviewed retrospectively to identify patients who underwent prostate MRI at our institution between August 2017 and December 2019 for clinical suspicion of prostate cancer. Patients were randomly selected from our database in order to have a homogeneous distribution by age group. Patients with proven prostate cancer were excluded from the study as were patients with PI-RADS 4 and 5 on MRI. A total of 154 patients was included and grouped by age in decades: Group 1, < 50-years-old ($n = 38$); Group 2, 50–59-years-old ($n = 31$); Group 3, 60–69-years-old ($n = 30$); Group 4, 70–79-years-old ($n = 29$); Group 5, > 79-years-old ($n = 26$). This study was approved by the local ethics committee.

MRI PROTOCOL

All images were acquired with a 3 Tesla MR imaging system (Siemens Healthcare, Erlangen, Germany) using a 32-channel phased-array torso coil according to a standardized protocol in which: (i) the patients were all advised to perform bowel preparation before the exam and to empty their bladder; (ii) 1 mg glucagon was administered intravenously to reduce peristaltic motion.

The standardized protocol (Table 1) performed in all examinations included a three-dimensional T_2 weighted image, axial diffusion-weighted image (DWI) of the prostate using b-values of 100, 500, 1000, and 2000 s/mm^2 with inline reconstruction of calculated DWI images (3000 s/mm^2) and apparent diffusion coefficient (ADC) map.

Dynamic contrast-enhanced imaging of the prostate was always obtained using a 3D fat-suppressed T_1 weighted gradient echo sequence with a temporal resolution of 10 sec after an intravenous bolus injection of 0.2 mL/kg of gadoterate meglumine (Dotarem, Guerbet). Delayed post-contrast fat-suppressed T_1 weighted imaging of the pelvis was also performed for nodal work-up.

IMAGE ANALYSIS

All measurements were performed retrospectively by one observer on images displayed on our standard review console. T_2 weighted images were evaluated with respect to prostatic zonal volumes: whole-gland (WG), TZ, and PZ volumes. On each examination, the prostate zonal volumes were calculated with the elliptical formula, length * width * height* 0.52. Length was defined as the greatest longitudinal distance on a mid-sagittal image, and width and height as the largest transverse and antero posterior distance on axial images. The reader was blinded from the PSA level and patient age. Measurements of the WG and TZ were made on the same images to calculate the TZ/WG ratio. Maximum measurable thickness at any level of the AFMS and periprostatic venous plexus (PPVP) was recorded as shown on Figure 1a. Regions of interest (ROIs) were drawn on the ADC map first on the anterior part (horn) and secondly in the posterior part of the PZ in order to keep the same size for both.

MRI textural analysis: quantitative analysis

Axial T_2 weighted images were analyzed using dedicated software for textural analysis (TexRAD Ltd, Feedback Plc, Cambridge, UK). Two identical ROIs were drawn by one observer in the PZ and TZ. The ROIs were placed in an area of normal appearing PZ and TZ signal. A suspicious lesion was defined as a focal increase

Table 1. ESUR recommendation-compliant description of multiparametric MRI protocol

		3-Tesla MRI	
	T_2 weighted **three-dimensional**	**Diffusion-weighted imaging**	**VIBE dynamic contrast enhanced imaging**
Section thickness/gap (mm)	0.85/0	4/1.2	3/0.6
Phase-encoding direction	Right-left	Anteroposterior	Anteroposterior
Repetition time (ms)	1550	6100	5,70
Echo time (ms)	173	64	2,66
Field of view	230 × 184	250 × 240	200 × 138
Acquisition matrix	320 × 288	108 × 108	256 × 179
b values (s/mm^2)		50, 500, 1000	
No. of repetitions	1,4	6, 9, 23	1
Turbo factor	24		
Acquisition duration	5 min 35 s	4 min 3 s	1 min 23 s
Flip angle (degrees)	115	90	10

All patients received 1 mg glucagon intravenously. No endorectal coil was used. VIBE: volumetric interpolated breath-hold examination.

Figure 1. a: Measurement method: maximal thickness of AFMS (blue line) and PPVP (red line) on axial T2-weighted image. b: bis. Changes in clinical and morphologic data with ranges of age.
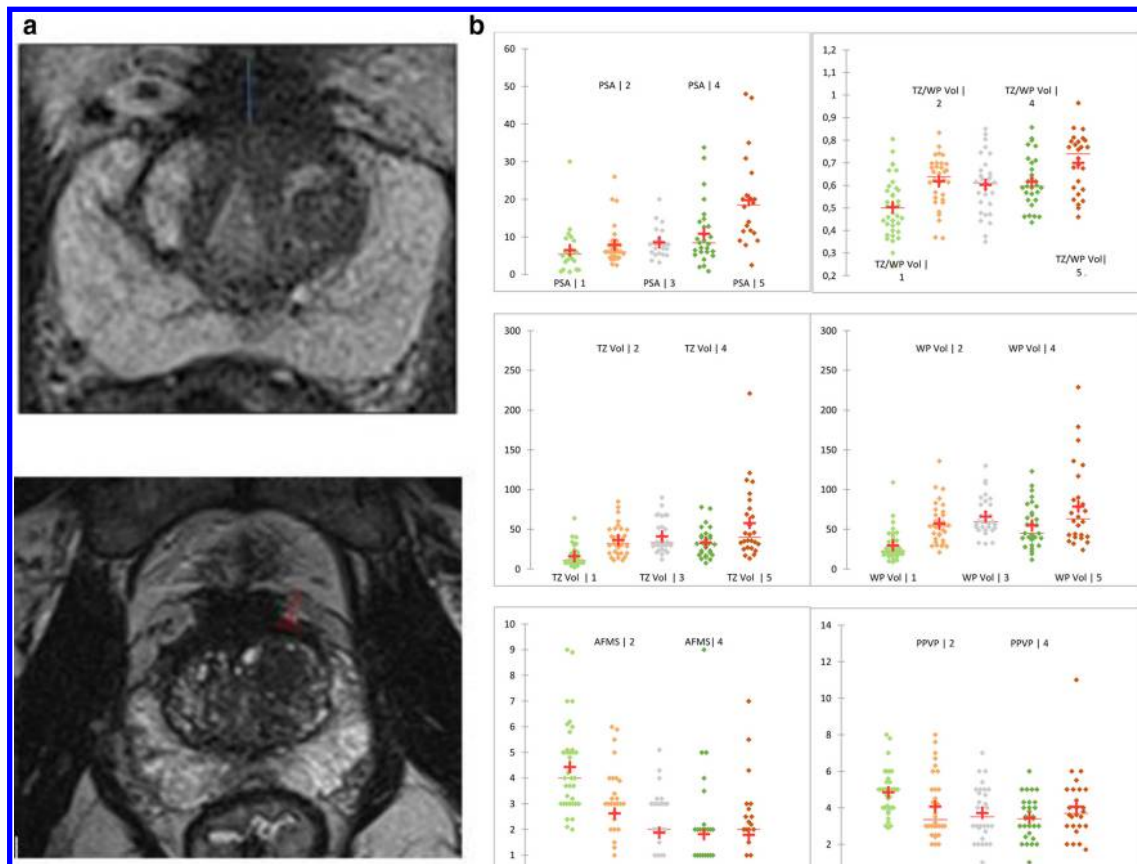
in signal intensity within the PZ on DWI images or decreased voxel values on the ADC map, or a lenticular, homogeneous, moderately hypointense focal lesion on T_2W in the TZ.

MRI textural analysis comprised image histogram analysis to quantify first-order statistics of mean, standard deviation (SD), entropy, mean of positive pixels, skewness, kurtosis, and sigma of the PZ and TZ ROIs. These parameters reflect, to varying extents, the number, intensity, and variability of areas of high and low signal intensity within the PZ and TZ.

STATISTICAL ANALYSIS

Frequentist inference was performed to describe the distribution of variables. Associations between each MRI variable and age as continuous variable were assessed by Pearson's correlation. MRI variables distribution was also determined after discretization by decade (<50-years-old, 50-59 years; 60-69 years; 79-80 years; >80 years).

A supervised machine learning algorithm using Bayesian inference (Markov Blanket which is particularly helpful when there is a large number of variables in a data set) was also used to analyze the probability distribution and importance (mutual information). To evaluate overfit evidence (G-test) was performed between MRI variables which are discretized automatically by computing with the Tree algorithm (the main reason for discretizing continuous variables is the advanced capability of the model

to capture more complex non-linear relationships between the variables) and age distribution classified manually by decades (<50-years-old, 50-59 years; 60-69 years; 79-80 years; >80 years). To visualize how MRI patterns change with age, direct effects analysis were performed from supervised Bayesian network and are presented in Figures 2 and 3. Direct effects measure the sensitivity of one variable to changes in another, analyzing both linear and non-linear dependencies. It also provides a ranking of input variables based on their relative contributions mutual dependence (Mutual information) of the evaluated results. It is typically used to rank the significant factors contributing to risk. Direct effects are calculated from the percentage change (d) in age (mean value) divided by the percentage change in each inputted variable according to formula: Direct effect $D_e x$ = dy/dx. So, in -axis represents the age and in x-axis, computed MRI patterns normalized variables to scale 0–100 to make them comparable. Mean values for MRI patterns (variables) are standardized between 0 and 100. The analysis was performed by using "soft evidence" feature, which gives virtual decimal values between actual values. The Mean m is computed using the numerical values (c) of the distribution states (according to discretization) and the marginal probability distribution (p) of the States: $m=\sum p*c$.

XLSTAT-Biomed (Addinsoft, Paris, France) and BayesiaLab 9.1 (Bayesia S.A.S, Change, France) software were used for the statistical analyses.

Figure 2. Relationship between age (<50-years-old, 50–59-years; 60–69-years; 79–80-years; >80-years). and MRI variables (ADC and AFMS) normalized on probability distribution means
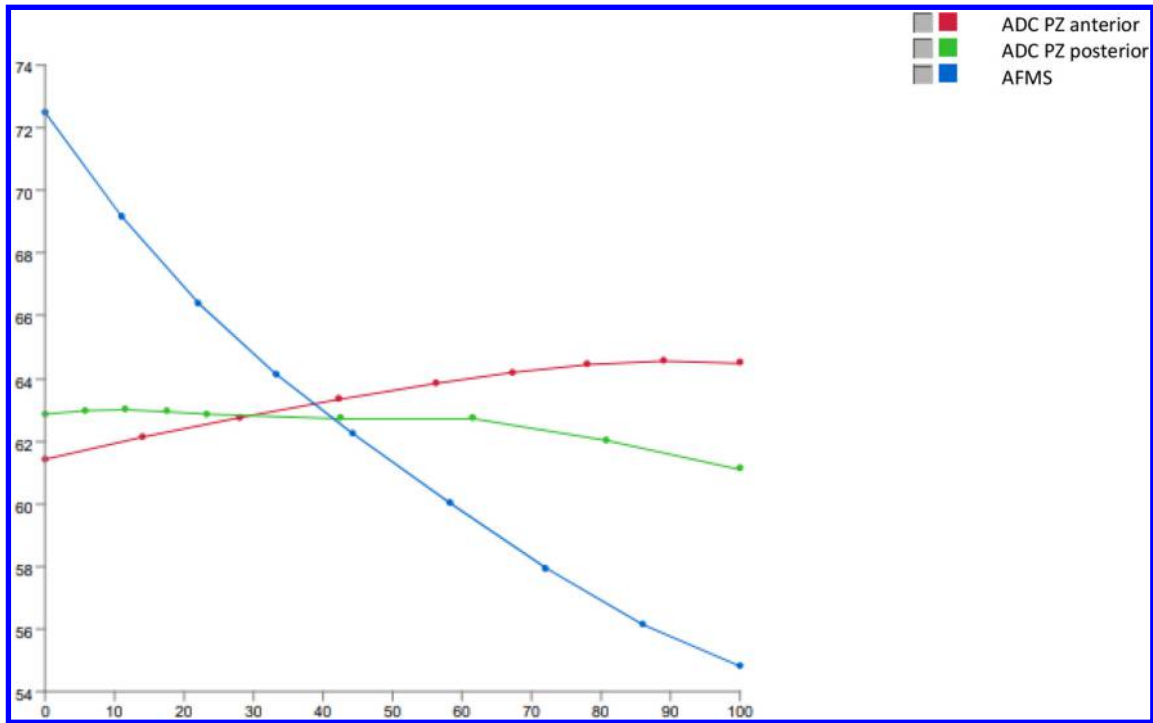

Figure 3. Relationship between age (<50-years-old, 50–59-years; 60–69-years; 79–80-years; >80-years). and MRI variables (entropy and sigma) normalized on probability distribution means
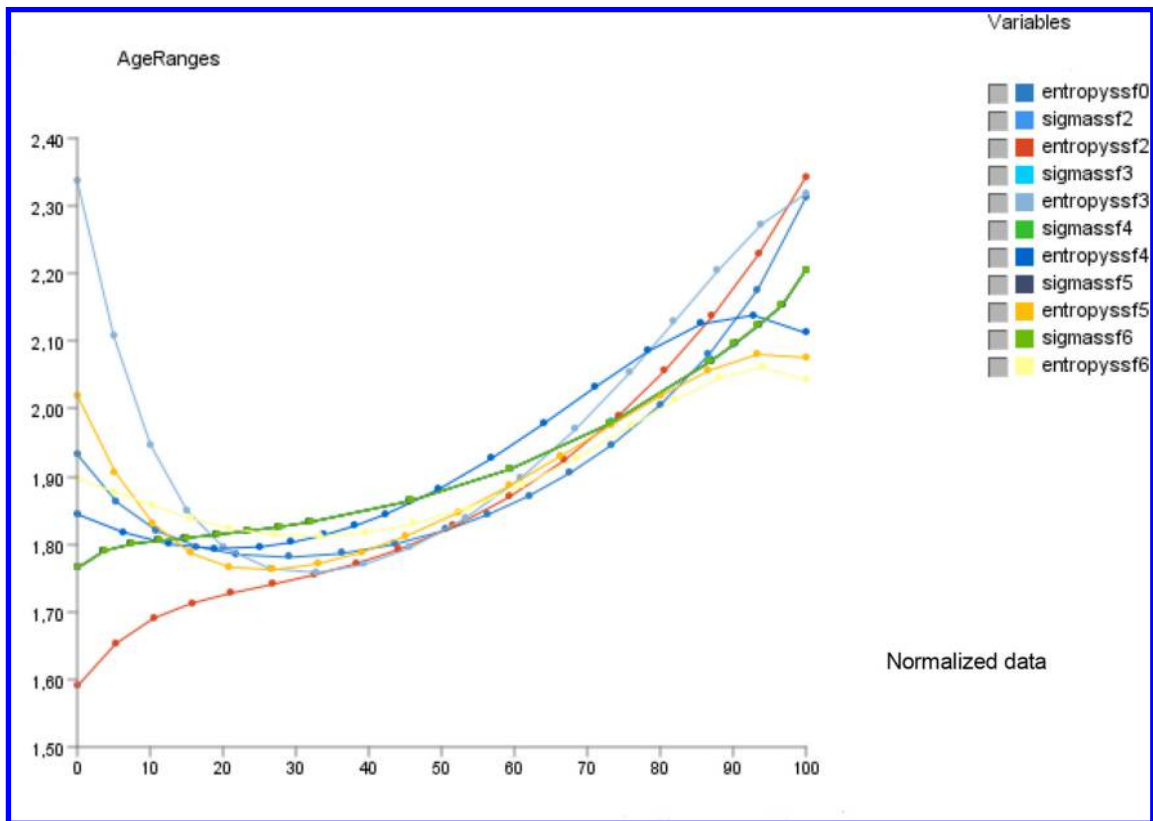
Table 2. Demographic, biologic, and morphologic data for the study population (N = 154)

Characteristic	
Age Mean ± SD Range (min–max) Median [IQR: first–third] Variance	63.0 ± 14.4 (22.0–88.0) 62.6 [53.2–74.0] 208.9
BMI Mean ± SD Range (min–max) Median [IQR: first–third] Variance	25.2 ± 3.9 (18.6–38.6) 24.9 [23.2–26.4] 15.4
PSA (ng/ml) Mean ± SD Range (min–max) Median [IQR: first–third] Variance	10.3 ± 8.6 (0.7–48.0) 7.8 [5.2–12.0] 74.5
TZ/WG ratio Mean ± SD Range (min–max) Median [IQR: first–third] Variance	0.6 ± 0.1 (0.2–0.9) 0.6 [0.5–0.7] 0
TZ volume (cc) Mean ± SD Range (min–max) Median [IQR: first–third] Variance	35.5 ± 27.8 (2.2–221.0) 30.0 [17.9–43.5] 775.3
WG volume (cc) Mean ± SD Range (min–max) Median [IQR: first–third] Variance	55.5 ± 34.3 (9.0–229.0) 49.0 [32.0–69.9] 1177.4
AFMS (mm) Mean ± SD Range (min–max) Median [IQR: first–third] Variance	2.6 ± 2.0 (0–9.0) 2.4 [1.0–3.8] 4.1
PPVP (mm) Mean ± SD Range (min–max) Median [IQR: first–third] Variance	4.0 ± 1.5 (1.0–11.0) 4.0 [3.0–5.0] 2.4
PZ ADC (anterior part) (mm^2/s) Mean ± SD Range (min–max) Median [IQR: first–third] Variance	1652.3 ± 385.9 (875.0–3254.0) 1640.0 [1352.0–1930.0] 148 985.4

BMI: body mass index; PSA: prostate-specific antigen; TZ: transitional zone; WG: whole gland; PZ: peripheral zone; AFMS: anterior fibromuscular stroma; PPVP: peri-prostatic venous plexus; ADC: apparent diffusion coefficient; ant: anterior; post: posterior.

RESULTS

Patients and demographic data

The demographic, biologic and morphologic data for the patients are summarized in Table 2. Mean patient age was 63 years (median: 62.5, range: 22–88 years), mean BMI was 25 (median: 25, range: 18.6–38.6), and mean PSA level was 10 ng ml^{-1} (median: 7.8, range: 0.7–48).

Mean WG, TZ, and PZ (=WG TZ) volumes were 55.5 ml (median: 49, range 9–229), 35.5 ml (median: 30, range 3–221 ml) and 20 ml (median: 16.9, range, 4–75 ml), respectively.

Mean WG volume was 29 ml for males aged <50 years (n = 37), 57 ml for males aged 50–59 years (n = 57), 66 ml for males aged 60–69 years (n = 30), 55 ml for males aged 70–79 years, and 79 ml for males aged >80 years (n = 29).

Mean TZ volume was 16 ml for males aged <50 years, 36 ml for males aged 50–59 years, 41 ml for males aged 60–69 years, 33 ml for males aged 70–79 years, and 58 ml for males aged >80 years.

Mean size of the AFMS and PPVP was 2.6 mm (median: 2.45, range: 1–9), and 4 mm (median: 4, range: 1–11), respectively.

Correlation between clinical and morphologic parameters and age

Age was positively correlated with serum PSA level, WG, and TZ volumes ($p < 0.0001$) (Figure 1b). In contrast, age was negatively correlated with AFMS thickness Figure 1b) and PPVP diameter ($p < 0.0001$ and $p < 0.002$)) (Table 3).

ADC values and textural metrics

Mean ADC values of PZ and TZ ROIs were 1666 mm^2/s (min–max: 813-4306) and 1652 mm^2/s (min–max: 875-3254), respectively. There was a positive correlation between ADC value of PZ and age ($p < 0.0001$) (Table 3, Figure 3).

There were significant positive correlations between entropy in the TZ and age at all filter values (SSF: 0, 2, 3, 4, 5, 6; $p < 0.001$) (Table 4, Figures 3 and 5), between age and sigma in the PZ and TZ ($p < 0.001$) (SSF: 2, 3, 4, 5, 6, and 2, 3, 4, 5, 6), and between entropy of the PZ and TZ/WG ratio (SSF 2, 4, 5). Entropy over time showed a peak in the fifth and sixth decades at all filter values (Figure 5, Figure 6).

Bayesian inference was used to explore conditional dependence relationships between age and MRI variables.

The relationship between age and MRI variable normalized probability distribution means are presented in Figure 5.

The supervised learning algorithm applied was the Markov Blanket learning algorithm. This algorithm restricts the selection of nodes to nodes belonging to the target node's fathers, sons, and spouses.[9]

DISCUSSION

We found, in this study, a gradual variations in morphologic and textural features with age.

Textural feature analysis depicted variations in entropy with respect to age and prostate gland volume. A strong correlation was found between entropy of the TZ and age at all filters ($p < 0.00001$), and between entropy of the PZ and TZ/WG ratio. Entropy is a measure of image "irregularity". An increase in entropy value indicates non-uniformity of the PZ and the TZ increasing with age and prostate volume under normal conditions. Different growth characteristics in each prostate zone may contribute to differences in the overall growth rate with age.[10] These changes that occur over time in the prostate gland

Table 3. Correlation coefficients for clinical and morphological data with age

Variable	Age	BMI	PSA	TZ/WG	TZ	WG	AFMS	PPVP	ADC-ant	ADC-post
Age	1	**0.033**	**0.369**	**0.470**	**0.414**	**0.406**	−0.047	−0.245	**0.235**	0.076
BMI	0.033	1	0.092	0.031	0.045	0.028	0.066	0.006	0.015	−0.014
PSA	**0.369**	0.092	1	**0.256**	**0.254**	**0.221**	−0.153	−0.107	−0.003	−0.052
TZ/WG	**0.470**	0.031	**0.256**	1	**0.630**	**0.452**	−0.428	−0.049	0.134	0.081
TZ	**0.414**	0.045	**0.254**	**0.630**	1	**0.951**	−0.517	**0.223**	**0.223**	0.087
WG	**0.406**	0.028	**0.221**	**0.452**	**0.951**	1	−0.522	**0.184**	**0.284**	0.117
AFMS	**0.477**	0.066	0.153	−0.428	−0.517	−0.522	1	0.057	−0.273	−0.105
PPVP	**0.245**	0.006	0.107	−0.049	**0.223**	**0.184**	0.057	1	−0.052	−0.095
ADC-ant	**0.235**	0.015	0.003	0.134	**0.223**	**0.284**	−0.273	−0.052	1	**0.547**
ADC-post	0.076	0.014	0.052	0.081	0.087	0.117	−0.105	−0.095	**0.547**	1

BMI: body mass index (kg/m²); PSA: prostate-specific antigen (ng/ml); TZ: transitional zone (ml); WG: whole gland (ml); AFMS: anterior fibromuscular stroma (mm); PPVP: peri-prostatic venous plexus (mm); ADC: apparent diffusion coefficient (mm²/s); ant: anterior; **Bold data indicate correlations that are significant (**p **value < 0.05)**

have been described by Mc Neal et al.[5] In the TZ, two distinct stages have been described: first the development and increase in number of nodules in the glandular tissue from the fourth decade into the 60 s, and then an abrupt increase in the mass of individual nodules.[10] Inversely, PZ is compressed by the increase in size of the TZ, with entropy in this area highly correlated with the TZ/WG ratio. All these structural changes may explain the positive correlation between entropy and age with a peak obtained during the fifth and the sixth decade.

We also observed a strong correlation between increasing PZ ADC values and age. De-Visshere et al[11] noticed that cystic atrophy of large glands occurred predominantly in older males. Because the water content of these large glands is higher than in pure normal glands it could explain the increase in ADC values of the PZ with age.

Most of available studies about textural analysis in prostate MRI concern prostate cancer detection and risk stratification. Wibmer et al[12] found in their study that Haralick texture features derived from T_2 weighted images and ADC maps have the potential to differentiate between prostate cancer and non-cancerous prostate tissue and that ADC map textural features correlated significantly with gleason score (GS). Nketiah et al[13] found that T_2W MRI derived textural features correlate significantly with GS. In this study, entropy was found to correlate significantly with

GS, possibly explained by the increase complexity of the tissue secondarily to glandular structure deformation.

Few studies have evaluated the changes in textural features in non-pathologic states and none in prostate imaging. In their study, Kalpana et al[14] correlated MRI features of brain white matter in normal subjects and those of HIV+ patients using a computational approach. They found that in non-pathologic states changes (either decrease or increase) in textural features (Haralick's parameter) may occur between 9 and 50 years of age and could be explained by changes in the architecture of the white mater.

Unlike many other organs that exhibit atrophy with age, prostate volume increases with age,.[10] In this study, values of 29 ml were being found for males aged <50 years to 79 ml for males > 80 years. This increase in size was highly correlated with the increase in TZ volume and TZ/PZ ratio. Knowledge of these morphologic changes on MRI will give us a better understanding of the meaning of variations in signal essential to improve the quality of reporting. In a previous study of 500 patients, Turkbey et al found that the WG volume peak was in the sixth and seventh decades of life and was mainly driven by changes in the TZ volume.[7] Our results are similar with a peak in Group 3 (sixth and seventh decades). However, we found that the maximum volume was obtained in the last decade (Group 5, > 80 years).

Figure 4. AFMS thickness decreased significantly with age (p<0.0001); MRIs from groups 1, 2, and 3, respectively
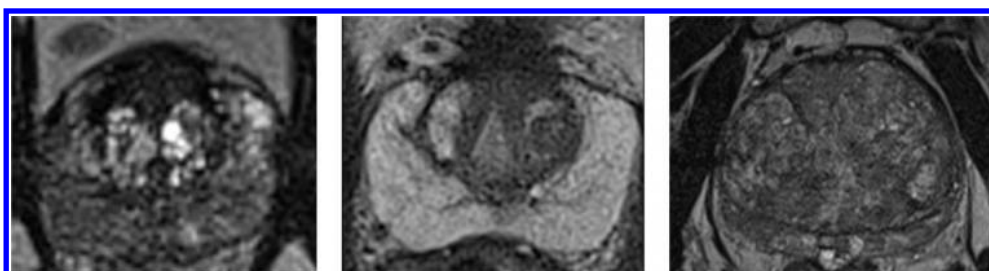
Table 4. Summary of significant associations between texture features and MRI according to age and prostate volume

Filter size (mm)	MRI features	Textural parameter	*p* value
2	PZ ROI and age	Sigma	0.00001
2	PZ ROI and age	Entropy	0.00014
2	PZ ROI and TZ/WG	Entropy	0.034355
2	TZ ROI and TZ/WG	Entropy	0.000293
3	PZ ROI and age	Sigma	0.000010
3	TZ ROI and age	Entropy	0.000010
3	TZ ROI and TZ/WG	Entropy	0.000008
4	PZ ROI and age	Sigma	0.000010
4	TZ ROI and age	Entropy	0.000020
4	PZ ROI and TZ/WG	Entropy	0.031047
4	TZ ROI and TZ/WG	Entropy	0.000043
5	PZ ROI and age	Sigma	0.000010
5	TZ ROI and TZ/WG	Entropy	0.044130
5	TZ ROI and age	Entropy	0.002328
5	PZ ROI and TZ/WG	Entropy	0.04413
5	TZ ROI and TZ/WG	Entropy	0.006224
6	PZ ROI and age	Sigma	0.000010
6	TZ ROI and age	Entropy	0.001963

PZ: peripheral zone; TZ: transitional zone; WG: whole gland; ROI: region of interest.

Figure 5. Evolution of transitional zone entropy with age (<50-years-old, 50–59-years; 60–69-years; 79–80-years; >80-years).

Figure 6. Mean and median values (and interquartile range 25 %-75%) for entropy at all filter according to age.

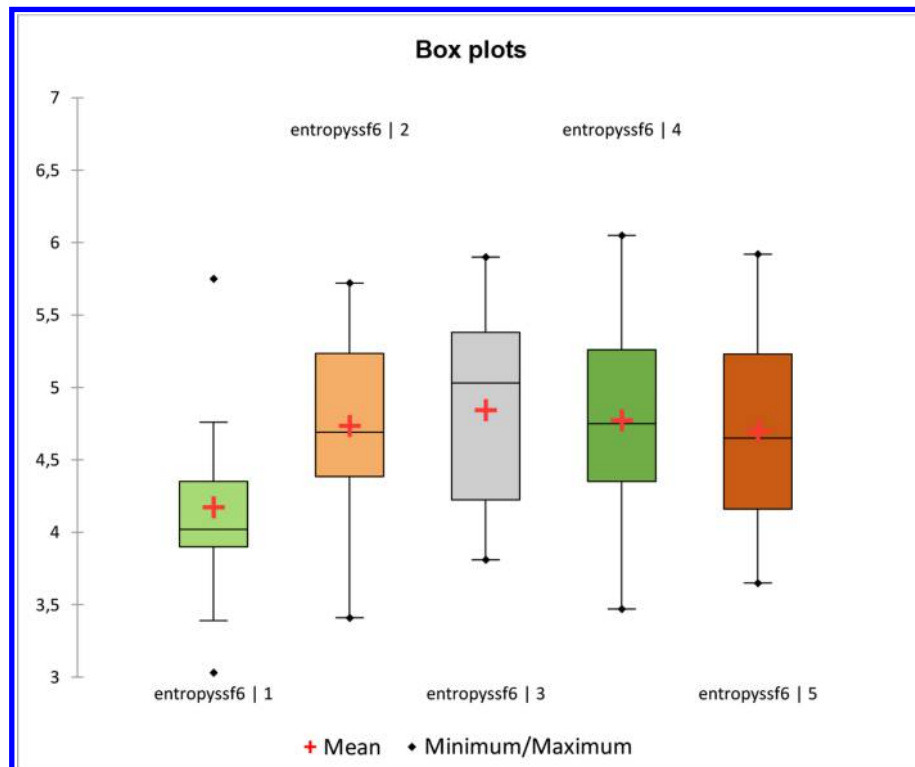| Statistique RO1	entropyssf0 | Age-C	entropyssf0 | Age-D	entropyssf2 | Age-C	entropyssf2 | Age-D	entropyssf4 | Age-C	entropyssf4 | Age-D	entropyssf6 | Age-C	entropyssf6 | Age-D	
Nb. d'observ	31	30	31	30	31	30	33	30	
1er Quartile	4,370	4,143	4,580	4,345	4,525	4,293	3,780	3,948	
Médiane	4,470	4,840	5,060	5,200	4,860	5,160	4,470	4,230	
3ème Quarti	5,000	5,083	5,395	5,520	5,225	5,398	4,790	4,678	
Moyenne	4,609	4,649	5,005	5,002	4,871	4,927	4,350	4,304	
Variance (n-)	0,179	0,308	0,303	0,413	0,280	0,434	0,319	0,293	
Ecart-type (n	0,423	0,555	0,551	0,643	0,529	0,658	0,565	0,541	
supplementary Table.									
Mean and median values (and interquartile range 25 %-75%) for entropy at all filter according to age (C 50-60, D 60 -70 yo)									

This difference may be due to a difference in sampling in groups; median age in the study of Turkbey et al was 60 years (range: 38–83 years), whereas it was 62.5 years in our study (range: 22–88 years). In addition, PZ volume decreased with age and in parallel with the increase in TZ volume. In a retrospective study, Matsugasumi et al[8] evaluated the relationship between morphology of the PZ and age in a cohort of 307 men (156 from Japan). The authors found that as the TZ increases in size the PZ becomes thinner as part of the stretched surgical capsule.

As described previously,[7,15] we also found a positive correlation between serum PSA level, WG ($p = 0.006$) and TZ volume ($p = 0.002$). These findings are consistent with the concept that the TZ, which consists of a mixture of stromal and glandular hyperplasia developed in response to testosterone, is the principal determinant factor in benign prostatic hyperplasia and elevated serum PSA levels.[16]

Because prostate cancer could extend in the AFMS, knowledge of its anatomy and evolution with age is important. The AFMS has low signal intensity on T_2W and forms the entire anterior and convex surface of the prostate as a thick apron, extending from the bladder neck to the prostate apex. Like Hricak et al,[17] we found that the thickness of the AFMS decreases proportionally with the increase in TZ, possibly due to compression or stretching by the enlarged gland. The AFMS was most prominent in young patients with small prostate glands (4.4 mm in Group 1 *vs* 1.8 mm in Group 5).

The PPVP, which had a round, tubular structure on anterior and lateral aspects of the prostate, was generally prominent in young patients with small glands and became thinner with increasing age. Although this phenomenon may be due to venous compression by gland enlargement, the inverse correlation of venous caliber to patient age was much greater than the inverse correlation of venous caliber to gland size. These results are concordant with those of Allen et al.[6]

The present study has some limitations. Morphometric analyses of prostate volume were done by one reader only. We did not monitor the longitudinal changes in zonal volume in our cohort or correlate morphologic changes with the International Prostate Symptom Score. Our results may be related to true anatomic differences in the prostate gland with age, as reflected in their parenchymal patterns, although other biological factors may be involved such as biochemical differences due to inflammatory or hormonal changes, unfortunately we could not have access to biological data as testoteronemia. The relationships between textural features and tissue composition (cytoplasm, stroma, luminal space) need to be explored with histopathological correlations.

CONCLUSION

Knowledge of the anatomic modifications of the prostate gland with age is a prerequisite to interpreting prostate MRIs. The results of this study show gradual variations in morphologic and textural features with age, mainly due to the increase in TZ volume, while the PZ tends to decrease. These modifications resulted in textural changes mainly at the expense of entropy.

FUNDING

REFERENCES

1. Ahmed HU, El-Shater Bosaily A, Brown LC, Gabe R, Kaplan R, Parmar MK, et al. Diagnostic accuracy of multi-parametric MRI and TRUS biopsy in prostate cancer (PROMIS): a paired validating confirmatory study. *Lancet* 2017; **389**: 815–22. doi: https://doi.org/10.1016/S0140-6736(16)32401-1

2. Dickinson L, Ahmed HU, Allen C, Barentsz JO, Carey B, Futterer JJ, et al. Magnetic resonance imaging for the detection, localisation, and characterisation of prostate cancer: recommendations from a European consensus meeting. *Eur Urol* 2011; **59**: 477–94. doi: https://doi.org/10.1016/j.eururo.2010.12.009

3. Weinreb JC, Barentsz JO, Choyke PL, Cornud F, Haider MA, Macura KJ, et al. PI-RADS prostate imaging - reporting and data system: 2015, version 2. *Eur Urol* 2016; **69**: 16–40. doi: https://doi.org/10.1016/j.eururo.2015.08.052

4. Turkbey B, Rosenkrantz AB, Haider MA, Padhani AR, Villeirs G, Macura KJ, et al. Prostate imaging reporting and data system version 2.1: 2019 update of prostate imaging reporting and data system version 2. *Eur Urol* 2019; **76**: 340–51. doi: https://doi.org/10.1016/j.eururo.2019.02.033

5. McNeal JE. Regional morphology and pathology of the prostate. *Am J Clin Pathol* 1968; **49**: 347–57. doi: https://doi.org/10.1093/ajcp/49.3.347

6. Allen KS, Kressel HY, Arger PH, Pollack HM. Age-Related changes of the prostate: evaluation by MR imaging. *AJR Am J Roentgenol* 1989; **152**: 77–81. doi: https://doi.org/10.2214/ajr.152.1.77

7. Turkbey B, Huang R, Vourganti S, Trivedi H, Bernardo M, Yan P, et al. Age-Related changes in prostate zonal volumes as measured by high-resolution magnetic resonance imaging (MRI): a cross-sectional study in over 500 patients. *BJU Int* 2012; **110**: 1642–7. doi: https://doi.org/10.1111/j.1464-410X.2012.11469.x

8. Matsugasumi T, Fujihara A, Ushijima S, Kanazawa M, Yamada Y, Shiraishi T, et al. Morphometric analysis of prostate zonal anatomy using magnetic resonance imaging: impact on age-related changes in patients in Japan and the USA. *BJU Int* 2017; **120**: 497–504. doi: https://doi.org/10.1111/bju.13823

9. Conrady S, Jouffe L. Bayesian Networks & BayesiaLab A Practical Introduction for Researchers. *Bayesia USA, 1st edition* 2015;.

10. McNeal JE. Origin and evolution of benign prostatic enlargement. *Invest Urol* 1978; **15**: 340–5.

11. De Visschere PJL, Vral A, Perletti G, Pattyn E, Praet M, Magri V, et al. Multiparametric magnetic resonance imaging characteristics of normal, benign and malignant conditions in the prostate. *Eur Radiol* 2017; **27**: 2095–109. doi: https://doi.org/10.1007/s00330-016-4479-z

12. Wibmer A, Hricak H, Gondo T, Matsumoto K, Veeraraghavan H, Fehr D, et al. Haralick texture analysis of prostate MRI: utility for differentiating non-cancerous prostate from prostate cancer and differentiating prostate cancers with different Gleason scores. *Eur Radiol* 2015; **25**: 2840–50. doi: https://doi.org/10.1007/s00330-015-3701-8

13. Nketiah G, Elschot M, Kim E, Teruel JR, Scheenen TW, Bathen TF, et al. T2-Weighted MRI-derived textural features reflect prostate cancer aggressiveness: preliminary results. *Eur Radiol* 2017; **27**: 3050–9. doi: https://doi.org/10.1007/s00330-016-4663-1

14. Kalpana R, Muttan S, Kumarasamy N. Virus infection on brain white matter: statistical analysis of dT MRI scans. *Int J Bioinform Res Appl* 2011; **7**: 273–86. doi: https://doi.org/10.1504/IJBRA.2011.041738

15. Berry SJ, Coffey DS, Walsh PC, Ewing LL. The development of human benign prostatic hyperplasia with age. *J Urol* 1984; **132**: 474–9. doi: https://doi.org/10.1016/S0022-5347(17)49698-4

16. Stamey TA, Yang N, Hay AR, McNeal JE, Freiha FS, Redwine E. Prostate-Specific antigen as a serum marker for adenocarcinoma of the prostate. *N Engl J Med* 1987; **317**: 909–16. doi: https://doi.org/10.1056/NEJM198710083171501

17. Hricak H, Dooms GC, McNeal JE, Mark AS, Marotti M, Avallone A, et al. Mr imaging of the prostate gland: normal anatomy. *AJR Am J Roentgenol* 1987; **148**: 51–8. doi: https://doi.org/10.2214/ajr.148.1.51

18. van der Leest M, Cornel E, Israël B, Hendriks R, Padhani AR, Hoogenboom M, et al. Head-To-Head comparison of transrectal ultrasound-guided prostate biopsy versus multiparametric prostate resonance imaging with subsequent magnetic resonance-guided biopsy in Biopsy-naïve men with elevated prostate-specific antigen: a large prospective multicenter clinical study. *Eur Urol* 2019; **75**: 570–8. doi: https://doi.org/10.1016/j.eururo.2018.11.023

19. Kasivisvanathan V, Rannikko AS, Borghi M, et al. MRI-targeted or standard biopsy for prostate-cancer diagnosis. *N Engl J Med* 1777; **2018**: 1767.

20. Rouvière O, Puech P, Renard-Penna R, Claudon M, Roy C, Mège-Lechevallier F, et al. Use of prostate systematic and targeted biopsy on the basis of multiparametric MRI in biopsy-naive patients (MRI-FIRST): a prospective, multicentre, paired diagnostic study. *Lancet Oncol* 2019; **20**: 100–9. doi: https://doi.org/10.1016/S1470-2045(18)30569-2

21. Loeb S, Kettermann A, Carter HB, Ferrucci L, Metter EJ, Walsh PC. Prostate volume changes over time: results from the Baltimore longitudinal study of aging. *J Urol* 2009; **182**: 1458–62. doi: https://doi.org/10.1016/j.juro.2009.06.047

FULL PAPER

Prognostic value of breast MRI characteristics before and during neoadjuvant endocrine therapy in patients with ER+/HER2- breast cancer

[1,2]MAX AA RAGUSI, MD, [1]GONNEKE AO WINTER-WARNARS, MD, PhD, [3]JELLE WESSELING, MD, PhD, [4]SABINE C LINN, MD, PhD, [1]REGINA G BEETS-TAN, MD, PhD, [2]BAS HM VAN DER VELDEN, PhD, [5]SJOERD G ELIAS, MD, PhD, [2]KENNETH GA GILHUIJS, PhD and [1]CLAUDETTE E LOO, MD, PhD

[1]Department of Radiology, The Netherlands Cancer Institute – Antoni van Leeuwenhoek Hospital, Amsterdam, The Netherlands
[2]Department of Radiology/Image Sciences Institute, University Medical Center Utrecht, Utrecht University, Utrecht, The Netherlands
[3]Department of Pathology, The Netherlands Cancer Institute – Antoni van Leeuwenhoek Hospital, Amsterdam, The Netherlands
[4]Department of Medical Oncology, The Netherlands Cancer Institute – Antoni van Leeuwenhoek Hospital, Amsterdam, The Netherlands
[5]Department of Epidemiology, Julius Center for Health Sciences and Primary Care, University Medical Center Utrecht, Utrecht University, Utrecht, The Netherlands

Address correspondence to: Mr Max AA Ragusi
E-mail: *m.a.a.ragusi-2@umcutrecht.nl*

Objective: To investigate whether BIRADS MRI characteristics before or during neoadjuvant endocrine therapy (NET) are associated with the preoperative endocrine prognostic index (PEPI) in ER+/HER2- breast cancer patients.

Methods: This retrospective observational cohort study included 35 ER+/HER2- patients with 38 tumors (3 bilateral cases) treated with NET. The pre- and midtreatment (after 3 months) MRIs were evaluated by two breast radiologists for BIRADS imaging characteristics, shrinkage pattern, and radiologic response. PEPI was used as end point. PEPI is based on the post-treatment surgical specimen's pT- and pN-stage, Ki67, and ER-status. Tumors were assigned PEPI-1 (good prognosis) or PEPI-2/3 (poor prognosis). We investigated whether pre- and midtreatment BIRADS characteristics were associated with PEPI.

Results: Median patient age was 65 years (interquartile interval [IQI]: 53, 70). 17 tumors (44.7%) were associated with good prognosis (PEPI-1), and 21 tumors (55.3%) with poor prognosis (PEPI-2/3). A larger reduction in tumor size after 3 months of NET was significantly associated with PEPI; 10 mm (IQI: 5, 13.5) in PEPI-1 tumors *vs* 4.5 mm (IQI: 3, 7; *p* = .045) in PEPI-2/3 tumors. Other BIRADS characteristics, shrinkage pattern or radiologic response were not associated with PEPI.

Conclusion: Only a larger reduction in tumor size on MRI after 3 months of NET was associated with PEPI-1 (good prognosis) in ER+/HER2- breast cancer patients.

Advances in knowledge: MRI characteristics previously reported to be associated with prognosis during neoadjuvant chemotherapy are not necessarily associated with prognosis during NET in ER+/HER2- breast cancer patients.

INTRODUCTION

Neoadjuvant treatment for patients with estrogen receptor-positive (ER+) human epidermal growth factor receptor 2-negative (HER2-) breast cancer includes neoadjuvant endocrine therapy (NET) and neoadjuvant chemotherapy (NAC). NET leads to similar rates of breast conserving surgery (BCS) and pathologic response rates compared to NAC in strong ER+ breast cancer patients.[1] However, NET has the advantage of being less toxic compared to NAC.[1]

About 50–70% of patients show a clinical response during NET.[2] In order to identify patients who will benefit from NET, it is important to monitor the tumor during treatment to allow for therapy adjustment, *e.g.* expediting surgery or switching treatment regimen. Response monitoring during neoadjuvant treatment is mostly done using MRI because it is the most sensitive modality to assess tumor response.[3] Many studies have identified MRI characteristics during NAC that are associated with tumor response and prognosis,[4–7] whereas studies investigating MRI during NET are limited.[8,9]

The performance of MRI to predict response after NAC differs among the different immunohistochemical

subtypes.[4,7] Especially predicting response in ER+/HER2- breast cancer has proven to be difficult.[4,7] For example, change in tumor size on MRI during NAC was associated with response in triple negative (TN) and HER2+ breast cancer, but was not associated with response or prognosis in ER+ breast cancer.[4,10] Changes in apparent diffusion coefficient (ADC),[6] and tumor shrinkage pattern during NAC, however, did show an association with tumor response in ER+/HER2- breast cancer.[5]

Pathologic complete response (pCR) is typically used as surrogate endpoint of survival in neoadjuvant studies. However, pCR might not be suited for ER+ breast cancer, because the rate of pCR is low (about 10%), and is poorly associated with prognosis.[11,12] This might also explain the relatively poor performance of MRI to predict response in ER+/HER2- breast cancer. The preoperative endocrine prognostic index (PEPI) was developed as a surrogate endpoint of survival for ER+/HER2- breast cancer after NET, and might better predict survival than pCR in this subset of patients. PEPI is derived from the histopathological evaluation after NET. Patients are stratified in three prognostic groups (PEPI-1, PEPI-2, and PEPI-3) based on pT- and pN-stage, the Ki67 index, and ER-status.[13,14] PEPI-1 is associated with the best prognosis, and PEPI-3 is associated with the poorest. Patients with a PEPI-1 after NET have such a favorable

prognosis that adjuvant endocrine monotherapy might suffice, whereas patients with a PEPI-2 or PEPI-3 should be recommended adjuvant chemotherapy.[13,14] Prediction of PEPI before or during NET could allow for therapy adjustments in patients who are predicted to have a poor prognosis after NET (*i.e.* PEPI-2 or PEPI-3).

The aim of this study was to investigate whether MRI characteristics before and during NET were associated with PEPI after NET. We have focused on those characteristics that were previously associated with response or prognosis in NAC, namely: Breast Imaging Reporting and Data System (BIRADS) MRI characteristics, diffusion-weighted imaging (DWI) findings, and radiologic response.

METHODS AND MATERIALS
Patients and treatment
This retrospective explorative observational cohort study was approved by the institutional review board of the Antoni van Leeuwenhoek Hospital and the requirement for informed consent was waived. All patients diagnosed with pathologically proven ER+/HER2- breast cancer treated with NET between January 2013 and December 2017 with available pretreatment

Figure 1. Flowchart of inclusion and available imaging. Flowchart of patient inclusion and availability of imaging sequences at the different timepoints. ER+, estrogen receptor-positive; HER-, human epidermal growth factor receptor 2-negative; NET, neoadjuvant endocrine therapy.

Available imaging	Pretreatment	Midtreatment
Contrast-enhanced	38 (100 %)	38 (100 %)
Kinetic analysis	29 (76.3 %)	36 (94.7 %)
Diffusion-weighted	29 (76.3%)	34 (94.4 %)
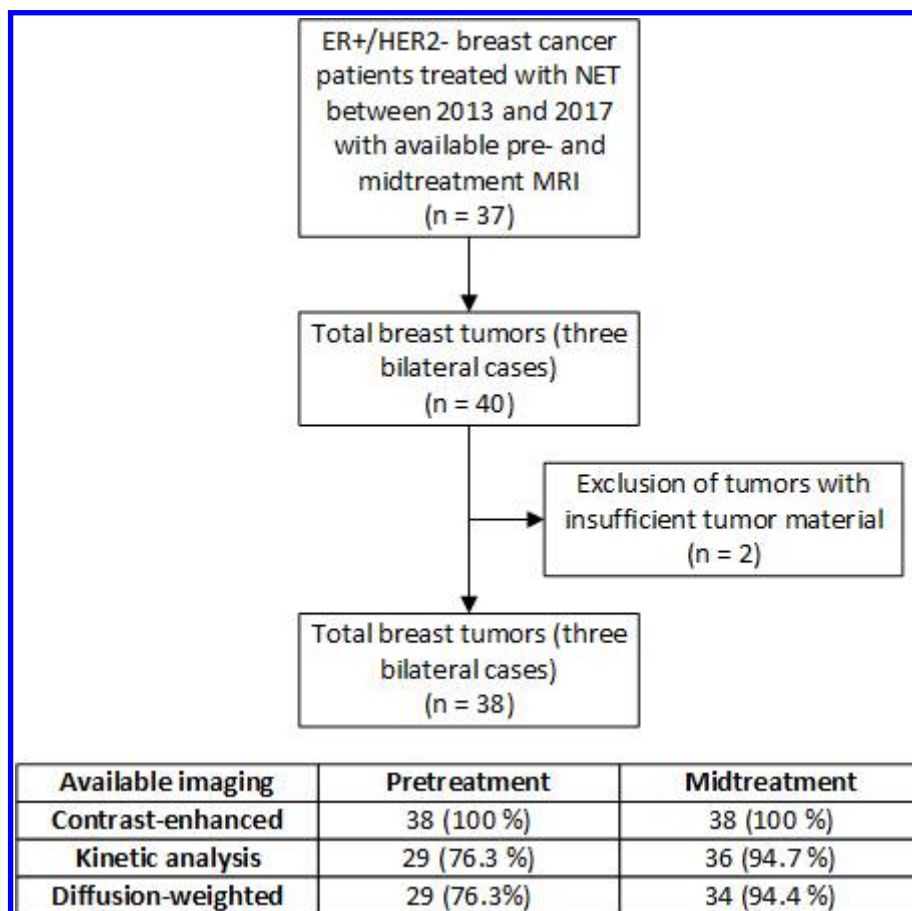
and midtreatment (after 3 months) MRI were consecutively included (*n* = 37; Figure 1). Three patients had a bilateral tumor. In total, 40 tumors were included in the study. NET was recommended to patients with strong ER+ (≥50 %) / HER2- tumors where BCS could not be performed or to reduce the risk of involved surgical margins [*e.g.* in the case of an invasive lobular carcinoma (ILC)]. Additionally, there should be no indication for NAC for these patients: the tumor is ≤30 mm and there is ≤1 suspicious lymph node in combination with a low risk Mammaprint 70-gene signature (Agendia, Amsterdam, The Netherlands). In case of excess comorbidity (*e.g.* in cases where NAC or primary surgery at that time is expected to put excessive strain on the patient), NET is also recommended. The decision for NET is made during a multidisciplinary meeting. Tamoxifen (for pre-menopausal patients), aromatase inhibitors (AIs, for post-menopausal patients), or a sequential combination of both agents was recommended for a duration of 6–9 months. A breast tissue marker was placed before start of treatment for future localization of the tumor.[7] The midtreatment response MRI is performed after 3 months of NET: in case of unfavorable tumor response (*i.e.* stable or progressive disease), surgery is expedited or the endocrine therapy is switched.

MRI technique

MRI was performed before start and after 3 months of NET and included axial DWI and dynamic contrast-enhanced (DCE) imaging with patients in prone position (Figure 1). MRI was performed on a 1.5 T or a 3 T imaging unit (Achieva, Philips, Best, The Netherlands) with a dedicated 7- or 16-element SENSE breast coil (Philips, Best, The Netherlands).

DWI was performed using *b* values of 0, and 800 s/mm^2; *b* values of 0, and 1000 s/mm^2; *b* values of 0, and 1200 s/mm^2; or *b* values of 0, 150, and 1500 s/mm^2. The following imaging parameters were used: ratio of repetition time/echo time 5500/71 or 7000/90, flip angle 90°, voxel sizes 0.90 × 0.90 × 5 mm^3 or 0.99 × 0.99 × 5 mm^3, and a field of view of 380 or 400 mm.

The DCE protocol consisted of an unenhanced three-dimensional T_1 weighted fast field echo sequence with fat suppression before intravenous injection of gadolinium-containing contrast (0.1 mmol/kg, Dotarem, Geurbet, Villepinte, France), followed by five consecutive series of dynamic post-contrast images at 60 or 90 s intervals. Two sets of imaging parameters were used: acquisition time 60 or 90 s, ratio of repetition time/echo time 4.3/1.8 or 3.7/1.9, flip angle 10°, voxel sizes 0.62 × 0.62 × 2.3 mm^3 or 0.89 × 0.89 × 1.8 mm^3, and a field of view of 400 mm (Supplementary Material 1). For nine patients, the pretreatment MRI was performed in the referring hospital.

MRI evaluation

Two dedicated breast radiologists (C.L. and G.W., with 18 and 30 years of experience) retrospectively reviewed the pre- and midtreatment MRIs. The radiologists independently interpreted the images and were blinded to the pathologic outcome. Only information regarding the laterality was made available in the case of bilateral tumors. Disagreements were overcome by reviewing the images in consensus.

The morphologic and kinetic features were evaluated according to the BIRADS.[15] The largest tumor in the breast was considered the index lesion. The size of the tumor was measured as its largest diameter in one of the three planes (sagittal, coronal, or axial) during initial enhancement (60–90 s post-contrast) and late enhancement (360–450 s post-contrast). In the case of a bilateral tumor, the index tumor of each breast was assessed independently. Kinetic features of the lesions were evaluated using DynaCAD (Invivo, Philips, Best, The Netherlands). After 3 months, the tumors were additionally evaluated on tumor shrinkage pattern, radiologic response, and the Response Evaluation Criteria in Solid Tumors (RECIST).[16] The shrinkage pattern classification was adapted from Fukada et al[5]; complete response (no visible tumor), concentric shrinkage; reduction of the largest diameter with disappearance of non-mass enhancement (residual foci of <5 mm were allowed), non-concentric shrinkage; if the shrinkage pattern couldn't be classified as concentric (*e.g.* decrease of intensity only, or diffuse decrease with non-mass enhancement), and stable or progressive growth (Figure 2).[5] The radiologic response was classified as; complete response (absence of pathological enhancement), partial response (partial disappearance of enhancement), and no response (stable or progressive disease). Lastly, the RECIST response categories included: disappearance of enhancing tumor was classified as complete response, ≥30% decrease in tumor size (initial enhancement) was classified as partial response, ≥20% increase in tumor size (initial enhancement) or the appearance of new lesions was classified as progressive disease, and if the shrinkage didn't qualify for partial nor progressive disease, the response was classified as stable disease.[16]

For the DWI assessment, the tumor was first identified on the DCE images and then localized on the DWI and the ADC maps. Both radiologists assessed the images for the presence of diffusion restriction in the tumor, which was defined as high signal intensity on the DWI combined with low signal intensity on the ADC maps.

Pathologic response assessment

PEPI was used as endpoint.[13,14] PEPI is derived from the surgical specimen after NET and is based on: pT- and pN-stage, Ki67, and ER-status. Tumors are assigned risk points (0–12) based on these characteristics. The risk points stratify patients in one of three prognostic groups: PEPI-1 (0 points), PEPI-2 (1–3 points), and PEPI-3 (3 or more points) with distinct prognosis.[13] It is proposed that patients with PEPI-1 have such a favorable prognosis after NET that monotherapy with adjuvant endocrine therapy can suffice after surgery, whereas adjuvant chemotherapy should be considered for PEPI-2 and PEPI-3.[13,14] As both PEPI-2 and PEPI-3 should be considered for adjuvant chemotherapy, the a-priori decision to analyze PEPI-1 *vs* PEPI-2/3 was made, a method that was also adopted by a recent publication on the validation of PEPI.[13] Two patients were excluded due to insufficient tumor material in the surgical specimen to assess PEPI (Figure 1).

Statistical analysis

Summary statistics are reported as median [interquartile interval (IQI)]. The inter-rater agreement for categorical variables was

Figure 2. Shrinkage pattern. Examples of a concentric shrinkage pattern (left column) and a non-concentric shrinkage pattern (right column). The tumor in the right column shows a diffuse decrease after 3 months of NET (a non-concentric shrinkage pattern). This patient also showed segmental enhancement in the lateral upper quadrant of the left breast. This proved to be a complex sclerosing lesion at biopsy. The definitions of shrinkage pattern were adapted from Fukada et al[5]. NET, neoadjuvant endocrine therapy.
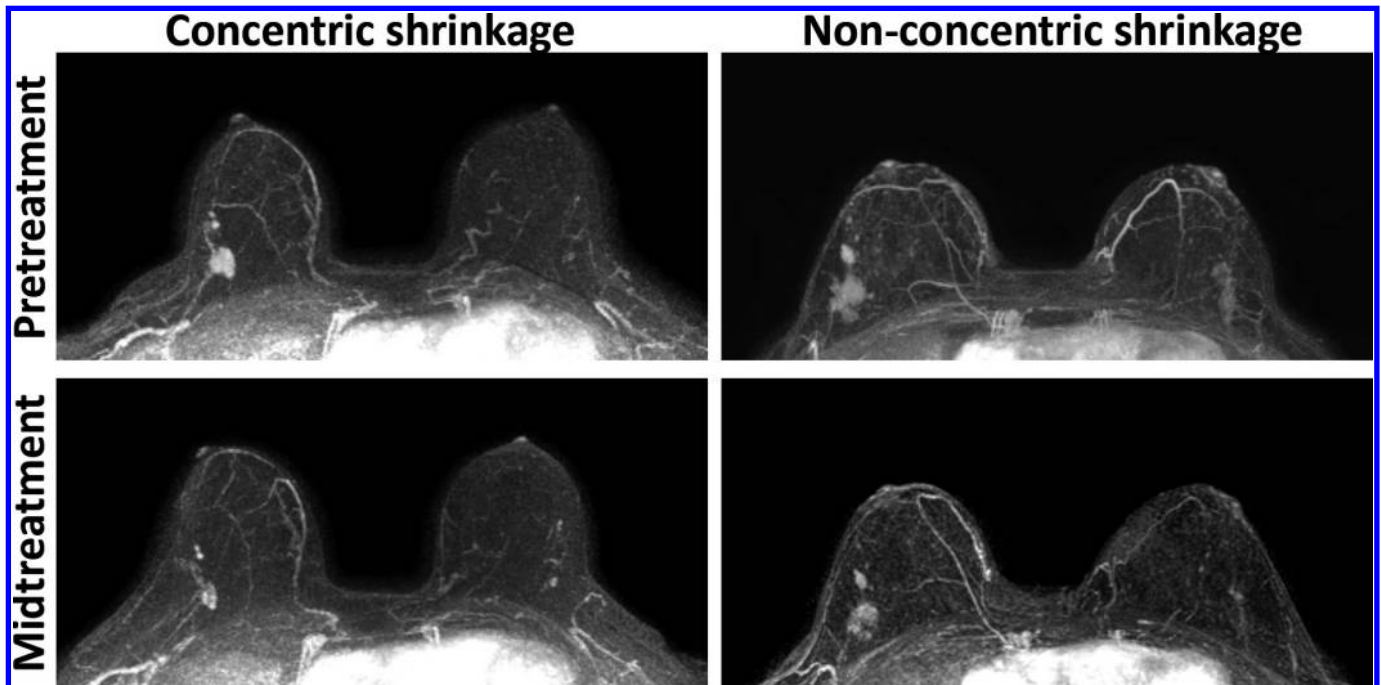
calculated using Cohen's κ. For continuous variables, the mean difference with limits of agreement, based on Bland–Altman analysis, and the intraclass correlation coefficient (ICC; two-way random-effects, absolute agreement, single rater) were calculated with 95% confidence intervals (95% CI).[17] Cohen's κ was interpreted as: <0, poor agreement; 0.01–0.20, slight agreement; 0.21–0.40, fair agreement; 0.41–0.60, moderate agreement; 0.61–0.80, substantial agreement; 0.81–1, almost perfect agreement[18]; and the ICC was interpreted as: <0.5, poor reliability; 0.5–0.75, moderate reliability; 0.75–0.9, good reliability; >0.9, excellent reliability.[17] The results after the consensus readings were used to investigate whether BIRADS characteristics on MRI before and after 3 months of NET were associated with the PEPI-groups. Statistical differences for categorical variables were calculated using Fisher's exact test, the Mann–Whitney *U* test for unpaired continuous variables, and the Wilcoxon signed-rank test for paired continuous variables. Statistical analyses were performed using R v. 4.0.2 (R Foundation for Statistical Computing, Vienna, Austria). A two-tailed *p* < .05 was considered to represent statistical significance.

RESULTS

Patient cohort

Table 1 summarizes patient, tumor, and treatment characteristics. The pre- and midtreatment MRI of 35 patients and 38 tumors (3 bilateral cases) were evaluated. The median age at diagnosis was 65 years (IQI: 53, 70). Clinical stage was mostly Stage I (26.3%) or II (60.5%), there was one clinical Stage 0 (ductal carcinoma *in situ* in a bilateral case) and four cases of clinical Stage III (10.5%). Pretreatment Ki67 was similar between the PEPI-groups.

Patients received NET for a median duration of 7.4 months (IQI: 6.6, 7.9), and BCS could be performed in 31 patients (81.6%). At histopathological evaluation 17 tumors (44.7%) were associated with a good prognosis, or PEPI-1, whereas 21 patients (55.3%) were associated with a relatively poor prognosis, or PEPI-2/3.

Inter-rater agreement

The inter-rater agreement for the BIRADS characteristics are summarized in Table 2. Most BIRADS characteristics show fair to moderate agreement, although the inter-rater agreement of the subclassifications for (non)mass shape and enhancement characteristics were poor. The mean inter-rater difference in pretreatment tumor size was −3.68 mm with limits of agreement between −27.7 mm and 20.3 mm, similarly, the mean difference in midtreatment tumor size was 0.3 mm with limits of agreement between −22.5 mm and 23.0 mm (Figure 3). Large disagreements in tumor size were in cases when the radiologists disagreed about the focality of the tumor (*i.e.* the index lesion in a unifocal versus a multifocal tumor), or in the case of non-mass enhancement. The inter-rater agreement for tumor size at early enhancement was moderate with an ICC of 0.68 (95% CI: 0.50, 0.80; *p* < .001) for pretreatment tumor size, and 0.70 (95% CI: 0.53, 0.81; *p* < .001) for midtreatment tumor size.

Associations between BIRADS characteristics and PEPI-groups

Tumor size at initial or late enhancement on pretreatment imaging was not significantly different between the PEPI-groups (*p* = .803 and *p* = .162) nor after 3 months of NET (*p* = .953 and *p* = .517). The change in tumor size at initial enhancement, after 3

Table 1. Patient, treatment and tumor characteristics

		All tumors (*n* = 38)	PEPI-1 (*n* = 17) Good prognosis	PEPI-2/3 (*n* = 21) Poor prognosis
Age (years)				
Median (IQI)		65 (53, 70)	66.5 (54, 71)	60 (49.5, 69.5)
Laterality	*Unilateral*	32 (84.2 %)	13 (76.5 %)	19 (90.5 %)
	Bilateral	6 (15.8 %)	4 (23.5 %)	2 (9.5 %)
Tumor histology	*DCIS*	1 (2.6 %)	1 (5.9 %)	0 (0 %)
	IDC	22 (57.9 %)	11 (64.7 %)	11 (52.4 %)
	ILC	11 (28.9 %)	3 (17.6 %)	8 (38.1 %)
	Mixed IDC/ILC	4 (10.5 %)	2 (11.8 %)	2 (9.5 %)
Clinical stage	*0*	1 (2.6 %)	1 (5.9 %)	0 (0 %)
	I	10 (26.3 %)	8 (47.1 %)	2 (9.5 %)
	II	23 (60.5 %)	7 (41.2 %)	16 (76.2 %)
	III	4 (10.5 %)	1 (5.9 %)	3 (14.3 %)
Tumor grade	*1*	7 (18.9 %)	5 (31.2 %)	2 (9.5 %)
	2	24 (64.9 %)	7 (43.8 %)	17 (81 %)
	3	6 (16.2 %)	4 (25 %)	2 (9.5 %)
	Unknown	1	1	0
ER-percentage (IQI)				
Median (IQI)		100 (97.5, 100)	100 (100, 100)	100 (95, 100)
PR-percentage (IQI)				
Median (IQI)		80 (25, 92.5)	70 (45, 97.5)	80 (3, 90)
Ki67 (%)				
Pretreatment (IQI)		10 (5, 20)	11.3 (3, 20)	10 (5, 16.3)
Posttreatment (IQI)		2 (1, 5)	1 (1, 2)	5 (1, 10)
Duration of NET (months)				
Median (IQI)		7.4 (6.6, 7.9)	7.6 (6.8, 8.6)	7.0 (6, 7.7)
Therapy	*AI*	26 (68.4 %)	12 (70.6 %)	14 (66.7 %)
	Tamoxifen	8 (21.1 %)	2 (11.8 %)	6 (28.6 %)
	Combination	4 (10.5 %)	3 (17.6 %)	1 (4.8 %)
Surgery	*BCS*	31 (81.6 %)	15 (88.2 %)	16 (76.2 %)
	No BCS	7 (18.4 %)	2 (11.8 %)	5 (23.8 %)

AI, Aromatase inhibitor; BCS, Breast conserving surgery; DCIS, Ductal carcinoma in situ; ER, Estrogen receptor; IDC, Invasive ductal carcinoma; ILC, Invasive lobular carcinoma; IQI, Interquartile interval; NET, Neoadjuvant endocrine therapy; PEPI, Preoperative endocrine prognostic index; PR, Progesterone receptor.
Patient, treatment and tumor characteristics. Unless otherwise specified data are number of tumors, with percentages in parentheses.

months of treatment, decreased in both PEPI-groups. However, a larger reduction in tumor size was observed in tumors that ended up being a PEPI-1 (good prognosis) at histopathological evaluation. Tumor size decreased on average in PEPI-1 by 10 mm (IQI: 5, 13.5) compared to an average decrease of 4.5 mm (IQI: 3, 7; *p* = .045; Figure 4) in PEPI-2/3. No other BIRADS characteristics of the pretreatment MRI or the midtreatment MRI were significantly associated with PEPI (Supplementary Material 2). Background parenchymal enhancement (BPE) decreased in all patients, but was not associated with PEPI (*p* = .770). Lastly,

shrinkage pattern (*p* = .578), radiologic response (*p* = .483), and RECIST (*p* = .790) were also not associated with PEPI (Table 3). All three patients with a complete radiologic response were diagnosed with an ILC. Two of these patients with a radiologic complete response had a PEPI-2/3 (poor prognosis) at histopathological evaluation and in both patients BCS could not be performed. These patients had involved surgical margins at pathology after attempting BCS, and underwent a mastectomy afterwards. Two examples of the pre- and midtreatment MRIs are shown in Figures 5 and 6.

Table 2. Inter-rater agreement for BIRADS characteristics, DWI, shrinkage pattern, and radiologic response of pretreatment and midtreatment MRI during NET

	Inter-rater agreement	
	Pretreatment	Midtreatment
Fibroglandular tissue	0.482 (0.260, 0.705)	0.440 (0.208, 0.672)
Background parenchymal enhancement	0.681 (0.502, 0.859)	0.298 (0.030, 0.566)
Presence of mass	0.713 (0.459, 0.968)	0.684 (0.458, 0.911)
Mass – Shape	0.090 (-0.077, 0.257)	0.095 (-0.086, 0.276)
Mass – Margin	0.292 (-0.063, 0.646)	0.486 (0.085, 0.886)
Mass – Internal enhancement	0.193 (0.029, 0.358)	0.289 (0.041, 0.538)
Presence of non-mass enhancement	0.612 (0.357, 0.867)	0.469 (0.189, 0.750)
Non-mass – Distribution	−0.236 (-0.427,−0.045)	0.158 (-0.124, 0.440)
Non-mass – Internal enhancement	0.441 (-0.034, 0.916)	0
Kinetics – Early enhancement	0.482 (-0.110, 1.000)	0.519 (0.294, 0.744)
Kinetics – Late enhancement	0.482 (0.120., 0.844)	0.449 (0.204, 0.694)
Presence of diffusion restriction	0.889 (0.676, 1.000)	0.422 (0.139, 0.705)
Shrinkage pattern		0.517 (0.308, 0.725)
Radiologic response		0.670 (0.428, 0.912)

95% CI, 95% confidence interval; DWI, Diffusion weighted-imaging; NET, Neoadjuvant endocrine therapy.
Data are Cohen's κ (95% CI).

Association between DWI and PEPI-groups

Pretreatment DWI was available for 29 tumors, and midtreatment DWI for 34 tumors. There was no significant difference between the presence of diffusion restriction assessed qualitatively on pretreatment imaging (p = .622) nor at the midtreatment imaging (p = .314) between the PEPI-groups (Supplemental Materials 2).

DISCUSSION

In this study, we investigated whether pre- or midtreatment BIRADS characteristics, kinetic, and DWI findings, on MRI were associated with prognosis (on the basis of PEPI) after NET in ER+/HER2- breast cancer patients. We found that only a larger reduction of tumor size after 3 months of NET was more strongly associated with PEPI-1 (good prognosis) than with PEPI-2/3 (poor prognosis) in our patient cohort, although tumor size measurements suffered from large inter-rater variability, especially in case of multifocal masses or non-mass enhancement.

Research on the use of MRI during NET is limited. For NAC, however, several characteristics and changes on MRI associated with response or prognosis have been identified in ER+/HER2-tumors, *e.g.* a concentric shrinkage pattern was associated with improved survival.[5] In our study, shrinkage pattern was not associated with prognosis on the basis of PEPI after NET. On the other hand, changes in tumor size at initial and late enhancement were

Figure 3. Two Bland–Altman plots showing the interrater agreement of pretreatment tumor size (a) and midtreatment tumor size (b) in mm at initial enhancement on MRI.
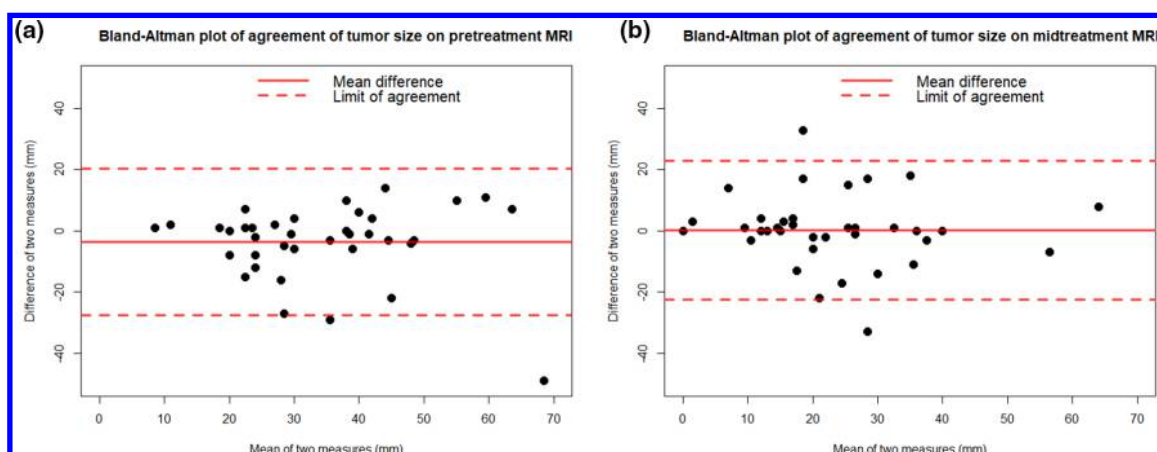
Figure 4. Change in tumor size at initial enhancement during NET. Tumor size at initial enhancement before start of NET and after three months of NET. Change in tumor size was associated with PEPI after NET (*p* = .045). However, tumor size decreased on average in both PEPI-groups: it decreased by 10 mm (IQI: 5, 13.5) in PEPI-1 (good prognosis) *vs* 4.5 mm (IQI: 3, 7) in PEPI-2/3 (poor prognosis). IQI, interquartile interval; NET, neoadjuvant endocrine therapy; PEPI, preoperative endocrine prognostic index.
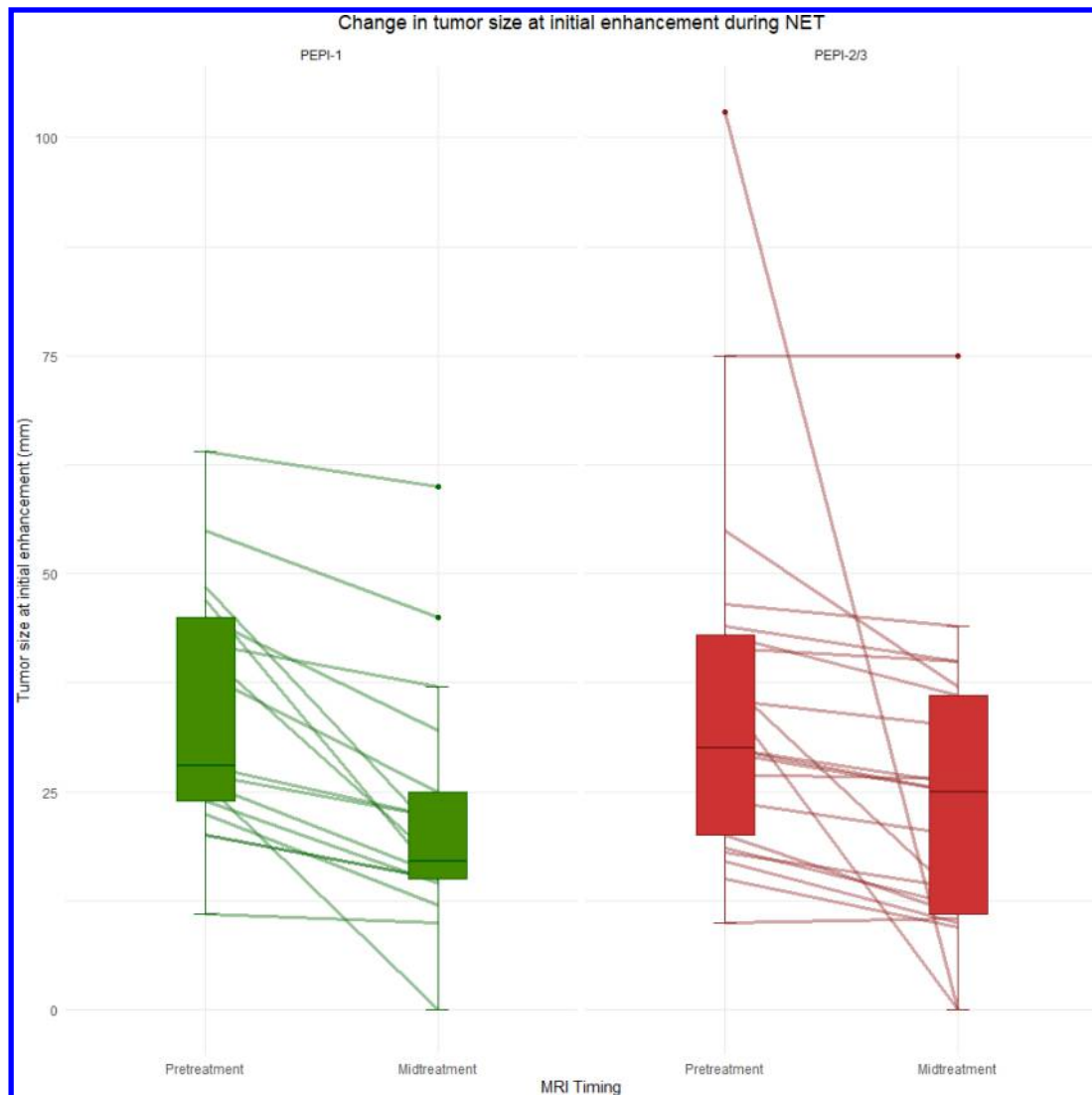
previously not associated with response in ER+/HER2- tumors during NAC,[4] but a larger reduction in tumor size was associated with PEPI-1 (good prognosis) in this study. In our study, BPE decreased in all patients, a known effect of endocrine therapy,[19] but was not associated with PEPI. However, a low pretreatment BPE was previously reported to be associated with a reduction in tumor size after NET.[8] Additionally, changes in contralateral parenchymal enhancement, a quantitative measure of the delayed enhancement of healthy breast tissue, during NET were predictive of PEPI.[20] Lastly, Reis et al, have reported a high correlation between residual disease size on MRI and pathology after NET and recommend the use of MRI for response monitoring during NET. Similar to our study, however, several patients (7 out of 35) were discordantly classified as complete responders on MRI with residual disease at pathology.[9]

As NET is increasingly recommended as an alternative for NAC in ER+/HER2- breast cancer patients,[21] it is important to identify accurate pre- or midtreatment methods to determine whether NET will be effective to allow for therapy adjustments in patients who are unlikely to experience benefit. As we report in this study, it is likely that MRI characteristics associated with a favorable prognosis after NAC are not necessarily associated with a favorable prognosis after NET. This could be due to differences in tumor biology (high proliferation *vs* low proliferation) or differences in treatment mechanisms (cytotoxic *vs* antiproliferative). Additionally, differences in findings compared to NAC studies could also be attributed to the differences in endpoints (pCR *vs* PEPI).

Although pCR is typically used as a surrogate endpoint in neoadjuvant breast cancer studies, it is poorly associated with prognosis in ER+/HER2- breast cancer.[11,12] Therefore, PEPI might be a more suitable surrogate endpoint for ER+/HER2- patients after NET, as PEPI stratifies patients in groups with distinct prognoses, and was validated in independent cohorts.[13,14]

Table 3. Shrinkage pattern and radiologic response at midtreatment MRI during NET

		PEPI-1 (*n* = 17) Good prognosis	PEPI-2/3 (*n* = 21) Poor prognosis	*p*
Shrinkage pattern	Complete response	1 (5.9%)	2 (9.5%)	.578
	Concentric	8 (47.1%)	6 (28.6%)	
	Non-concentric	6 (35.3%)	7 (33.3%)	
	No shrinkage	2 (11.8%)	6 (28.6%)	
Radiologic response	Complete response	1 (5.9%)	2 (9.5%)	.483
	Partial response	14 (82.4%)	13 (61.9%)	
	No response	2 (11.8%)	6 (28.6%)	
RECIST	Complete response	1 (5.9%)	2 (9.5%)	.790
	Partial response	7 (41.2%)	6 (28.6%)	
	Stable disease	9 (52.9%)	13 (61.9%)	
	Progressive disease	0	0	

NET, Neoadjuvant endocrine therapy; PEPI, Preoperative endocrine prognostic index; RECIST, Response evaluation criteria in solid tumors.
Shrinkage pattern and radiologic response at midtreatment MRI during NET.

A larger reduction of tumor size was associated with improved prognosis after NET (PEPI-1), however, tumor size decreased on average in both PEPI-groups during treatment. Additionally, although the tumors were measured by experienced radiologists, measurements suffered from large inter-rater variability. Although the limits of agreement included clinically meaningful thresholds (±20 mm), this was mostly due to disagreement of the index tumor (in case of multifocal masses) and in tumors with non-mass enhancement. The agreement in radiologic response was substantial between the radiologists. Remarkably, three patients showed a radiologic complete response, two of whom had a poor prognosis (PEPI-2/3) at histopathological evaluation, a similar observation made by Reis et al.[9] All three patients were diagnosed with an ILC, which are known to grow diffusely without significant desmoplastic reaction (*i.e.* show non-mass enhancement), and are often ill-defined on imaging.[22,23] Response assessment based solely on changes in tumor size should be done with care, especially in the case of ILC. Automatic quantitative analysis tools could aid the radiologists in response assessment during NET, and also decrease inter-rater variability.

Our study has some limitations. Firstly, this exploratory study was retrospective, with a relatively small and heterogeneous cohort of 35 patients (38 tumors), which limits the power to detect small effects. However, for a NET MRI study, this is a large sample. Secondly, NET is a relatively new treatment option and the patient selection is not as clear-cut compared to NAC, which leads to a heterogeneous cohort treated with NET for varying

Figure 5. The images of a 68-year-old patient with a T1N0 IDC (Grade: 2, ER: 100 %, PR: 60 %) of the left breast. On the pre-treatment images (top row), a unifocal mass enhancing lesion with rim enhancement of 20 mm is visible. In the kinetic analysis (middle row), only a minimal part of the lesion shows wash-out (red), the vast majority of the tumor shows cumulative contrast enhancement (blue). The ADC map (right row) shows diffusion restriction in the rim of the lesion. After 3 months of AI, the size of the mass decreased to 15 mm (largest diameter). Enhancement and diffusion restriction are still present but significantly reduced. This patient was considered a radiologic partial responder. At histopathological evaluation, the specimen was assigned a PEPI-1 (good prognosis). ADC, apparent diffusion coefficient; AI, aromatase inhibitor; DCE, dynamic contrast-enhanced; DWI, diffusion weighted-imaging; ER, estrogen receptor; IDC, invasive ductal carcinoma; PR, progesterone receptor; PEPI, preoperative endocrine prognostic index.
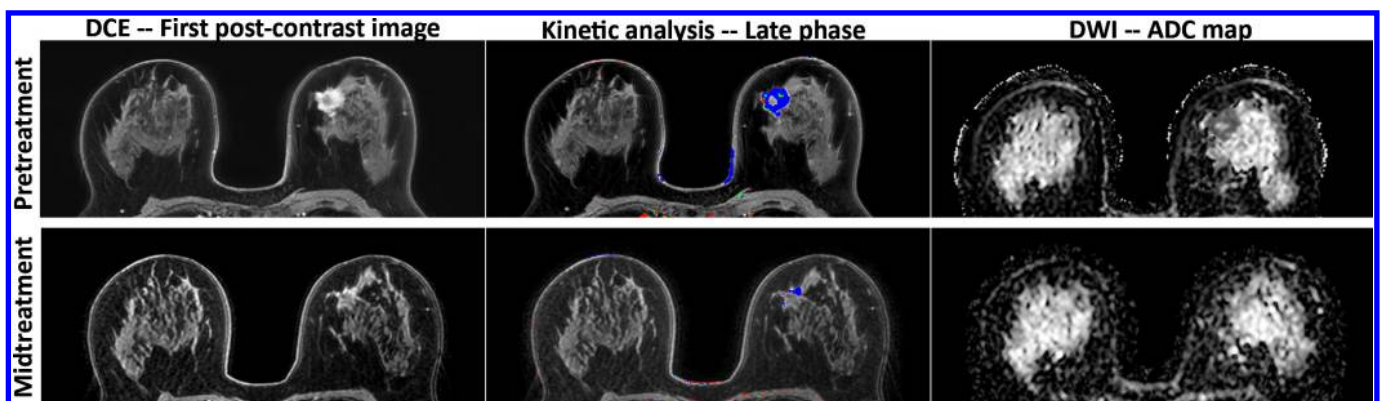
Figure 6. The images of a 71-year-old patient with a bilateral tumor. The right breast showed a T2N0 ILC (Grade: 2, ER: 100%, PR: 5%), and the left breast showed a DCIS (TisN0). The kinetic analysis showed some plateau and wash-out sections in both lesions. Diffusion restriction in the right lesion was noted. After 3 months of AI, the right lesion (ILC) showed no enhancement on the DCE and no diffusion restriction. The left lesion decreased in size, however, some sections of the lesion still showed cumulative enhancement on the kinetic analysis (shown in blue). The right lesion was considered a radiologic complete response (no patho-logical enhancement). However, at histological evaluation an invasive component of 25 mm was found in the surgical specimen. The lesion was assigned a PEPI-2/3 (poor prognosis). The left lesion was considered a partial responder after 3 months of NET, and was assigned a PEPI-1 (good prognosis) at histological evaluation (based on pathologic complete response). ADC, apparent diffusion coefficient; AI, aromatase inhibitor; DCE, dynamic contrast-enhanced, DWI, diffusion-weighted imaging; DCIS, ductal carcinoma *in situ*; ER, estrogen receptor; ILC, invasive lobular carcinoma, PR, progesterone receptor; PEPI, preoperative endocrine prognostic index.
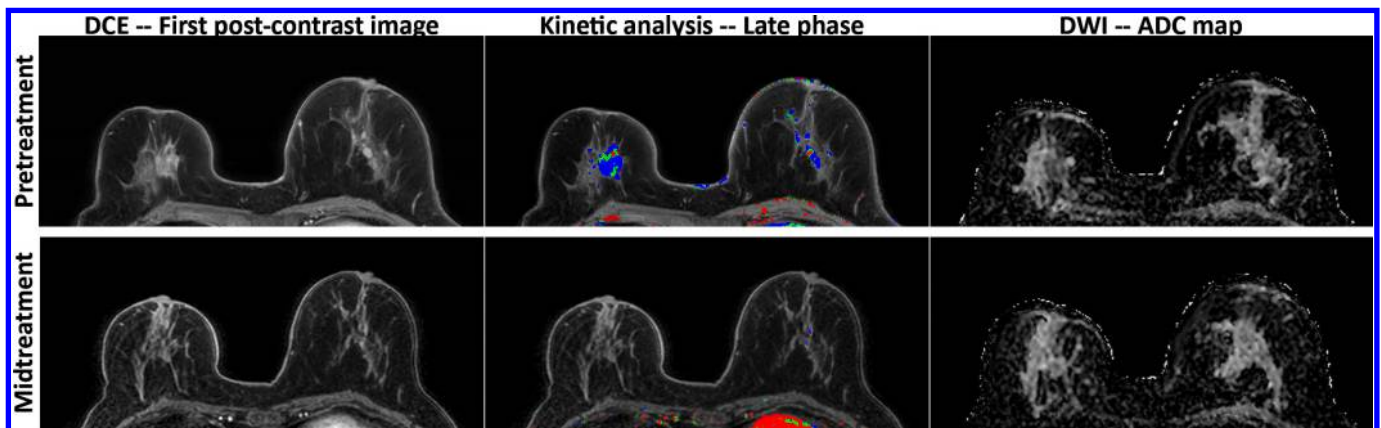
reasons (*e.g.* strong ER+ tumors *vs* excess comorbidity). Additionally, there are no guidelines for response evaluation during NET: the patient cohort might be the result of selection bias, where difficult to image tumors were evaluated with MRI as opposed to ultrasound. This could also explain the large inter-rater variability. Thirdly, differences in tumor response and change in BPE exist between AI and tamoxifen,[1,19] however, due to small sample size we could not further stratify the patient cohort into different treatment groups. Lastly, tumor ADC at DWI was reported to be associated with tumor response after NAC and survival in general,[6,24] however, due to the different *b*-value pairs used during the midtreatment imaging resulting in variability of ADC measurements,[25,26] we could not perform a quantitative ADC analysis. The results should be interpreted with this perspective in mind and should certainly be validated in a larger cohort.

In conclusion, larger reduction of tumor size after three months of NET was significantly associated with PEPI-1 (good prognosis) at histopathological evaluation. No other investigated breast MRI characteristics were associated with PEPI. Response monitoring based only on change in tumor size should, however, be done with care, because tumor size also decreased on average in patients with PEPI-2/3 (poor prognosis). Particularly, in the case of an ILC, multifocal tumor or non-mass enhancement, size measurements on MRI suffers from inter-rater variability. MRI characteristics previously reported to be associated with prognosis after NAC in literature were not associated with prognosis after NET in the current study. Radiologists must be aware that response evaluation on MRI differ between NET and NAC.

REFERENCES

1. Spring LM, Gupta A, Reynolds KL, Gadd MA, Ellisen LW, Isakoff SJ, et al. Neoadjuvant endocrine therapy for estrogen receptor-positive breast cancer: a systematic review and meta-analysis. *JAMA Oncol* 2016; **2**: 1477–86. doi: https://doi.org/10.1001/jamaoncol.2016.1897
2. Selli C, Dixon JM, Sims AH. Accurate prediction of response to endocrine therapy in breast cancer patients: current and future biomarkers. *Breast Cancer Res* 2016; **18**: 1–10. doi: https://doi.org/10.1186/s13058-016-0779-0
3. Fowler AM, Mankoff DA, Joe BN. Imaging neoadjuvant therapy response in breast cancer. *Radiology* 2017; **285**: 358–75. doi: https://doi.org/10.1148/radiol.2017170180
4. Loo CE, Straver ME, Rodenhuis S, Muller SH, Wesseling J, Vrancken Peeters M-JTFD, et al. Magnetic resonance imaging response monitoring of breast cancer during neoadjuvant chemotherapy: relevance of breast cancer subtype. *J Clin Oncol* 2011; **29**: 660–6. doi: https://doi.org/10.1200/JCO.2010.31.1258
5. Fukada I, Araki K, Kobayashi K, Shibayama T, Takahashi S, Gomi N, et al. Pattern of tumor shrinkage during neoadjuvant chemotherapy is associated with prognosis in low-grade luminal early breast cancer. *Radiology* 2018; **286**: 49–57. doi: https://doi.org/10.1148/radiol.2017161548

6. Partridge SC, Zhang Z, Newitt DC, Gibbs JE, Chenevert TL, Rosen MA, et al. Diffusion-Weighted MRI findings predict pathologic response in neoadjuvant treatment of breast cancer: the ACRIN 6698 multicenter trial. *Radiology* 2018; **289**: 618–27. doi: https://doi.org/10.1148/radiol.2018180273

7. Santamaría G, Bargalló X, Fernández PL, Farrús B, Caparrós X, Velasco M. Neoadjuvant systemic therapy in breast cancer: association of contrast-enhanced MR imaging findings, diffusion-weighted imaging findings, and tumor subtype with tumor response. *Radiology* 2017; **283**: 663–72. doi: https://doi.org/10.1148/radiol.2016160176

8. Hilal T, Covington M, Kosiorek HE, Zwart C, Ocal IT, Pockaj BA, et al. Breast MRI phenotype and background parenchymal enhancement may predict tumor response to neoadjuvant endocrine therapy. *Breast J* 2018; **24**: 1010–4. doi: https://doi.org/10.1111/tbj.13101

9. Reis J, Lindstrøm JC, Boavida J, Gjesdal K-I, Park D, Bahrami N, et al. Accuracy of breast MRI in patients receiving neoadjuvant endocrine therapy: comprehensive imaging analysis and correlation with clinical and pathological assessments. *Breast Cancer Res Treat* 2020; **184**: 407–20. doi: https://doi.org/10.1007/s10549-020-05852-7

10. Drisis S, Metens T, Ignatiadis M, Stathopoulos K, Chao S-L, Lemort M. Quantitative DCE-MRI for prediction of pathological complete response following neoadjuvant treatment for locally advanced breast cancer: the impact of breast cancer subtypes on the diagnostic accuracy. *Eur Radiol* 2016; **26**: 1474–84. doi: https://doi.org/10.1007/s00330-015-3948-0

11. Cortazar P, Zhang L, Untch M, Mehta K, Costantino JP, Wolmark N, et al. Pathological complete response and long-term clinical benefit in breast cancer: the CTNeoBC pooled analysis. *Lancet* 2014; **384**: 164–72. doi: https://doi.org/10.1016/S0140-6736(13)62422-8

12. von Minckwitz G, Untch M, Blohmer J-U, Costa SD, Eidtmann H, Fasching PA, et al. Definition and impact of pathologic complete response on prognosis after neoadjuvant chemotherapy in various intrinsic breast cancer subtypes. *J Clin Oncol* 2012; **30**: 1796–804. doi: https://doi.org/10.1200/JCO.2011.38.8595

13. Ellis MJ, Suman VJ, Hoog J, Goncalves R, Sanati S, Creighton CJ, et al. Ki67 proliferation index as a tool for chemotherapy decisions during and after neoadjuvant aromatase inhibitor treatment of breast cancer: results from the American College of surgeons Oncology Group Z1031 trial (alliance. *J Clin Oncol* 2017; **35**: 1061–9. doi: https://doi.org/10.1200/JCO.2016.69.4406

14. Ellis MJ, Tao Y, Luo J, A'Hern R, Evans DB, Bhatnagar AS, et al. Outcome prediction for estrogen receptor-positive breast cancer based on postneoadjuvant endocrine therapy tumor characteristics. *J Natl Cancer Inst* 2008; **100**: 1380–8. doi: https://doi.org/10.1093/jnci/djn309

15. D'Orsi C, Sickles EA, Mendelson EB ME, Reporting BI. *Data System: ACR BI-RADS Breast Imaging Atlas*. Reston, VA: American College of Radiology; 2013.

16. Eisenhauer EA, Therasse P, Bogaerts J, Schwartz LH, Sargent D, Ford R, et al. New response evaluation criteria in solid tumours: revised RECIST guideline (version 1.1. *Eur J Cancer* 2009; **45**: 228–47. doi: https://doi.org/10.1016/j.ejca.2008.10.026

17. Koo TK, Li MY. A guideline of selecting and reporting intraclass correlation coefficients for reliability research. *J Chiropr Med* 2016; **15**: 155–63. doi: https://doi.org/10.1016/j.jcm.2016.02.012

18. Landis JR, Koch GG. The measurement of observer agreement for categorical data. *Biometrics* 1977; **33**: 159–74. doi: https://doi.org/10.2307/2529310

19. Schrading S, Schild H, Kühr M, Kuhl C. Effects of tamoxifen and aromatase inhibitors on breast tissue enhancement in dynamic contrast-enhanced breast MR imaging: a longitudinal intraindividual cohort study. *Radiology* 2014; **271**: 45–55. doi: https://doi.org/10.1148/radiol.13131198

20. Ragusi MAA, Loo CE, van der Velden BHM, Wesseling J, Linn SC, Beets-Tan RG, et al. Contralateral parenchymal enhancement on breast MRI before and during neoadjuvant endocrine therapy in relation to the preoperative endocrine prognostic index. *Eur Radiol* 2020; **30**: 6740–8. doi: https://doi.org/10.1007/s00330-020-07058-3

21. Chiba A, Hoskin TL, Heins CN, Hunt KK, Habermann EB, Boughey JC. Trends in neoadjuvant endocrine therapy use and impact on rates of breast conservation in hormone receptor-positive breast cancer: a national cancer data base study. *Ann Surg Oncol* 2017; **24**: 418–24. doi: https://doi.org/10.1245/s10434-016-5585-5

22. Lopez JK, Bassett LW. Invasive lobular carcinoma of the breast: spectrum of mammographic, us, and MR imaging findings. *Radiographics* 2009; **29**: 165–76. doi: https://doi.org/10.1148/rg.291085100

23. Johnson K, Sarma D, Hwang ES. Lobular breast cancer series: imaging. *Breast Cancer Res* 2015; **17**: 1–8. doi: https://doi.org/10.1186/s13058-015-0605-0

24. Kim JY, Kim JJ, Hwangbo L, Kang T, Park H. Diffusion-Weighted imaging of invasive breast cancer: relationship to distant Metastasis–free survival. *Radiology* 2019; **291**: 300–7. doi: https://doi.org/10.1148/radiol.2019181706

25. Zhang JL, Sigmund EE, Chandarana H, Rusinek H, Chen Q, Vivier P-H, et al. Variability of renal apparent diffusion coefficients: limitations of the monoexponential model for diffusion quantification. *Radiology* 2010; **254**: 783–92. doi: https://doi.org/10.1148/radiol.09090891

26. Koh D-M, Collins DJ, Orton MR. Intravoxel incoherent motion in body diffusion-weighted MRI: reality and challenges. *AJR Am J Roentgenol* 2011; **196**: 1351–61. doi: https://doi.org/10.2214/AJR.10.5515

FULL PAPER

Delayed contrast dynamics as marker of regional impairment in pulmonary fibrosis using 5D MRI - a pilot study

[1,2,3,4]MARIA TA BUZAN, MD, PhD, [5,6]ANDREAS WETSCHEREK, PhD, [5]CHRISTOPHER M RANK, PhD, [3,7]MICHAEL KREUTER, MD, PhD, [1,3,7]CLAUS PETER HEUSSEL, MD, PhD, [5]MARC KACHELRIEß, PhD and [1,8,9]JULIEN DINKEL, MD, PhD

[1]Department of Diagnostic and Interventional Radiology with Nuclear Medicine, Thoraxklinik at Heidelberg University Hospital, Heidelberg, Germany
[2]Department of Pneumology, Iuliu Hatieganu University of Medicine and Pharmacy, Cluj-Napoca, Romania
[3]Translational Lung Research Center Heidelberg (TLRC), Member of the German Center for Lung Research (DZL), Heidelberg, Germany
[4]Addenbrooke's Hospital, Cambridge University Hospitals NHS Foundation Trust, Cambridge, United Kingdom
[5]Medical Physics in Radiology, German Cancer Research Center (DKFZ), Heidelberg, Germany
[6]Joint Department of Physics at The Institute of Cancer Research and The Royal Marsden NHS Foundation Trust, London, United Kingdom
[7]Center for Rare and Interstitial Lung Diseases, Pneumology and respiratory critical care medicine, Thoraxklinik, Heidelberg University Hospital, Heidelberg, Germany
[8]Institute for Clinical Radiology, Ludwig-Maximilians-University Hospital Munich, Munich, Germany
[9]Comprehensive Pneumology Center Munich (CPC-M), Member of the German Center for Lung Research (DZL), Munich, Germany

Address correspondence to: Dr Andreas Wetscherek
E-mail: *andreas.wetscherek@icr.ac.uk*

Objective: To analyse delayed contrast dynamics of fibrotic lesions in interstitial lung disease (ILD) using five dimensional (5D) MRI and to correlate contrast dynamics with disease severity.

Methods: 20 patients (mean age: 71 years; M:F, 13:7), with chronic fibrosing ILD: n = 12 idiopathic pulmonary fibrosis (IPF) and n = 8 non-IPF, underwent thin-section multislice CT as part of the standard diagnostic workup and additionally MRI of the lung. 2 min after contrast injection, a radial gradient echo sequence with golden-angle spacing was acquired during 5 min of free-breathing, followed by 5D image reconstruction. Disease was categorized as severe or non-severe according to CT morphological regional severity. For each patient, 10 lesions were analysed.

Results: IPF lesions showed later peak enhancement compared to non-IPF (severe: p = 0.01, non-severe: p = 0.003). Severe lesions showed later peak enhancement compared to non-severe lesions, in non-IPF (p = 0.04),

but not in IPF (p = 0.35). There was a tendency towards higher accumulation and washout rates in IPF compared to non-IPF in non-severe disease. Severe lesions had lower washout rate than non-severe ones in both IPF (p = 0.003) and non-IPF (p = 0.005). Continuous contrast agent accumulation, without washout, was found only in IPF lesions.

Conclusions: Contrast agent dynamics are influenced by type and severity of pulmonary fibrosis, which might enable a more thorough characterisation of disease burden. The regional impairment is of particular interest in the context of antifibrotic treatments and was characterised using a non-invasive, non-irradiating, free-breathing method.

Advances in knowledge: Delayed contrast enhancement patterns allow the assessment of regional lung impairment which could represent different disease stages or phenotypes in ILD.

INTRODUCTION

Chronic fibrotic interstitial lung diseases (ILDs) make up a group of progressive disorders that impair the space between the epithelial and endothelial basement membranes by various degrees of inflammation and fibrosis.[1] Pulmonary function testing (PFT) reveals restrictive impairment with reduced lung volumes and decreased diffusing capacity. Fibrotic ILDs typically carry a poor prognosis, with often limited therapeutic options.[2] In Europe and USA, two new drugs were cleared recently for the treatment of patients with idiopathic pulmonary fibrosis (IPF).[3,4] However, antifibrotic therapies still lack reliable metrics to assess therapeutic response and

disease progression, in particular regarding the development and severity of perivascular fibrosis.

30 years ago, McFadden et al were first to suggest a potential role of MRI in the assessment of patients with ILD.[5] Although an inherent feature of MRI is high soft tissue contrast, contrast-enhanced studies are needed for a more precise assessment. Results of time–intensity curve analysis indicate that inflammation-predominant lesions show fast time to peak, while fibrotic lesions show delayed enhancement.[6]

We hypothesise that the same principle may be applied to further characterise fibrotic lesions of different severity. Recently, a novel motion compensated image reconstruction technique was proposed, which allows for obtaining 4D (four-dimensional) MR images (three-dimensional image volumes for different respiratory phases) of high image quality for morphological assessment,[7] which can be employed to quantify regional lung volumes.[8]

Standard motion mitigation strategies, such as breath-hold acquisition or gating, have limitations in temporal resolution, signal-to-noise ratio, artefact level, or demand inappropriately long acquisition times.[7] Studies have previously reported T1 estimation errors when patients were not able to maintain breath-hold. These problems may be minimised by applying a robust sequence, with acquisition in free breathing, which provides excellent image quality and allows for regional analysis of tissue dynamics and lung ventilation.[7,8] Furthermore, it allows for measurements in any respiratory phase and at any time point within the scanning interval.

In the present study, we aim to analyse the contrast agent accumulation patterns of fibrotic lesions in chronic ILD using a 5D MRI reconstruction of radial gradient echo data acquired in free-breathing. In this context, the term 5D refers to three spatial and two temporal dimensions, extending the concept of 4D MRI to several time points after contrast injection. Moreover, a correlation between the late enhancement dynamics and disease severity will be assessed for a more accurate definition of regional lung function impairment.

METHODS AND MATERIALS

Patients

Patients with chronic fibrotic ILD were examined in a referral tertiary-care university hospital. This prospective study included 20 consecutive patients, recruited over 4 months according to their upcoming clinic appointment, with diagnosis of stable lung fibrosis, made by multidisciplinary clinicoradiologic-pathologic consensus as recommended by current guidelines,[9] who underwent MRI of the lung. The study cohort included 13 males and 7 females, with a median and interquartile range (IQR) age of 71 [61-73] years.

As part of the standard diagnostic protocol, all patients underwent PFTs and thin-section multislice CT (TSMS-CT). MRI was performed as part of a prospective study to evaluate the contribution of MRI in the assessment of chronic ILD and received

approval from the institutional review board at Thoraxklinik at Heidelberg University Hospital (clearance number S-318/2013). Informed consent was obtained from each patient before the examination.

Computed tomography imaging

All TSMS-CT examinations were performed using a 64-multislice CT system (Somatom Definition AS, Siemens Medical Systems, Erlangen, Germany). Non-contrast scans were obtained from the lung apex to the upper abdomen, during breath-holding at end inspiratory phase. The helical scan protocol applied included: 64×0.6 mm collimation, 1.5 pitch, 0.33 s/rotation, 300–330 mm field of view, 512×512 matrix, care-dose 4D with a reference of 120 kV and 70 mAs. Reconstructions of all images were performed as contiguous slices of 1.0 mm thickness by means of a standard iterative algorithm (I40) and a lung iterative algorithm (I70).

Magnetic resonance imaging

Data acquisition

MRI data were acquired on a 1.5 T clinical whole-body MRI scanner (MAGNETOM Aera, Siemens Healthcare, Erlangen, Germany). A weight-based full dose contrast injection (0.07 mmol/kg patient weight, at 5 ml s^{-1} injection rate) of gadobutrol was administered. 2 min after contrast injection, a vendor-provided volumetric radiofrequency-spoiled gradient echo sequence with radial stack-of-stars sampling (radial-GRE) and golden angle spacing[10,11] was performed: slice orientation: sagittal, field-of-view: $385 \times 385 \times 300$ mm, voxel size: $1.5 \times 1.5 \times 5.0$ mm, TR/TE = 3.77/1.69 ms, flip angle: 12°, readout bandwidth = 490 Hz/px. Spectrally selective fat suppression was performed before acquisition of each k-space plane and a partial Fourier factor of 6/8 was used along the Cartesian-encoded dimension in combination with 33% slice oversampling and an acquired slice resolution of 8.33 mm. A total of 2035 radial planes were acquired over a total acquisition time of 350 s. Patients were advised to breathe normally.

5D image reconstruction

Self-gating refers to the use of a motion surrogate, which is derived directly from the acquired MRI data and does not require external devices, such as a respiratory belt, nor separate acquisition of a dedicated navigator signal. We performed respiratory self-gating in MATLAB (MATLAB Release 2015a, The Math-Works, Inc., Natick, MA) based on the magnitude of the k-space center,[12] where the first seven radial planes were excluded to account for the MRI signal reaching a steady-state. Principal component analysis was performed to combine signals from different receiver coils and partitions into one breathing surrogate[13] and a linear correction based on the exhale peaks of the surrogate signal was performed to account for drifts, *e.g.* due to contrast agent washout. The remaining 2028 radial planes were sorted by the amplitude of the self-gating signal to determine the end-expiration phase first. Starting from end-expiration, the spokes were sorted based on the amplitude of the breathing signal into a total of 11 overlapping respiratory bins covering the complete breathing cycle and distinguishing between inspiration and expiration (Figure 1 for details).

Figure 1. (A) Representative self-gating signal for the duration of the acquisition. Respiratory states were defined such that the same amount of time is spent in each state. Each colour represents an individual respiratory bin. Note that inspiratory and expiratory states corresponding to the same amplitude of the signal are distinguished, causing a visual overlap of the bins. The deepest inhalatory state is reached primarily at the beginning of the measurement. The end-expiratory phases are most reproducible and exhibit the least amount of motion blurring. Note that the amplitude of the self-gating signal is not directly related to a spatial position. (B) First 30 s of the self-gating signal showing the assignment to respiratory bins using the same colours as in (A). Extent of each bin along the amplitude axis is indicated by a coloured rectangle. Each bin contains the same amount of data when measured over the whole duration of the acquisition.
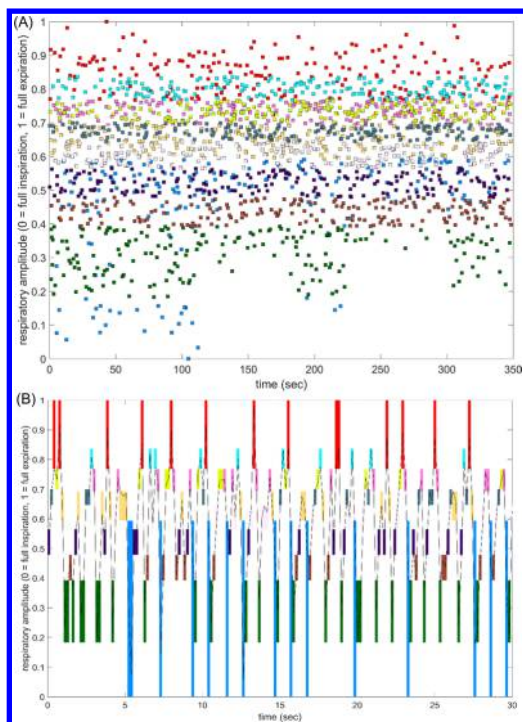
The radial MRI data were then further assigned to 5 overlapping time-steps (separated by 58.1 s each), resulting in 676 spoke planes each and an average of 122.9 radial spokes per image. After coil sensitivity profiles were jointly estimated for the whole data set,[14] 4D images (11 respiratory phases) were reconstructed separately for each time-step using an in-house developed *C*++ implementation of the recently published joint motion-compensated high-dimensional total variation algorithm.[7] In this study, only the end-expiratory phase was used for evaluation, which exhibited the lowest intraphase variation and was least affected by changes in the breathing pattern of the patients (Figure 1A) or blurring in the deepest inhalatory state due to the larger motion range (Figure 1B).

Data analysis and statistics
From the PFTs, we recorded the forced vital capacity and diffusing capacity of lung for carbon monoxide for further analysis.

The morphological severity of lung fibrosis was assessed at TSMS-CT at a regional level by a thoracic radiologist with more than 5 years of experience. Regions with dorsobasal localisation were considered as morphologically severe fibrosis, if honeycombing or reticulation with advanced lung volume loss and architectural distortion was present; and, respectively, non-severe fibrosis, if reticulation or ground glass opacities, with mild/minimal architectural distortion was observed. Architectural distortion was defined based on visual average degree of traction bronchiectasis and bronchiolectasis within the areas of fibrosis. We use the Fleischner Society nomenclature to define honeycombing, reticulation and ground glass lesions.[15] The terms *lesion* and *region* are used interchangeably throughout this manuscript to reflect the diffuse nature of fibrotic lung disease.

On the reconstructed images from the radial MRI acquisition, for each case, 10 regions of interest (in 5 consecutive slices for each lung), were selected corresponding to the lesions defined at TSMS-CT. The acquisition of MRI images in sagittal orientation allowed us to identify the corresponding regions on reference TSMS-CT sagittal reformats, as patients suffering from lung fibrosis cannot achieve deep inspiration, respectively a large displacement of the diaphragm.[16] Further, the analysis performed on contrast-enhanced images with high image quality[7] facilitated easy identification of anatomical landmarks, such as blood vessels. The availability of 5D MRI enabled identification of the corresponding regions in expiration by tracking them through the respiratory cycle.

To assess the accumulation and washout characteristics for each fibrotic region, changes in signal intensity over the course of the radial MRI acquisition were evaluated at each time step. For each region, the signal intensity was normalised on the average signal intensity at the different time points. The following quantitative parameters were evaluated: time point at which the signal intensity peaked and rates for accumulation and washout of the contrast agent. The rates represent the signal change in percent per minute and were obtained by linear least squares fitting of the data between peak value and first (accumulation), respectively last time point (washout). If the maximum signal intensity was observed at two subsequent time points, then the peak enhancement was considered in the middle of those two time points. For documentation, signal change maps were calculated by pixelwise fitting using ImageJ 1.50b software (U.S. National Institutes of Health, Bethesda, Maryland, USA).

Data analysis were performed using R statistical software version 2.15.1 (R Foundation for Statistical Computing, Vienna, Austria). Categorical data were expressed as absolute values and percentages. Fishers' exact test was applied to verify the differences of frequency for qualitative variables between the groups. Continuous variables were expressed as median and IQR. The Wilcoxon rank-sum test was used to determine differences between groups of quantitative data. All probability values were two-sided, with a significance level of 0.05.

Table 1. General difference between the IPF and non-IPF groups

Criteria	IPF Median [IQR]	Non-IPF Median [IQR]	p-value
Age (years)	72 [69-73]	62 [58-73]	0.2*
Sex (M:F)	10:2	3:5	0.06**
FVC (%)	83 [60-91]	76 [51-94]	0.7*
DLCO (%)	40 [31-47]	48 [45-51]	0.1*
TSMS-CT-MRI interval (days)	0 [0–86]	4 [0–64]	0.7*
Contrast-scan interval (s)	116 [115-126]	123 [120-126]	0.2*

DLCO, diffusing capacity of lung for carbon monoxide; FVC, forced vital capacity; IPF, idiopathic pulmonary fibrosis; IQR, interquartile range; Non-IPF, Idiopathic nonspecific interstitial pneumonia, connective tissue disease-related nonspecific interstitial pneumonia; TSMS, thin-section multislice.
* from Wilcoxon rank-sum test
** from Fisher exact test

RESULTS

The final diagnosis was IPF in 12 cases and non-IPF in 8 cases: idiopathic nonspecific interstitial pneumonia (NSIP) in 4 cases, connective tissue disease-related ILD (NSIP pattern) in another 4 cases.

Most of the patients were scheduled to undergo a CT scan during their clinic appointment with only few patients in which CT was not clinically indicated and the most recent CT was used for

Figure 2. Images (A, E and I) represent thin-section multislice CT sagittal reformats; images (B, F and J) represent the joint MoCo-HDTV reconstruction of the T1 radial-GRE acquisition at the first of the five time points; images (C, G and K) represent maps resulting from the difference between the last time step and the first time step; images (D, H and L) display the signal change over time in the drawn region of interest. Images (A–D) Non-severe fibrosis in idiopathic nonspecific interstitial pneumonia showing predominant washout during the scan interval. Images (E–H) Severe fibrosis in idiopathic pulmonary fibrosis showing continuous accumulation of contrast agent during the 5 min scan. Images (I–L) severe fibrosis in idiopathic pulmonary fibrosis showing constant signal intensity during the whole acquisition time. GRE, gradient echo sequence.
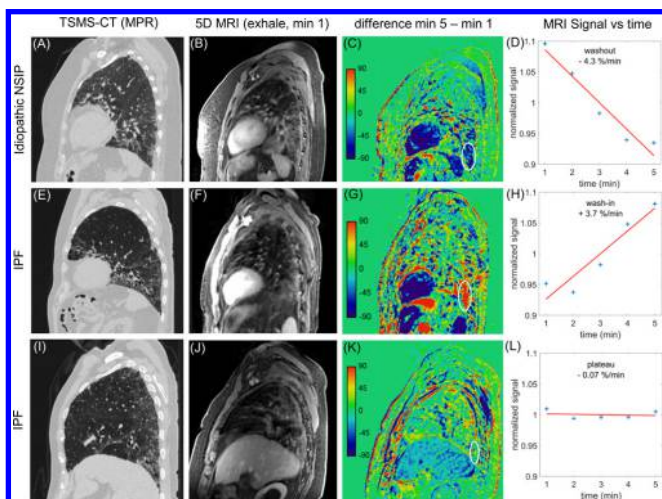
reference. The median and IQR interval between CT and MRI was 1 [0–64] days. The median and IQR interval from contrast reaching the pulmonary artery until the start of the study sequence was 121 [116-126] seconds (approximately 2 min). All reconstructed images were of good quality, allowing for further analysis.

We found no general differences between the IPF and non-IPF groups (Table 1). Regarding regional severity of the analysed fibrotic areas, in IPF, 72 regions were considered severe and 48 regions were considered non-severe disease. In non-IPF, 20 regions were considered severe and 60 regions were considered non-severe disease.

After evaluating the time-dependence of signal intensity changes, we found an overall median contrast agent accumulation rate of 1.5 [0.8–3] percent per minute and a washout rate of −1.5 [−2.5-(−0.6)] percent per minute. The first quartile was used as cut-off value for presence of accumulation and the third quartile for the presence of washout. We found 44/200 (22%) lesions, most of them in one IPF and three non-IPF cases, demonstrating plateau signal intensity, with a rate of signal intensity change between −0.6 and 0.8% per minute. From the remaining lesions, 68/200 (34%), most of them found in 3 IPF and 3 non-IPF cases, presented only washout and no accumulation during the scan interval. In 55/200 (27.5%) lesions, most of them found in 6 IPF cases, we found only accumulation and no washout during the acquisition interval. Representative examples are shown in Figure 2.

Regarding the minute of peak enhancement and the contrast agent accumulation and washout rate, we observed several differences both between IPF and non-IPF ILD groups and between severe and non-severe disease. Detailed results are presented in Tables 2 and 3.

Peak enhancement occurred later in IPF regions (around minute 6 after injection) compared to non-IPF (around minutes 3 and 4), $p < 0.05$, with no difference between severe and non-severe disease. In non-IPF, we found a later time to peak in severe compared to non-severe disease, $p = 0.04$.

Table 2. Minute of peak enhancement after contrast injection considering severity assessed on CT

Disease	IPF[a]	Non-IPF[b]	*p*-value*
Severe	6 [4–7]	4 [4–5]	**0.01**
Non-severe	6 [4–7]	3 [4–5]	**0.003**
p-value*	0.35	**0.04**	

* From Wilcoxon rank-sum test
[a]Idiopathic pulmonary fibrosis
[b]Idiopathic nonspecific interstitial pneumonia, connective tissue disease-related nonspecific interstitial pneumonia

There was a tendency towards higher accumulation and washout rates in IPF compared to non-IPF in non-severe disease. Both in IPF and non-IPF, the severe lesions had lower washout rate than non-severe ones, $p < 0.05$. Continuous contrast agent accumulation, without washout, was found only in IPF lesions.

DISCUSSION
Standard motion mitigation strategies, such as breath-hold acquisition or gating, have limitations in temporal resolution, signal-to-noise ratio, artefact level, or demand inappropriately long acquisition times.[7] Studies have previously reported T1 estimation errors when patients were not able to maintain breath-hold. We were able to minimize these problems by applying a robust sequence, with acquisition in free breathing, which provides excellent image quality and allows for regional analysis of tissue dynamics and lung ventilation.[7,8] Furthermore, it allows for measurements in any respiratory phase and at any time point within the scanning interval.

To the best of our knowledge, this is the first study to show that the type and severity of fibrosing lung disease influence the dynamics of the contrast agent, allowing for a more accurate definition of regional lung function impairment.

As previously reported at time–intensity curve analysis,[6] inflammation-predominant lesions have a higher percentage signal intensity in the initial dynamic phase at 1 min, while fibrotic predominant lesions have delayed enhancement, with peak enhancement between minute 3 and minute 9. Our results extend these findings: in IPF, regardless of the disease severity assessed on CT, we found a median peak enhancement at minute 6 after injection, while in non-IPF, this was around minutes 3 and 4, with the delay increasing with severity. Mirsadraee and

co-workers showed that the T1 value of fibrotic and apparently normal lung in IPF patients, 10 min after contrast agent administration, was significantly greater than that of normal lung tissue in the control group, and the T1 of fibrotic lung continued to decrease until 20 min after contrast agent administration.[17] We report 44 lesions with unchanged signal intensity values during the scan interval. When reviewing the CT data, some of these lesions were identified in connective tissue disease-related NSIP and had non-severe appearance at regional CT assessment. We interpreted that in these lesions the peak enhancement was before the acquisition started, and these fibrotic lesions had a fast washout, similar to that of inflammatory lesions. Other lesions presented severe disease at CT regional assessment, and we hypothesise that these advanced fibrotic lesions were only reached by minimal, if any, contrast agent, leading to unchanged signal intensity values during the acquisition interval.

Our study shows that severe non-IPF lesions display later peak enhancement compared to non-severe lesions, $p = 0.04$. The early enhancement pattern of non-severe lesions in NSIP may be due to an increase of neovascularisation through angiogenesis in these lesions. Neovascularisation is increased in early fibrosis and decreased in advanced lesions.[18] On the other hand, in usual interstitial pneumonia—the characteristic histological pattern of IPF, well-capillarised intraluminal lesions are typically not present and severe fibrosis was reported to have lower vascularity in fibroblastic foci.[19] This might explain our findings of late peak enhancement in IPF and early peak enhancement in non-IPF (NSIP pattern).

As contrast agent dynamics are influenced by the severity of fibrosis, we believe at least four patterns are of clinical importance: first, advanced fibrotic lesions tend to have the latest peak enhancement, if at all, and very slow contrast dynamics and those are hypothetically less probable to respond to any antifibrotic treatment; second, some morphological non-severe lesions may present an enhancement similar to the one of severe lesions, probably due to more perivascular fibrosis, and their response to treatment could be rather modest; third, some morphologically severe lesions show an earlier enhancement, more similar to that of non-severe lesions, and here treatment might prevent the progress of perivascular fibrosis. An additional pattern of clinical importance is the rapid wash-in and washout corresponding to active inflammatory lesions[6] and early fibrosis.

Table 3. Rate of contrast agent accumulation and washout (%/min) considering severity assessed on CT

	Accumulation rate			Wash out rate		
Disease	Non-severe	Severe	*p*-value*	Non-severe	Severe	*p*-value*
IPF[a]	2.2 [1.6–4]	2.2 [1.5–3.7]	0.92	−2.5 [−3.9-(−1.9)]	−1.6 [−1.9-(−0.9)]	**0.003**
Non-IPF[b]	1.4 [1.1–2.5]	2 [1.3–4.2]	0.42	−2.0 [−2.8-(−1.6)]	−1.5 [−1.6-(−1)]	**0.005**
p-value*	0.07	0.98		0.05	0.63	

IPF, idiopathic pulmonary fibrosis.
* From Wilcoxon rank-sum test
[a]Idiopathic pulmonary fibrosis
[b]Idiopathic nonspecific interstitial pneumonia, connective tissue disease-relatednonspecific interstitial pneumonia

Very similar findings were recently reported using hyperpolarised 129Xe MRI.[20] The authors described three distinct patterns of pathologic gas exchange which, in concordance with our results, often co-existed in the same patient and may not correlate with disease severity on CT, particularly in IPF. These patterns include: diffusion impairment with increased barrier uptake and delayed red blood cell transfer; end-stage disease with low barrier uptake and almost no red blood cell transfer; and a high barrier uptake coexisting with preserved red blood cell transfer, corresponding to early fibrotic changes. The authors speculated that novel antifibrotic therapies may achieve a positive response in latter group. However, one drawback of this method is the limited availability of hyperpolarised MRI studies, and considering the wider accessibility of dynamic contrast enhancement, our results might be of clinical and research interest. A ^{1}H MRI-based alternative is the study of late gadolinium enhancement with a stack-of-spirals technique.[21] Considering the ultrashort echo times (UTE) achievable with this approach, it could be beneficial for studying contrast-agent dynamics in pulmonary fibrosis, considering the higher signal-to-noise ratio associated with UTE imaging.

Jacob et al[22] demonstrated a correlation between the pulmonary vessel volume, lung function and extent of disease which suggests that evaluation of pulmonary vessel volume may have implications for the complex fluid dynamics in fibrotic lesions and may be an important new index when assessing disease severity in patients with IPF. Therefore, it may be of interest to analyse in further studies the relationship between delayed contrast dynamics and pulmonary vessel volume, extent of fibrosis and total and lobar pulmonary volume, respectively. The applied 5D MRI method warrants a volumetric evaluation as it would allow for global analysis of the contrast enhancement pattern and generate maps identifying the different stages and severity of fibrosis.

In Europe, antifibrotic treatment is indicated for patients with mild to moderate IPF (forced vital capacity >50% and a diffusing capacity of lung for carbon monoxide > 30–35%).[3,23] The general severity classification might be misleading in predicting treatment outcome, moreover considering that PFTs are dependent on patients' compliance and the heterogeneous disease distribution cannot be captured using global metrics. More important, since to date the results of ongoing trials including patients with other fibrotic lung disorders have not been published,[4] it is currently unknown whether antifibrotic therapies will have an effect on other fibrotic ILDs.[3] Here, our method might find further application, since we found differences in accumulation patterns between severe and non-severe disease in non-IPF patients at regional severity level. Follow-up studies have shown only minor structural alterations on CT in the first 6 months after diagnosis,[24] despite possible functional and symptomatic deterioration. Our method might be a more sensitive assessment of disease progression at regional level, since additional fibrotic accumulation would influence the contrast agent dynamics. Ultimately, this might enable a strategy for the implementation of personalised medicine to the management of chronic ILD.

Our study has four main limitations. First, our study population is small. This is because the study was designed as a proof of principle

to determine the potential applications of 5D MRI in clinical practice and research trials including patients with IPF and fibrotic NSIP. Further studies are needed to validate our results and possibly extend the findings to other categories of patients. Second, despite that vascular distribution tends to be more homogeneous in expiration,[25] because the parenchymal abnormalities in lung fibrosis involve mainly the lower lobes,[9,24] we measured the contrast dynamics only for dorsal lesions. In supine position with resting respiration, gravity determines an increase in blood volume in the posterior part of each lobe. However, at end-expiration phase, the distribution shifts more towards the ventral parts.[25] Future research will assess the influence of supine *vs* prone positioning on contrast agent accumulation patterns in lung fibrosis. Third, in our study we could not calculate the absolute value of enhancement, as our aim was to characterise the delayed contrast dynamics. With the presented non-irradiating free-breathing method, absolute values could be easily obtained, if the contrast agent is administered within the acquisition interval. At the same time, this would allow the assessment of inflammatory or very early fibrotic areas with peak enhancement in the first minute.[6] In this study, only the exhalation phase was evaluated to minimise the impact of changes in the respiratory pattern on the accuracy of the measurements. This could also be addressed by incorporating a signal model[26] into the joint-HDTV reconstruction, but is beyond the scope of this work. Last, our analysis did not take into consideration the presence of comorbidities such as pulmonary hypertension. This will be subject of further prospective research, since the most accurate diagnostic method for pulmonary hypertension—right heart catheterisation—is not regularly performed in all patients with chronic ILD. Especially in patients with advanced interstitial lung disease, there is a low specificity for determining pulmonary hypertension by measuring the pulmonary artery diameter on CT.[27]

CONCLUSIONS
The contrast agent dynamics are influenced by the type and severity of lung fibrosis. The results might enable a more thorough characterisation of progressive fibrosing lung disease, of special interest being the regional impairment, particularly in the context of new antifibrotic treatments aiming to decelerate disease progression. We demonstrated that this could be achieved using a non-invasive, non-irradiating, free-breathing method.

DISCLOSURE
CP Heussel is a consultant of Pfizer, Boehringer Ingelheim, Gilead, Intermune, and Fresenius; he also received research funding from Siemens, Pfizer, and Boehringer Ingelheim as well as fees for lectures from Gilead, MSD, Pfizer, Intermune, Boehringer Ingelheim, and Novartis.
M Kreuter received a grant from Dietmar Hopp Stiftung; he is a consultant for Intermune and he received fees for lectures and educational presentations from Boehringer Ingelheim and Intermune.

REFERENCES

1. Martinez FJ, Flaherty K. Pulmonary function testing in idiopathic interstitial pneumonias. *Proc Am Thorac Soc* 2006; **3**: 315–21. doi: https://doi.org/10.1513/pats.200602-022TK

2. Nathan SD, Shlobin OA, Weir N, Ahmad S, Kaldjob JM, Battle E, et al. Long-Term course and prognosis of idiopathic pulmonary fibrosis in the new millennium. *Chest* 2011; **140**: 221–9. doi: https://doi.org/10.1378/chest.10-2572

3. Raghu G, Selman M. Nintedanib and pirfenidone. New antifibrotic treatments indicated for idiopathic pulmonary fibrosis offer hopes and raises questions. *Am J Respir Crit Care Med* 2015; **191**: 252–4. doi: https://doi.org/10.1164/rccm.201411-2044ED

4. Richeldi L, Varone F, Bergna M, de Andrade J, Falk J, Hallowell R, et al. Pharmacological management of progressive-fibrosing interstitial lung diseases: a review of the current evidence. *Eur Respir Rev* 2018; **27**: 180074. doi: https://doi.org/10.1183/16000617.0074-2018

5. McFadden RG, Carr TJ, Wood TE. Proton magnetic resonance imaging to stage activity of interstitial lung disease. *Chest* 1987; **92**: 31–9. doi: https://doi.org/10.1378/chest.92.1.31

6. Yi CA, Lee KS, Han J, Chung MP, Chung MJ, Shin KM. 3-T MRI for differentiating inflammation- and fibrosis-predominant lesions of usual and nonspecific interstitial pneumonia: comparison study with pathologic correlation. *AJR Am J Roentgenol* 2008; **190**: 878–85. doi: https://doi.org/10.2214/AJR.07.2833

7. Rank CM, Heußer T, Buzan MTA, Wetscherek A, Freitag MT, Dinkel J, et al. 4D respiratory motion-compensated image reconstruction of free-breathing radial Mr data with very high undersampling. *Magn Reson Med* 2017; **77**: 1170–83. doi: https://doi.org/10.1002/mrm.26206

8. Kolb C, Wetscherek A, Buzan MT, Werner R, Rank CM, Kachelrie M, et al. Regional lung ventilation analysis using temporally resolved magnetic resonance imaging. *J Comput Assist Tomogr* 2016; **40**: 899–906. doi: https://doi.org/10.1097/RCT.0000000000000450

9. Raghu G, Collard HR, Egan JJ, Martinez FJ, Behr J, Brown KK, et al. An official ATS/ERS/JRS/ALAT statement: idiopathic pulmonary fibrosis: evidence-based guidelines for diagnosis and management. *Am J Respir Crit Care Med* 2011; **183**: 788–824. doi: https://doi.org/10.1164/rccm.2009-040GL

10. Block KT, Chandarana H, Milla S, Bruno M, Mulholland T, Fatterpekar G, et al. Towards routine clinical use of radial Stack-of-Stars 3D gradient-echo sequences for reducing motion sensitivity. *J Korean Soc Magn Reson Med* 2014; **18**: 87. doi: https://doi.org/10.13104/jksmrm.2014.18.2.87

11. Winkelmann S, Schaeffter T, Koehler T, Eggers H, Doessel O. An optimal radial profile order based on the golden ratio for time-resolved MRI. *IEEE Trans Med Imaging* 2007; **26**: 68–76. doi: https://doi.org/10.1109/TMI.2006.885337

12. Grimm R, Fürst S, Dregely I, Forman C, Hutter JM, Ziegler SI, et al. Self-gated radial MRI for respiratory motion compensation on hybrid PET/MR systems. *Med Image Comput Comput Assist Interv* 2013; **16**(Pt 3): 17–24. doi: https://doi.org/10.1007/978-3-642-40760-4_3

13. Paul J, Divkovic E, Wundrak S, Bernhardt P, Rottbauer W, Neumann H, et al. High-Resolution respiratory self-gated golden angle cardiac MRI: comparison of self-gating methods in combination with k-t sparse sense. *Magn Reson Med* 2015; **73**: 292–8. doi: https://doi.org/10.1002/mrm.25102

14. Bydder M, Larkman DJ, Hajnal JV. Combination of signals from array coils using image-based estimation of coil sensitivity profiles. *Magn Reson Med* 2002; **47**: 539–48. doi: https://doi.org/10.1002/mrm.10092

15. Hansell DM, Bankier AA, MacMahon H, McLoud TC, Müller NL, Remy J. Fleischner Society: glossary of terms for thoracic imaging. *Radiology* 2008; **246**: 697–722. doi: https://doi.org/10.1148/radiol.2462070712

16. Buzan MTA, Eichinger M, Kreuter M, Kauczor H-U, Herth FJ, Warth A, et al. T2 mapping of CT remodelling patterns in interstitial lung disease. *Eur Radiol* 2015; **25**: 3167–74. doi: https://doi.org/10.1007/s00330-015-3751-y

17. Mirsadraee S, Tse M, Kershaw L, Semple S, Schembri N, Chin C, et al. T1 characteristics of interstitial pulmonary fibrosis on 3T MRI-a predictor of early interstitial change? *Quant Imaging Med Surg* 2016; **6**: 42–9. doi: https://doi.org/10.3978/j.issn.2223-4292.2016.02.02

18. Cottin V, disease Ilung. Interstitial lung disease.. *Eur Respir Rev* 2013; **22**: 26–32. doi: https://doi.org/10.1183/09059180.00006812

19. Takahashi M, Kunugi S, Terasaki Y, Terasaki M, Urushiyama H, Kuwahara N, et al. The difference of neovascularization in early intra-alveolar fibrosis between nonspecific interstitial pneumonia and usual interstitial pneumonia. *Pathol Int* 2013; **63**: 237–44. doi: https://doi.org/10.1111/pin.12058

20. Wang JM, Robertson SH, Wang Z, He M, Virgincar RS, Schrank GM, et al. Using hyperpolarized [129]Xe MRI to quantify regional gas transfer in idiopathic pulmonary fibrosis. *Thorax* 2018; **73**: 21–8. doi: https://doi.org/10.1136/thoraxjnl-2017-210070

21. Pierce IT, Keegan J, Drivas P, Gatehouse PD, Firmin DN. Free-breathing 3D late gadolinium enhancement imaging of the left ventricle using a stack of spirals at 3T. *J Magn Reson Imaging* 2015; **41**: 1030–7. doi: https://doi.org/10.1002/jmri.24643

22. Jacob J, Bartholmai BJ, Rajagopalan S, Kokosi M, Nair A, Karwoski R, et al. Automated quantitative computed tomography versus visual computed tomography scoring in idiopathic pulmonary fibrosis: validation against pulmonary function. *J Thorac Imaging* 2016; **31**: 304–11. doi: https://doi.org/10.1097/RTI.0000000000000220

23. Kreuter M, Bonella F, Wijsenbeek M, Maher TM, Spagnolo P. Pharmacological treatment of idiopathic pulmonary fibrosis: current approaches, unsolved issues, and future perspectives. *Biomed Res Int* 2015; **2015**: 1–10. doi: https://doi.org/10.1155/2015/329481

24. Silva CIS, Müller NL, Pneumonias II. Idiopathic interstitial pneumonias.. *J Thorac Imaging* 2009; **24**: 260–73. doi: https://doi.org/10.1097/RTI.0b013e3181c1a9eb

25. Yoshida S, Wu D, Fukumoto M, Akagi N, Seguchi H. Quantitative study of the difference in pulmonary perfusion in different respiratory phases in healthy volunteers. *Ann Nucl Med* 2002; **16**: 533–9. doi: https://doi.org/10.1007/BF02988630

26. Feng L, Huang C, Shanbhogue K, Sodickson DK, Chandarana H, Otazo R. RACER-GRASP: Respiratory-weighted, aortic contrast enhancement-guided and coil-unstreaking golden-angle radial sparse MRI. *Magn Reson Med* 2018; **80**: 77–89. doi: https://doi.org/10.1002/mrm.27002

27. Alhamad EH, Al-Boukai AA, Al-Kassimi FA, Alfaleh HF, Alshamiri MQ, Alzeer AH, et al. Prediction of pulmonary hypertension in patients with or without interstitial lung disease: reliability of CT findings. *Radiology* 2011; **260**: 875–83. doi: https://doi.org/10.1148/radiol.11103532

FULL PAPER

Feasibility of MRI based extracellular volume fraction and partition coefficient measurements in thigh muscle

[1,2]ALEX F GOODALL, MSc, [1]DAVID A BROADBENT, PhD, [3,4]RALUCA B DUMITRU, MD, [5]DAVID L BUCKLEY, PhD, [3,4]AI LYN TAN, MRCP, MD, [3,4,6]MAYA H BUCH, PhD, FRCP and [1,3]JOHN D BIGLANDS, PhD

[1]Department Of Medical Physics and Engineering, Leeds Teaching Hospitals NHS Trust, Leeds, UK
[2]Department of Medical Imaging and Medical Physics, Sheffield Teaching Hospitals Foundation Trust, Sheffield, UK
[3]NIHR Leeds Biomedical Research Centre, Leeds, UK
[4]Leeds Institute of Rheumatic and Musculoskeletal Medicine, University Of Leeds, Leeds, UK
[5]Biomedical Imaging, University Of Leeds, Leeds, UK
[6]Centre for Musculoskeletal Research, School of Biological Sciences, Faculty of Biology, Medicine & Health, University of Manchester, Manchester, UK

Address correspondence to: Alex F Goodall
E-mail: *alexgoodall@nhs.net*

Objective: This study aimed to assess the feasibility of extracellular volume-fraction (ECV) measurement, and time to achieve contrast equilibrium (CE), in healthy muscles, and to determine whether in-flow and partial-volume errors in the femoral artery affect measurements, and if there are differences in the partition coefficient (λ) between muscles.

Methods: T1 was measured in the biceps femoris, vastus intermedius, femoral artery and aorta of 10 healthy participants. This was repeated alternately between the thigh and aorta for ≥25 min following a bolus of gadoterate meglumine. λ was calculated for each muscle/blood measurement. Time to CE was assessed semi-quantitatively.

Results: 8/10 participants achieved CE. Time to CE = 19±2 min (mean ± 95% confidence interval). Measured λ: biceps femoris/aorta = 0.210±0.034, vastus intermedius/

aorta = 0.165±0.015, biceps femoris/femoral artery = 0.265±0.054, vastus intermedius/femoral artery = 0.211±0.026. There were significant differences in λ between the muscles when using the same vessel (p < 0.05), and between λ calculated in the same muscle when using different vessels (p < 0.05).

Conclusion: ECV measurements in the thigh are clinically feasible. The use of the femoral artery for the blood measurement is associated with small but significant differences in λ. ECV measurements are sensitive to differences between muscles within the healthy thigh.

Advances in knowledge: This paper determines the time to contrast equilibrium in the healthy thigh and describes a method for measuring accurately ECV in skeletal muscle. This can aid in the diagnosis and understanding of inflammatory auto-immune diseases.

INTRODUCTION

Musculoskeletal extracellular volume-fraction (ECV) comprises the fluid-filled space between the cells within the tissue (the interstitium) and the blood plasma. It not only represents a conduit for solute exchange from the capillary to the lymphatic system but also affects cellular behaviour and fluid exchange within the tissue.[1]

T_1 weighted imaging post-contrast is useful for identifying focal pathology but of limited use for diffuse disease, and is inherently qualitative.[2] T1 measurement allows a more objective assessment, but post-contrast values on their own are sensitive to several patient and method related factors so there has been widespread interest in other areas (*e.g.*

cardiology) in the estimation of ECV from pre- and post-contrast T1 measurements.[2–6]

In cardiac magnetic resonance (MR), ECV measurement of the myocardium by T1-mapping before and after gadolinium-based contrast agent (GBCA) administration is sensitive to focal and diffuse fibrosis, oedema and myocyte hypertrophy and is used to study a range of ischaemic and non-ischaemic subclinical myocardial pathologies.[3–5] ECV mapping has been proven to be sensitive to both subtle and global changes in myocardial fibrosis that could be missed or obscured on late gadolinium-enhanced (LGE) imaging.[2,6]

Recently, it has been shown that ECV measurements in skeletal muscle could be important in assessing and understanding inflammatory and fibrotic diseases which affect skeletal muscle. Banypersad et al[7] measured ECV in the biceps, using a cardiac MR protocol, where they found a significant ($p < 0.0001$) increase in ECV in patients with amyloidosis compared to healthy volunteers across multiple organs and tissues. Similarly, Barison et al[8] measured ECV of the pectoralis and latissimus dorsi (visible on cardiac MR) and found a greater ECV for patients with scleroderma compared to healthy volunteers (23±6% vs. 18±4%, $p < 0.01$). More recently, DeMarchi et al[9] have shown that scleroderma can be detected in both cardiac and skeletal muscles using LGE, and Huber et al[10,11] demonstrated that ECV measurements in skeletal muscle (again those visible on cardiac MR) offered high sensitivity and specificity (95 and 80% respectively – receiver operator characteristic (ROC) area under curve (AUC) of 0.94) in differentiating patients with idiopathic inflammatory myopathy (IIM) and healthy controls and similar levels (sensitivity – 95%, specificity – 89%, ROC AUC – 0.96) at differentiating between IIM and acute viral myocarditis patients.

However, these studies examined skeletal muscle visible at the edge of the field of view of a cardiac image, where errors due to B1 inhomogeneity could be significant. Furthermore, accurate ECV measurement requires T1 measurements pre-contrast and after contrast-agent equilibrium (CE) is established (*i.e.* when the exchange of contrast agent between the interstitium and the blood pool is such that the concentrations of contrast agent in the two volumes are equal). Previous measurements have assumed that the time delay necessary to achieve CE in skeletal muscle and the heart is the same. However, the lower resting perfusion rate of skeletal muscle may lengthen the time necessary for equilibrium to be established, and insufficient waiting times will cause errors in ECV. Therefore, it is important to establish whether or not the waiting times of around 15–20 min, that are routinely used to ensure CE in the heart, are adequate in the muscle, and what magnitude of errors in ECV measurements are likely if this order of waiting time is used for skeletal muscle. ECV measurements are likely to be sensitive to differences in tissue microstructure between the quadriceps and hamstrings.[12] It is important to establish the magnitude of these differences in the normal thigh so that differences in future studies in diseased populations can be better interpreted.

This study applies ECV measurement in the thigh because it provides large, axial muscle volumes for T1 measurement, is not affected by cardiac or breathing motion artefacts, and the femoral vessels provide relatively large regions for blood T1 measurement. However, the blood T1 measurements may be susceptible to partial volume effects, as their size may not be much larger than the clinically achievable image resolution. Additionally, inflow effects due to through-plane blood flow could compromise accuracy. An alternative approach to blood T1 measurement is to measure T1 in the aorta, where both partial volume and in-flow effects can be minimized, but this lengthens the duration, and adds to the difficulty, of the imaging protocol.

The aims of this study were to assess whether ECV measurements in the thigh are clinically feasible, to assess the time to CE in the thigh for healthy participants, to determine whether in-flow and partial volume errors in the femoral artery affect ECV measurements and to determine whether there are differences in ECV between individual thigh muscles.

METHODS AND MATERIALS
Selection of healthy participants
10 healthy participants (6 females, mean age: 35.0 years., range: 24–43 years) were imaged before and after GBCA administration between July 2017 and April 2018. Participants were recruited under regional ethics committee approval (17/EM/0079), gave informed written consent to participate in the prospective study and were free to withdraw at any time. Exclusion criteria were: 4 weeks estimated glomerular filtration rate <45 ml min^{-1} 1.73 m^{-2}, asthma or chronic obstructive pulmonary disease, previous anaphylactic reaction to GBCAs, contraindications for MRI (claustrophobia, MR unsafe implants or foreign bodies, or pregnancy), history of rheumatic diseases, or spinal disease with neuropathy.

Imaging
Volunteers were imaged on a Siemens Verio 3 T scanner (Siemens Healthcare), feet-first supine with two Siemens small 4-channel flexible-coils (35 x 17 cm left-right by foot-head) placed with the inferior edge approximately 4 cm above the patella for the thigh images, and a Siemens body 18 matrix-coil placed on the chest for the aorta images. The contralateral leg was shielded using an RF blanket. Chest images were acquired at an oblique sagittal angle imaging from the top the aortic arch following the track of the aorta.

Images were acquired using an inversion recovery steady-state free precession sequence. A non-selective inversion pulse was used to minimise in-flow effects. An image acquired without an inversion pulse [inversion time (TI) = 0 ms] was used to obtain the initial estimate for the signal at equilibrium (S_0), in fitting the monoexponential recovery equation. Imaging parameters are given in Table 1.

Contrast [0.1 mmol kg^{-1} gadoterate meglumine (Dotarem, Guerbet LLC)] was administered intravenously as a single bolus and then alternate aorta and thigh post-contrast scans were then acquired sequentially for at least 25 min. As the signal from TI = 0 ms was only used as an initial guess for the S_0 in the fitting equation, and not used as a data point, it was excluded from the post-contrast scans to increase the temporal resolution of the data, but included pre-contrast to increase the speed and accuracy of the T1-fitting.

The pre-contrast TR for each sequence was set to 10 s so as to be greater than five times the maximum T1 for the expected biological range. The post-contrast TR was shortened to 6 s to reflect the reduction in T1 from the GBCA-administration and to decrease the time delay between acquisitions. TIs were also shortened post-contrast to reflect the increased rate of recovery. The mean time between the start of the two sequences was 73 s.

Table 1. Pre- and post-contrast acquisition parameters for the thigh and aorta sequences

Parameter	Pre-contrast values	Post-contrast values
TR (ms)	1000	6000
TE (ms)	1.83	1.83
TI (ms)	0, 80, 120, 160, 640, 3550, 5100	80, 120, 160, 320, 640, 2550
Flip angle (°)	60	60
Slice thickness (mm)	5	5
Bandwith (Hz/px)	930	930
FoV – Leg (mm x mm)	250 × 250	250 × 250
FoV – Aorta (mm x mm)	300 × 300	300 × 300
Matrix size	256 × 256	256 × 256

FOV, field of view; TE, echo time; TI, inversion time; TR, repetition time.
Contrast [0.1 mmol kg^{-1} gadoterate meglumine (Dotarem, Guerbet LLC)] was administered intravenously as a single bolus.

Data analysis
Measurement of T1 in-vivo
Image analysis was performed using MATLAB (MATLAB R2015a, The MathWorks Inc. Natick, MA, 2015) and ImageJ (ImageJ 1.51k, Rasband, W.S., ImageJ, U. S. National Institutes of Health, Bethesda, MD, https://imagej.nih.gov/ij/, 1997–2018).

Regions of interest (ROIs) were contoured within the muscles avoiding muscle fascia. For the femoral artery, a small circular ROI was created around a user-defined centre, set within the vessel, ensuring that the ROI fell fully within the vessel to minimise partial volume effects (Figure 1a). In the aorta, a rectangular ROI was created around a central line drawn by the user. The width was chosen to avoid inclusion of the vessel wall and was long enough to span the extent of at least three vertebrae. The ROI was located towards the inferior end of the aorta to minimise in-flow effects (Figure 1b). All ROIs were drawn using ImageJ. ROIs were copied across all images manually adjusting for any movement between images.

T1 values for each ROI were obtained by fitting the mean signal within the ROIs at the different TIs to a monoexponential recovery equation: -

Figure 1. (a) Example ROIs on for vastus intermedius, biceps femoris, and femoral artery on the thigh images. (b) Example ROI on for aorta on the chest images. ROI, region of interest.

$$S = S_0 \cdot \left(1 - \left(\left[1 - cos\left(\theta \right) \right] \cdot e^{\frac{-TI}{T1}} \right) \right)$$
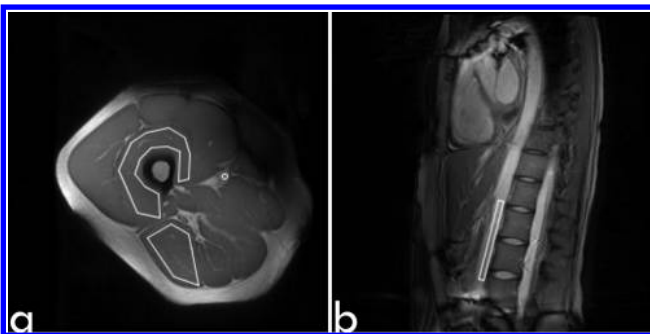
Where θ is the inversion angle, to the mean signal intensities from each ROI at each time point using a non-linear least squares fitting algorithm (lsqcurvefit, MATLAB R2015a). S_0, θ, and T1 are all free parameters in the fit. Constraints were applied so that S_0 and T1 were positive, and θ was between 0 and π radians.

The signal output of the scanner was not phase corrected from the inversion recovery, and so only the magnitude of the signal data was obtained. To fit the magnitude data to the monoexponential recovery equation the method of Messroghli et al[13] was used. The sign of the signal from each TI point, starting with the lowest TI, was changed sequentially from positive to negative, keeping previously changed values negative, and the fitting algorithm was run for each combination. The coefficient of determination (R^2) for each fit was recorded and the fit with the maximum R^2 value was chosen. Data points with values below 10% of the maximum signal in the sequence were considered to be influenced by the Rician noise floor and were therefore excluded from the fitting.

Determining the partition coefficient and time to contrast equilibrium
For each time point the partition coefficient, λ, was calculated using: -

$$\lambda = \frac{R1_{muscle}}{R1_{blood}} \left(= \frac{\left[CA_{muscle} \right]}{\left[CA_{blood} \right]} = \frac{ECV_{muscle}}{ECV_{blood}} \right)$$

Where: -

$$R1 = \frac{1}{T1}$$

To ensure that that blood and muscle values from the same time point were used, blood ΔR1 values were temporally interpolated using a biexponential decay model to reflect the more rapid decay from the GBCA entering the extravascular space and the slower decay from renal extraction.[14] This allowed a

more physiologically appropriate interpolation of the blood ΔR1 values than linear interpolation.

As GBCAs distribute themselves only within extracellular space in the interstitium and the blood–plasma within the vasculature, then at equilibrium the ratio of the GBCA concentrations will be equal to the ratio of ECV fractions (assuming sufficiently rapid water exchange) so that the effect of the contrast agent can be assumed to be averaged over the whole tissue volume. The ECV fraction in the blood is the plasma volume fraction, equal to 1-haematocrit (1 - hct), and so the ECV fraction in the muscle can be calculated (below) if the haematocrit is known, or estimated using an assumed value (*e.g.* 0.42 haematocrit as found by Jacob et al.)[15]

$$ECV = \lambda \times (1 - hct)$$

λ was then plotted against time since contrast administration and a third-order polynomial was fitted to smooth the data. Example figures of the biexponential and third-order polynomial fits are shown for one volunteer who did not reach equilibrium (Figure 2a–c) and for one who did (Figure 3a–c).

Time to CE was defined as the next acquired scan time point after the gradient of the polynomial reached zero. To investigate the magnitude of errors in ECV if the post-contrast imaging was limited to a clinically feasible time frame a pragmatic post-contrast delay time of 20 min[16] was chosen.

Statistical analysis

All statistical analysis was performed in MATLAB. Comparisons between groups were performed using a Wilcoxon signed-rank test (significance at $p < 0.05$). All results are reported as mean ± 95% confidence interval $(1.96 \times \sigma/\sqrt{n})$. No volunteers were excluded.

RESULTS

Measurement of T1 *in-vivo*

There was no significant difference between the native T1 values of blood in the aorta compared to the femoral artery (aorta 1808 ± 166 ms, femoral artery 1873 ± 298 ms; $p = 0.70$), but there was a significant difference between the T1 values of the two muscles (biceps femoris 1352 ± 21 ms, vastus intermedius 1387 ± 42 ms; $p < 0.005$) (Figure 4).

Determining the partition coefficient and time to contrast equilibrium

A CE plateau was achieved in 8/10 healthy participants. There was no significant difference between the times to CE for the two muscles ($p = 0.3$) or between measurements made using the aorta or femoral artery for the blood values ($p = 1.0$) (Table 2 and Figure 5a).

Partition coefficient (λ) measurements at equilibrium (Table 2 and Figure 5b) were significantly higher in the biceps femoris compared to the vastus intermedius, regardless of which vessel was used (aorta: $p = 0.03$, femoral artery: $p = 0.02$). λ is also higher when using the femoral artery for blood ΔR1 values,
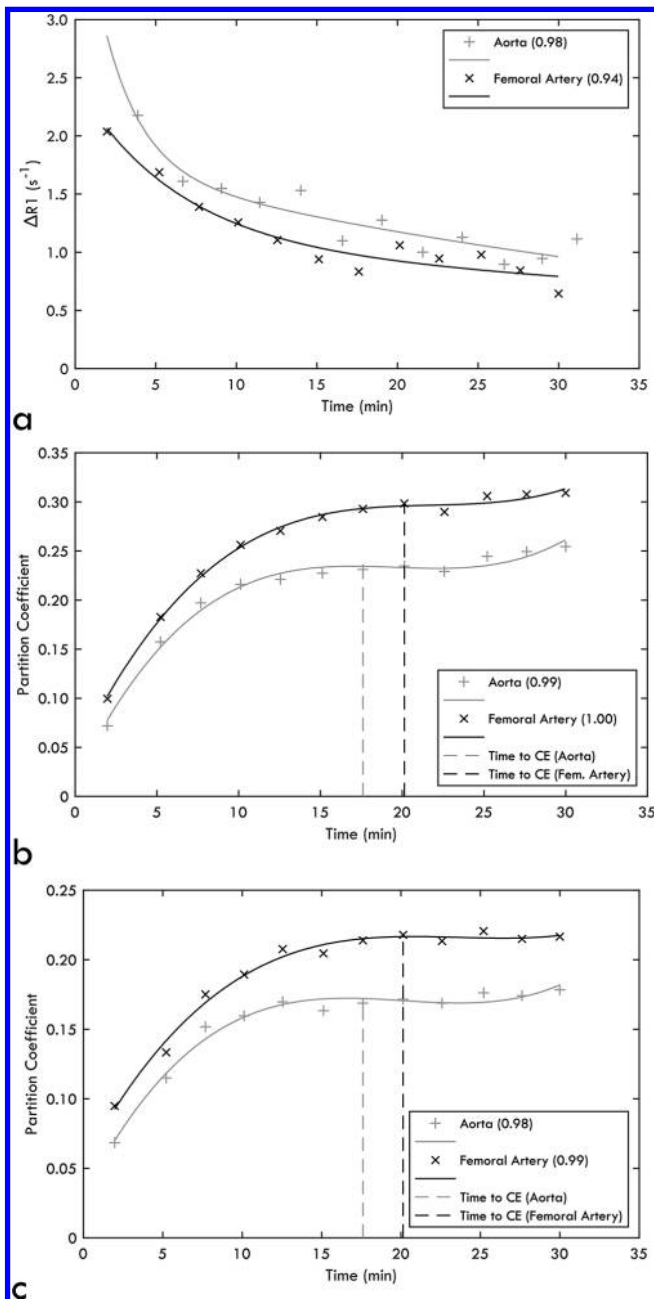
Figure 2. For a volunteer who did not reach equilibrium: (a) measured change in relaxation rate of blood measured in the aorta and femoral artery, with biexponential fits. (b) Partition coefficient in the Biceps Femoris against time graphs for aorta and femoral artery, with third-order polynomial fit. (c) Partition coefficient in the Vastus Intermedius against time graphs for aorta and femoral artery, with third-order polynomial fit. Coefficient of determination (R^2) for fit is given in brackets.
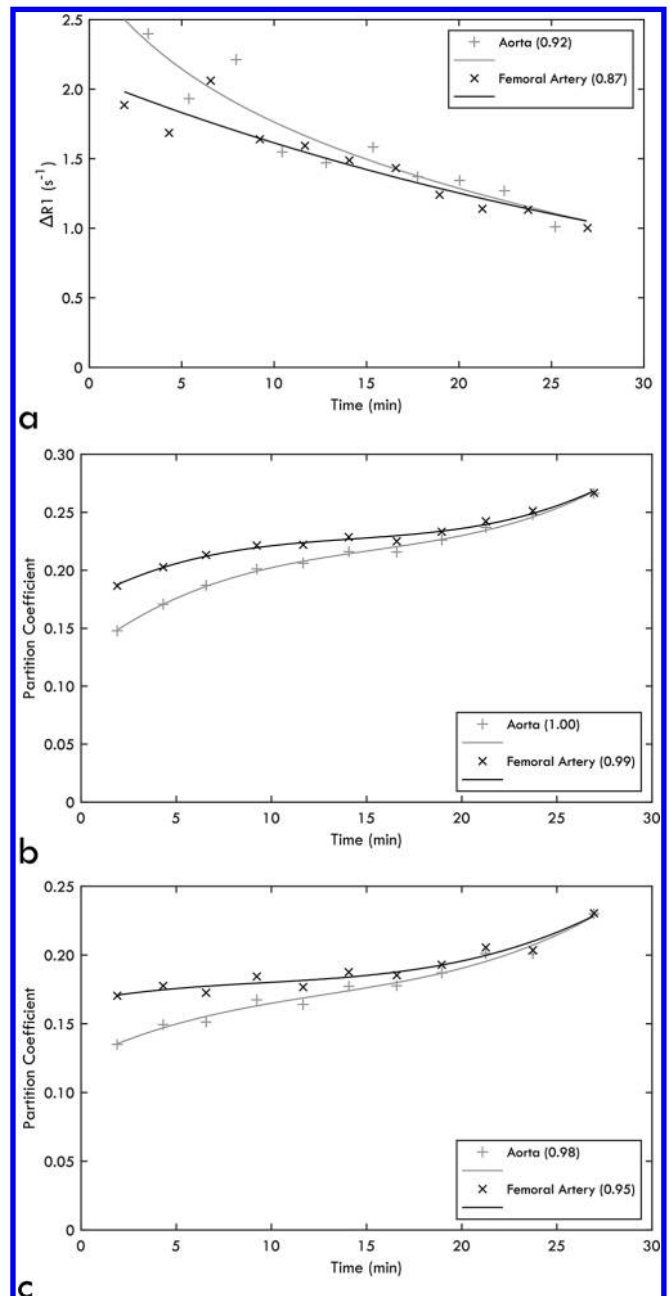
regardless of the muscle used (biceps femoris: $p = 0.01$, vastus intermedius: $p = 0.01$).

Comparisons between λ values measured using the values at 20 min (Figure 5c) and the value at equilibrium (or the end time point of the experiment for participants who didn't reach CE) are given in Table 2. Differences in λ (Δλ) between equilibrium and

Figure 3. For a volunteer who did reach equilibrium: (a) measured change in relaxation rate of blood measured in the aorta and femoral artery, with biexponential. (b) Partition coefficient in the Biceps Femoris against time graphs for aorta and femoral artery, with third order polynomial fit. (c) Partition coefficient in the Vastus Intermedius against time graphs for aorta and femoral artery, with third order polynomial fit. Coefficient of determination (R^2) for fit is given in brackets.

Figure 4. Pre-contrast T1s for the four ROIs. There is a significant difference between the T1 of the biceps femoris and the vastus intermedius (**$p < 0.01$) but not the two vessels. ROI, region of interest.

time frame of 20 min. There were small but significant changes in λ between the femoral artery and aorta-based blood ΔR1 measurements.

Measured pre-contrast T1 measurements were comparable to the literature.[17–21] The observed difference in pre-contrast T1 measurements between the biceps femoris and the vastus intermedius is consistent with known differences in muscle fibre populations and fat-fractions between quadriceps and hamstrings.[22–25] In general, T1 measurements in blood had a larger standard deviation than those in muscle, which could be due to flow effects, variability in haematocrit, or blood oxygenation levels.[26–28]

In most cases, the time to CE was achieved in <24 min. For those cases, if a pragmatic cut-off time of 20 min had been used, the resulting error in the estimated ECV would be less than 1% (assuming 0.42 haematocrit).[15,29] This suggests that skeletal-muscle ECV measurements would be achievable within a clinically relevant time scale with very small errors due to poor contrast equilibrium. However, 2/10 healthy participants did not reach CE within the time frame of the experiment. In these cases, the mean difference between λ measured at the end of the study and that measured after 20 min would lead to an underestimation of the ECV approximately equal to 1% for both biceps femoris and vastus intermedius across both blood measurements Such errors are unlikely to obscure clinical differences in ECV[7–11] (which are of the order of 5%). Therefore, we recommend a pragmatic post-contrast imaging time of 20 min. The reason for longer CE times compared to cardiac studies may be due to lower perfusion in the muscle, and so it takes longer for the relative concentrations of contrast in the blood and muscle to reach equilibrium. It may be advisable to require some exercise prior to skeletal muscle ECV measurements to ensure sufficiently high flow rates. This should be addressed in further work.

There was a significant, and systematic, difference in λ at 20 min using blood measurements taken from the aorta compared to the femoral artery, which may be due to inflow or partial volume
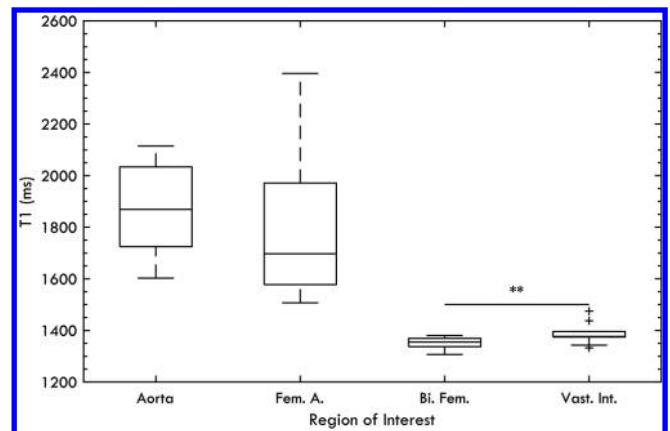
20 min (Figure 5d) were small (0.002–0.004) and not significant ($p = 0.16$–0.94) for all muscle vessel combinations.

DISCUSSION

This study has shown that ECV measurements are feasible in thigh muscle and that they are sensitive to differences between muscles. In most cases, CE was achieved in a clinically practicable

Table 2. Mean time to CE, and partition-coefficients measured at three different time points (at equilibrium, if reached, at approximately 20 min, and at the end of the scanning session) for all muscle vessel pairs

Muscle	Biceps femoris		Vastus Intermedius	
Vessel	Aorta	Femoral artery	Aorta	Femoral artery
Time to CE (min)	19.2 ± 6.1	20.4 ± 3.9	19.1 ± 4.9	18.9 ± 5.0
λ at Equilibrium	0.210 ± 0.034	0.265 ± 0.054	0.165 ± 0.015	0.211 ± 0.026
λ at 20 min	0.212 ± 0.027	0.262 ± 0.045	0.174 ± 0.016	0.213 ± 0.023
λ at End	0.225 ± 0.030	0.273 ± 0.042	0.182 ± 0.019	0.219 ± 0.021
Δλ: 20 min – Equilibrium ($n = 8$)	-0.002 ± 0.005	-0.002 ± 0.005	0.004 ± 0.005	0.003 ± 0.007
Δλ: End - 20 min ($n = 2$)	0.032	0.032	0.024	0.023

CE, contrast equilibrium.
The reported difference in partition coefficient (Δλ) is the difference between λ at 20 min and at equilibrium if reached, and at the end of the time-course if not.

effects. The mean difference in λ between both muscles using the femoral artery compared to the aorta would cause an approximate difference in the measured ECV of 2.0±1.7%. This is again too small to obscure clinical differences but may justify preferring the aorta for blood measurements.

The difference in λ for the biceps femoris and vastus intermedius could be due to different proportions of type-1 and type-2 fibres between these muscles. Vincensini et al[30] found a higher ECV in muscles with higher type-1 fibre percentage (in rabbits) and as the hamstrings have more type-1 fibres than the quadriceps[24,25] this could explain the greater λ in the biceps femoris

observed in this study. This is consistent with other studies[22–25] where differences in diffusion and fat fraction have also been noted. Estimated ECVs for the two muscle populations (aorta/femoral artery: *biceps femoris* – 9 ± 2 %/12±4%; *vastus intermedius* – 7 ± 1 % / 9±1%) are consistent with ECV measurements in skeletal muscle in the literature (10 ± 2% - Huber et al[10,11] and 9% - Banypersad et al).[7]

We acknowledge a number of limitations in this study, including small sample size. The use of magnitude images incorporates small errors in T1, and this could have been improved by using a phase-sensitive recovery sequence. Although respiratory and

Figure 5. (a) Time to contrast equilibrium for all muscle/vessel combinations. There was no significant difference in CE values between any muscle/vessel combinations. (b) Partition coefficient values for the volunteers who reached equilibrium for all muscle/vessel combinations (*$p < 0.05$, **$p < 0.01$). (c) Partition coefficient values for all volunteers at approximately 20 min (***$p < 0.005$). (d) The difference in the measured partition coefficient at 20 min for the volunteers who reached equilibrium compared to the equilibrium value. There was no significant difference between the value at 20 min and that at equilibrium.
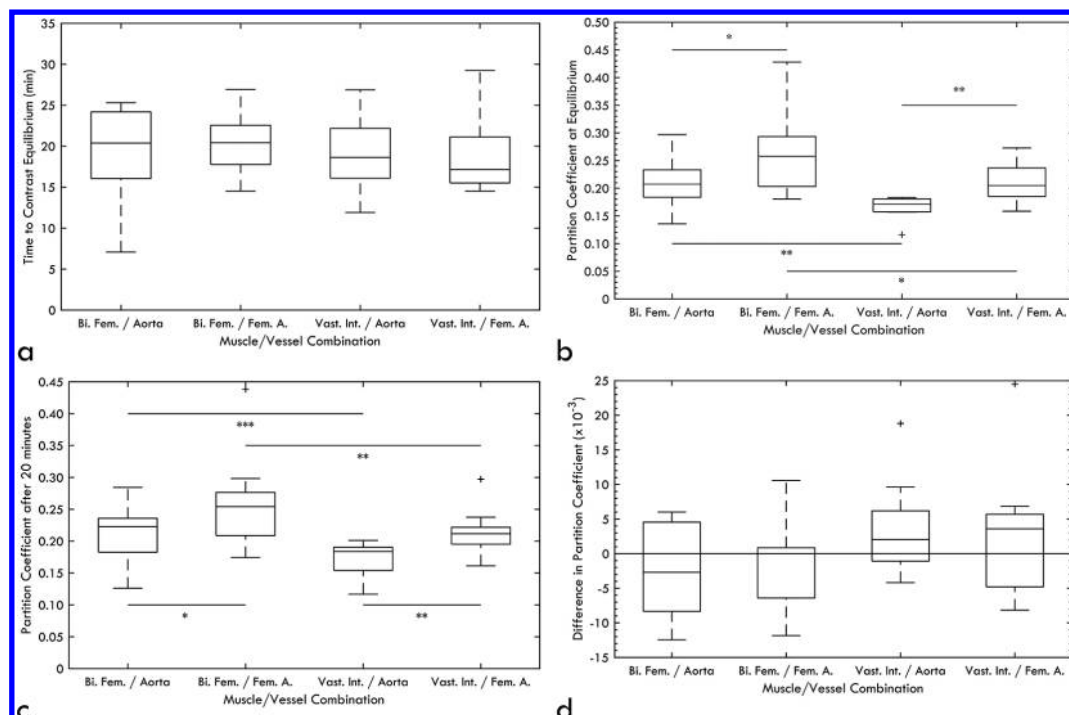
cardiac motion artefacts did not affect the region of the aorta where measurements were taken, gating techniques could have improved the quality of the data. A longer imaging time would have ensured that equilibrium was reached but could have reduced compliance and lead to discomfort and gross motion artefacts. The thigh images were not fat-suppressed which could have caused a biexponential T1 recovery due to the different T1 values of fat and water. To estimate the impact of fat on our ECV measurements fitting was repeated using a biexponential equation with an assumed fat T1 of 370 ms[16] and a fat-fraction of 5% in the vastus intermedius and 10%[31] in the biceps femoris. There was a small but significant difference in ECV at equilibrium (<1%, $p < 0.05$), and in the time to CE (3 min, $p < 0.05$). Errors of this magnitude would not be sufficient to alter the conclusions of this study.

CONCLUSION

ECV measurements in the thigh are clinically feasible and most healthy participants would reach CE using a post-contrast delay of 20 min. In cases where CE time is uncharacteristically long, using such a 20 min delay time would not induce ECV errors greater than 4%. There are small errors in partition coefficient associated with using the femoral artery for blood-pool measurements, so aortic blood-pool measurements are recommended wherever possible. There are significant differences in partition coefficient between the biceps femoris and vastus intermedius, which are consistent with known differences in muscle fibre populations.

ACKNOWLEDGEMENT

CONFLICT OF INTEREST

The authors of this manuscript declare no relationships with any companies, whose products or services may be related to the subject matter of the article.

REFERENCES

1. Scallan J, Huxley VH, Korthuis RJ. Capillary Fluid Exchange: Regulation, Functions, and Pathology. In: *Capillary Fluid Exchange: Regulation, Functions, and Pathology*. **2**. San Rafael (CA: Morgan & Claypool Life Sciences; 2010 01. 1–94. https://www.ncbi.nlm.nih.gov/books/NBK53446/.. doi: https://doi.org/10.4199/C00006ED1V01Y201002ISP003

2. Schelbert EB, Messroghli DR. State of the art: clinical applications of cardiac T1 mapping. *Radiology* 2016; **278**: 658–76. doi: https://doi.org/10.1148/radiol.2016141802

3. Kellman P, Wilson JR, Xue H, Bandettini WP, Shanbhag SM, Druey KM, et al. Extracellular volume fraction mapping in the myocardium, part 2: initial clinical experience. *J Cardiovasc Magn Reson* 2012; **14**: 64. doi: https://doi.org/10.1186/1532-429X-14-64

4. Ugander M, Oki AJ, Hsu L-Y, Kellman P, Greiser A, Aletras AH, et al. Extracellular volume imaging by magnetic resonance imaging provides insights into overt and sub-clinical myocardial pathology. *Eur Heart J* 2012; **33**: 1268–78. doi: https://doi.org/10.1093/eurheartj/ehr481

5. Haaf P, Garg P, Messroghli DR, Broadbent DA, Greenwood JP, Plein S. Cardiac T1 mapping and extracellular volume (ECV) in clinical practice: a comprehensive review. *J Cardiovasc Magn Reson* 2016; **18**: 89. doi: https://doi.org/10.1186/s12968-016-0308-4

6. Perea RJ, Ortiz-Perez JT, Sole M, Cibeira MT, de Caralt TM, Prat-Gonzalez S, et al. T1 mapping: characterisation of myocardial interstitial space. *Insights Imaging* 2015; **6**: 189–202. doi: https://doi.org/10.1007/s13244-014-0366-9

7. Banypersad SM, Bandula S, Sado D, Pinney JH, Gibbs SD, Maestrini V, et al. Multiorgan ECV as measured by EQ-MRI in systemic amyloidosis. *J Cardiovasc Magn Reson* 2013; **15**(Suppl 1): O34 doi: https://doi.org/10.1186/1532-429X-15-S1-O34

8. Barison A, Aquaro GD, Pugliese NR, Cappelli F, Chiappino S, Vergaro G, et al. Measurement of myocardial amyloid deposition in systemic amyloidosis: insights from cardiovascular magnetic resonance imaging. *J Intern Med* 2015; **277**: 605–14. doi: https://doi.org/10.1111/joim.12324

9. Barison A, Gargani L, De Marchi D, Aquaro GD, Guiducci S, Picano E, et al. Early myocardial and skeletal muscle interstitial remodelling in systemic sclerosis: insights from extracellular volume quantification using cardiovascular magnetic resonance. *Eur Heart J Cardiovasc Imaging* 2015; **16**: 74–80. doi: https://doi.org/10.1093/ehjci/jeu167

10. Huber AT, Lamy J, Bravetti M, et al. Comparison of Mr T1 and T2 mapping parameters to characterize myocardial and skeletal muscle involvement in systemic idiopathic inflammatory myopathy (IIM. *Eur Radiol* 2019;: 1–9.

11. Huber AT, Bravetti M, Lamy J, Bacoyannis T, Roux C, de Cesare A, et al. Non-Invasive differentiation of idiopathic inflammatory myopathy with cardiac involvement from acute viral myocarditis using cardiovascular magnetic resonance imaging T1 and T2 mapping. *J Cardiovasc Magn Reson* 2018; **20**: 1–11. doi: https://doi.org/10.1186/s12968-018-0430-6

12. Farrow M, Grainger AJ, Tan AL, Buch MH, Emery P, Ridgway JP, et al. Normal values and test-retest variability of stimulated-echo diffusion tensor imaging and fat fraction measurements in the muscle. *Br J Radiol* 2019; **92**: 20190143. doi: https://doi.org/10.1259/bjr.20190143

13. Messroghli DR, Radjenovic A, Kozerke S, Higgins DM, Sivananthan MU, Ridgway JP. Modified Look-Locker inversion recovery (MOLLI) for high-resolution T1 mapping of the heart. *Magn Reson Med* 2004; **52**: 141–6. doi: https://doi.org/10.1002/mrm.20110

14. Weinmann HJ, Brasch RC, Press WR, Wesbey GE, Websey GE. Characteristics of gadolinium-DTPA complex: a potential NMR contrast agent. *AJR Am J Roentgenol* 1984; **142**: 619–24. doi: https://doi.org/10.2214/ajr.142.3.619

15. Jacob M, Annaheim S, Boutellier U, Hinske C, Rehm M, Breymann C, et al. Haematocrit is invalid for estimating red cell volume: a prospective study in male volunteers. *Blood Transfus* 2012; **10**: 471–9. doi: https://doi.org/10.2450/2012.0111-11

16. Messroghli DR, Moon JC, Ferreira VM, Grosse-Wortmann L, He T, Kellman P, et al. Clinical recommendations for cardiovascular magnetic resonance mapping of T1, T2, T2* and extracellular volume: a consensus statement by the Society for cardiovascular magnetic resonance (SCMR) endorsed by the European association for cardiovascular imaging (EACVI. *J Cardiovasc Magn Reson* 2017; **19**Vol. doi: https://doi.org/10.1186/s12968-017-0389-8

17. Gold GE, Han E, Stainsby J, Wright G, Brittain J, Beaulieu C. Musculoskeletal MRI at 3.0 T: relaxation times and image contrast. *American Journal of Roentgenology* 2004; **183**: 343–51. doi: https://doi.org/10.2214/ajr.183.2.1830343

18. Sibley CT, Huang J, Ugander M, Oki A, Han J, Nacif MS, et al. Myocardial and blood T1 quantification in normal volunteers at 3T. *J Cardiovasc Magn Reson* 2011; **13**(Suppl 1): P51. doi: https://doi.org/10.1186/1532-429X-13-S1-P51

19. Stanisz GJ, Odrobina EE, Pun J, Escaravage M, Graham SJ, Bronskill MJ, et al. T1, T2 relaxation and magnetization transfer in tissue at 3T. *Magn Reson Med* 2005; **54**: 507–12. doi: https://doi.org/10.1002/mrm.20605

20. Morrow JM, Sinclair CDJ, Fischmann A, Reilly MM, Hanna MG, Yousry TA, et al. Reproducibility, and age, body-weight and gender dependency of candidate skeletal muscle MRI outcome measures in healthy volunteers. *Eur Radiol* 2014; **24**: 1610–20. doi: https://doi.org/10.1007/s00330-014-3145-6

21. Zhang X, Petersen ET, Ghariq E, De Vis JB, Webb AG, Teeuwisse WM, et al. In vivo blood T(1) measurements at 1.5 T, 3 T, and 7 T. *Magn Reson Med* 2013; **70**: 1082–6. doi: https://doi.org/10.1002/mrm.24550

22. Li K, Dortch RD, Welch EB, Bryant ND, Buck AKW, Towse TF, et al. Multi-parametric MRI characterization of healthy human thigh muscles at 3.0 T - relaxation, magnetization transfer, fat/water, and diffusion tensor imaging. *NMR Biomed* 2014; **27**: 1070–84. doi: https://doi.org/10.1002/nbm.3159

23. Scheel M, von Roth P, Winkler T, Arampatzis A, Prokscha T, Hamm B, et al. Fiber type characterization in skeletal muscle by diffusion tensor imaging. *NMR Biomed* 2013; **26**: 1220–4. doi: https://doi.org/10.1002/nbm.2938

24. Polgar J, Johnson MA, Weightman D, Appleton D. Data on fibre size in thirty-six human muscles. An autopsy study. *J Neurol Sci* 1973; **19**: 307–18. doi: https://doi.org/10.1016/0022-510x(73)90094-4

25. Edgerton VR, Smith JL, Simpson DR. Muscle fibre type populations of human leg muscles. *Histochem J* 1975; **7**: 259–66. doi: https://doi.org/10.1007/BF01003594

26. Brooks RA, Di Chiro G. Magnetic resonance imaging of stationary blood: a review. *Med Phys* 1987; **14**: 903–13. doi: https://doi.org/10.1118/1.595994

27. Lu H, Clingman C, Golay X, van Zijl PCM. Determining the longitudinal relaxation time (T1) of blood at 3.0 Tesla. *Magn Reson Med* 2004; **52**: 679–82. doi: https://doi.org/10.1002/mrm.20178

28. Wu W-C, Jain V, Li C, Giannetta M, Hurt H, Wehrli FW, et al. In vivo venous blood T1 measurement using inversion recovery true-FISP in children and adults. *Magn Reson Med* 2010; **64**: 1140–7. doi: https://doi.org/10.1002/mrm.22484

29. Sourbron SP, Buckley DL. Tracer kinetic modelling in MRI: estimating perfusion and capillary permeability. *Phys Med Biol* 2012; **57**: R1–33. doi: https://doi.org/10.1088/0031-9155/57/2/R1

30. Vincensini D, Dedieu V, Renou JP, Otal P, Joffre F. Measurements of extracellular volume fraction and capillary permeability in tissues using dynamic spin-lattice relaxometry: studies in rabbit muscles. *Magn Reson Imaging* 2003; **21**: 85–93. doi: https://doi.org/10.1016/S0730-725X(02)00638-0

31. Kumar D, Karampinos DC, MacLeod TD, Lin W, Nardo L, Li X, Majumdar S, Souza RB et al. Quadriceps intramuscular fat fraction rather than muscle size is associated with knee osteoarthritis. *Osteoarthritis Cartilage* 2014; **22**: 226–34. doi: https://doi.org/10.1016/j.joca.2013.12.005